**UF-IHEPA 01-01**

# SEARCH FOR MIXING IN THE NEUTRAL $D$ MESON SYSTEM WITH DECAYS INTO $CP$ EVEN EIGENSTATES

By

CRAIG PHILLIP PRESCOTT

A DISSERTATION PRESENTED TO THE GRADUATE SCHOOL
OF THE UNIVERSITY OF FLORIDA IN PARTIAL FULFILLMENT
OF THE REQUIREMENTS FOR THE DEGREE OF
DOCTOR OF PHILOSOPHY

UNIVERSITY OF FLORIDA

2001

For my parents, John and Janet Prescott,

and my sisters, Heidi Anne and Jennifer Joy

ACKNOWLEDGMENTS

I am indebted to many people for their help in bringing this analysis and my gradute school career to final fruition. It was a long and sometimes bumpy road to the very end, and it would not have been possible without the insight and advice from colleagues and the support of family and friends.

I owe much gratitude to my advisor, John Yelton, for his patience and guidance. John encouraged me to explore problems that attracted me and gave me the freedom to find my own way through them. This openness created a stimulating and rewarding work environment that I was lucky to be a part of. I am also indebted to Paul Avery for his willingness and enthusiasm to discuss the technical matters related to my work. Paul taught me much about the kinematic fitting crucial to this analysis, and encouraged my interests in software development and technical computing. I would also like to thank University of Florida faculty members Rick Field and Richard Woodard, who taught me undergraduate quantum mechanics and thermodynamics. It was their dedication and enthusiasm that led me to pursue a graduate degree in physics in the first place.

I was initially approached with this analysis idea by Tony Hill. As my mentor and as leader of the D Mixing Group at CLEO, Tony played a principle role in the ultimate result of this analysis as well as my development as a scientist. Harry Nelson provided inspiration and motivation, as well. I am also very grateful to Dave Cinabro, who provided valuable advice and helped shepherd this analysis to a final result, and Randal Hans, who beat this analysis into a paper after I left CLEO to start a new job.

Completion of a graduate degree in physics is more than the years of coursework, exams, and research; it also includes all the life experiences that happen over these years. I cannot overstate my gratitude to the friends I made and worked with at Cornell and Florida; not only for their enthusiastic willingness to discuss physics ideas and observations, but also for the time spent together outside the office. Indeed, these people made it possible, or at least much easier, for me to complete this analysis. At UF, the core classes, qualifying exam, and subsequent reasearch were made tolerable for me with the help of Eric Fons, Richard Haley, Mark Moores, Tony Rubiera, Vanessa Wichmann, David Willmes, and Jiu Zheng. Late night study sessions at the Clock restaurant with Fadi Zeini, games of "ball" with Sean Moore in the narrow ground floor hallway of Williamson Hall, and four a.m. trips to Perkins with Paul Moyland got me through some difficult times. At LNS, the friendship of Andy Foland, Pablo Hopman, Martin Lohner, Greg Ludwig, John O'Neill, Mark Palmer, Ed Potter, and Tony Rubiera made my two year stay in Ithaca rewarding and fun, despite all the work. I have been truly blessed to have friends like David and Deanna Asner, with whom many wonderful evenings were spent at their home on Slaterville Road. They were always there for me, especially when I was feeling low. I am also thankful to David for our many physics discussions that helped improved this analysis. Véronique Boisvert and I completed most of the tuning for the CLEO II tracking simulation, and I am very grateful for her patience and understanding during this arduous and frustrating procedure. Despite that painful experience, Véronique remained a caring friend who tried very hard to keep me from biting off more than I could chew. Silvia Schuh and I shared many wonderful times together. Silvia helped me tremendously by reminding me that there is a life to live outside of my work - a point that had become lost on me, or at least obfuscated, during the latter years of my research.

Finally, this work would not have been possible without the love and support of my parents, John and Janet Prescott, and my sisters, Heidi Anne and Jennifer Joy.

When I was frustrated, they endured my crankiness without complaint, returning only encouragement and understanding. Their confidence in me was unwavering. I cannot begin to express my gratitude for their support. This document is for them.

TABLE OF CONTENTS

ACKNOWLEDGMENTS . . . . . iii

ABSTRACT . . . . . viii

CHAPTERS

1 THEORY . . . . . 1
1.1 Particle Physics and the Standard Model . . . . . 1
1.2 Symmetry Operations $C$, $P$, and $CP$ . . . . . 5
1.3 Mixing in the $D^0 - \overline{D^0}$ System . . . . . 7
1.4 Using $CP$ Eigenstate Decays to Probe Mixing . . . . . 13
1.5 Theoretical Expectations for $y_{CP}$ and Current Experimental Limits . . . . . 17

2 EXPERIMENTAL APPARATUS . . . . . 21
2.1 The Cornell Electron Storage Ring . . . . . 21
2.1.1 Linear Accelerator . . . . . 23
2.1.2 Synchrotron . . . . . 24
2.1.3 Storage Ring . . . . . 25
2.2 The Upsilon System . . . . . 31
2.3 The CLEO Experiment . . . . . 33
2.3.1 The CLEO II Detector . . . . . 34
2.3.2 The CLEO II.V Detector . . . . . 46

3 ANALYSIS TECHNIQUE . . . . . 52
3.1 Data Samples and Event Selection . . . . . 52
3.2 Building Blocks . . . . . 53
3.3 Charged Particle Selection . . . . . 54
3.4 Neutral $D$ Meson Reconstruction . . . . . 55
3.5 Proper Time Measurement . . . . . 58
3.6 Lifetime Measurement . . . . . 62

4 RESULTS . . . . . 66
4.1 Simulation . . . . . 66
4.1.1 LifeFit Internal Generator . . . . . 66
4.1.2 FASTMC . . . . . 68
4.1.3 CLEOG . . . . . 68
4.2 Data . . . . . 80

5 CHECKS AND SYSTEMATIC UNCERTAINTIES . . . . . 88
5.1 Data Consistency Checks . . . . . 88
5.1.1 Azimuthal Angle $\phi_D$ . . . . . 89
5.1.2 Polar Angle $cos\theta_D$ . . . . . 90
5.1.3 Momentum . . . . . 91
5.1.4 Decay Angle $cos\theta^*$ . . . . . 92
5.1.5 Vertex Confidence Level prob($\chi^2_{vtx}$) . . . . . 93
5.1.6 Dataset . . . . . 94
5.2 Systematic Uncertainties . . . . . 95
5.2.1 Signal Shape . . . . . 95
5.2.2 Background Shape . . . . . 96
5.2.3 Treatment of Proper Time Outliers . . . . . 98
5.2.4 Proper Time/Mass Correlation & Mass Scale . . . . . 100
5.2.5 Length Scale . . . . . 101
5.2.6 Total Systematic Uncertainty . . . . . 102

6 CONCLUSION . . . . . 105

REFERENCES . . . . . 109

BIOGRAPHICAL SKETCH . . . . . 111

Abstract of Dissertation Presented to the Graduate School
of the University of Florida in Partial Fulfillment of the
Requirements for the Degree of Doctor of Philosophy

SEARCH FOR MIXING IN THE NEUTRAL $D$ MESON SYSTEM
WITH DECAYS INTO $CP$ EVEN EIGENSTATES

By

CRAIG PHILLIP PRESCOTT

May 2001

Chairman: John Yelton
Major Department: Physics

Using 9.0 $fb^{-1}$ of data collected with the CLEO II.V detector at the CESR $e^+e^-$ storage ring, we compare the lifetimes of neutral $D$ mesons decaying via $D^0 \to K^-K^+$ and $D^0 \to \pi^-\pi^+$ to $D^0 \to K^-\pi^+$ to measure the $D^0 - \overline{D^0}$ mixing parameter $y_{CP}$. We find $y_{CP} = -1.1 \pm 2.5 \pm 1.6\%$, where the first error is statistical and the second is systematic. This corresponds to a 95% confidence interval $-6.7 < y_{CP} < 4.5\%$.

# CHAPTER 1
# THEORY

In this document, we describe an analysis of $D^0$ meson lifetimes when the $D^0$ decays into $CP^+$ final states. In this first chapter, we discuss the physics behind this work and describe why this particular analysis is interesting.

## 1.1 Particle Physics and the Standard Model

Particle physics is in many ways the quest to find the answers to just two questions: "What are the fundamental building blocks of matter?" and "How do these building blocks interact with each other?". In the last thirty years our understanding of the universe has advanced so tremendously that we now have partial answers to these two questions. We now have a convincing picture of the fundamental structure of all observable matter in terms of a small set of building blocks, the elementary particles. The extremely successful (if incomplete) theory describing the behavior of and interactions among these building blocks is called the Standard Model.

First we describe the fundamental constituents of matter and the forces they interact through, according to the Standard Model. In the Standard Model, three generations of leptons and quarks are supposed to be the fundamental building blocks of matter. Each generation of quarks and leptons has two components. For the quark generations, shown in Table 1.1, there is a quark with electric charge $+2/3$ (among other quantum numbers) and a partner quark whose electric charge is $-1/3$. For the lepton generations, shown in Table 1.2, there is a lepton with electric charge $-1$ and a partner lepton (a neutrino) whose electric charge is 0. The quarks and leptons are fermions (particles with half odd integer spin; natural units are used throughout this document).

Table 1.1: Quark generations and some of their properties.

| Name/Flavor | Symbol | Electric Charge | Weak Isospin | Has Color | Mass (MeV) |
|---|---|---|---|---|---|
| Up | $u$ | $+2/3$ | $+1/2$ | Yes | 2–8 |
| Down | $d$ | $-1/3$ | $-1/2$ | Yes | 5–15 |
| Charm | $c$ | $+2/3$ | $+1/2$ | Yes | 1000–1600 |
| Strange | $s$ | $-1/3$ | $-1/2$ | Yes | 100–300 |
| Top | $t$ | $+2/3$ | $+1/2$ | Yes | $\approx$175000 |
| Bottom | $b$ | $-1/3$ | $-1/2$ | Yes | 4100–4500 |

Table 1.2: Lepton generations and some of their properties.

| Name | Symbol | Electric Charge | Weak Isospin | Has Color | Mass (MeV) |
|---|---|---|---|---|---|
| Electron Neutrino | $\nu_e$ | 0 | $+1/2$ | No | $< 0.000015$ |
| Electron | $e$ | $-1$ | $-1/2$ | No | 0.511 |
| Muon Neutrino | $\nu_\mu$ | 0 | $+1/2$ | No | $< 0.19$ |
| Muon | $\mu$ | $-1$ | $-1/2$ | No | 105.7 |
| Tau Neutrino | $\nu_\tau$ | 0 | $+1/2$ | No | $< 18.2$ |
| Tau | $\tau$ | $-1$ | $-1/2$ | No | 1777.0 |

The quarks and leptons make up all matter; each quark and lepton has a corresponding antimatter partner that has opposite quantum numbers, but the same mass as the matter particle. Ordinary matter (atoms and molecules) is composed of only a subset of elementary quarks and leptons. Two quarks (up and down) compose protons and neutrons, and one lepton (the electron) makes up the matter that humans encounter in everyday life. Except for their masses, each quark or lepton generation is a duplicate of another.

The forces between the elementary particles are mediated by the gauge bosons, shown in Table 1.3, and all have spin 1. The Standard Model describes three kinds of forces. The electromagnetic force, which is familiar to us all, is mediated by the photon. The electromagnetic force is responsible for binding nuclei and electrons into atoms, for example. Only particles with electric charge can interact electromagnetically. The strong force, mediated by the gluon, couples particles that have color, and

Table 1.3: Gauge Bosons and some of their properties.

| Name | Symbol | Force Mediated | Electric Charge | Mass (GeV) |
|---|---|---|---|---|
| Photon | $\gamma$ | Electromagnetism | 0 | 0 |
| Gluon | $g$ | Strong | 0 | 0 |
| $Z^0$ | $Z^0$ | Weak | 0 | 91.187 |
| $W^{+-}$ | $W^{+-}$ | Weak | $\pm 1$ | 80.40 |

is responsible for holding quarks together inside hadrons. Color is a kind of "strong charge," very much analogous to electric charge. Each quark flavor comes in three different colors, and a total of 8 gluons are required to describe the strong forces between quarks. Leptons have no color, and therefore do not interact via the strong force. This is one of the primary differences between quarks and leptons. The weak force is mediated by the $W^+$, $W^-$, and $Z^0$. Particles with "weak charge," or "weak isospin," can interact via the weak force. An example of a weak interaction is the $\beta$-decay of heavy nucleii.

Note that in Table 1.3 there is no force carrier for the most familiar force, gravity. This is because gravity is not included in the Standard Model, and is indeed one of the reasons the Standard Model is incomplete. Since the masses of the particles are so small, this turns out to be not important in particle physics.

Quantum chromodynamics (QCD) is the part of the Standard Model that describes the strong force; i.e. the interactions between quarks and gluons. It explains why free quarks have never been observed, by requiring that quarks be confined in "color singlets," that is, objects that have no net color. The possible colors for quarks are $r$ (red), $b$ (blue), and $g$ (green). Anti-quarks have "opposite" colors: $\overline{r}$ (anti-red), $\overline{b}$ (anti-blue), and $\overline{g}$ (anti-green). Colorless objects that can be constructed include mesons, $q\overline{q}$ states where the quark and anti-qaurk colors cancel each other (for example, a red quark and an anti-red anti-quark), and baryons, which are three quark states where each quark is a different color (red + green + blue = white = "colorless"). Together, mesons and baryons (and anti-baryons) make up a class of particles

called hadrons. Quarks and anti-quarks are confined into hadrons in QCD with a steep inter-quark potential that becomes extremely strong at large distance. Using a meson as an example, if we put energy into the system to try to separate the quark and anti-quark, at some point it becomes energetically favorable to produce a new quark pair. Two color singlet mesons result, and we never actually see any free quarks. On the other end of the distance scale when our quark and anti-quark are close in our meson, the inter-quark potential is smaller and the quarks are comparatively free to bounce around.

The Standard Model is very successful in explaining all existing experimental data, despite the lack of treatment for gravity. However, several additional issues remain unclear. For instance, the Standard Model mechanism by which particles acquire mass involves the existence of a yet unobserved boson, the "Higgs" particle. The Standard Model says nothing about what its mass may be. However, experimental evidence suggests it must be below 200-300 $GeV$. Why is that? Further, the Standard Model also provides a mechanism, $CP$ violation, that could explain the excess of matter over anti-matter in our universe. [1] However, is there "enough" $CP$ violation allowed in the standard model to allow creatures like ourselves to exist, or are there some still unknown processes required for that to happen? There are many other questions about which the Standard Model is silent. All told, there are some twenty free parameters in the Standard Model (depending how you count), which could imply that the Standard Model is a low-energy approximation of a greater theory that can answer questions the Standard Model cannot. Therefore, experimenters make measurements that can be checked for consistency with Standard Model pre-

[1] Were this not true, none of us would be here.

dictions. An observed inconsistency would be a signature for "New Physics" beyond the Standard Model, which could result in answers to some of these questions.

## 1.2 Symmetry Operations $C$, $P$, and $CP$

Symmetry operations upon a system transformation the system in a way which leaves it indistinguishable from the original configuration. Such symmetries manifest themselves in the laws of physics.

Charge conjugation is one such symmetry operation. The charge conjugation operator, $C$, is a unitary operator ($C^{-1} = C^{\dagger}$) changes a particle $a$ into its anti-particle $\overline{a}$ and vice-versa. Therefore, we can write

$$C|a\rangle = \eta_C|\overline{a}\rangle \tag{1.1}$$

where $\eta_C$ is a phase factor $e^{i\theta_C}$. Certainly, we can let $C$ operate on $|a\rangle$ twice to recover our original state $|a\rangle$

$$C^2|a\rangle = \eta_C(a)C|\overline{a}\rangle = \eta_C(a)\eta_C(\overline{a})|a\rangle = |a\rangle \tag{1.2}$$

which shows that $\eta_C(a)\eta_C(\overline{a}) = 1$, and it follows that $\eta_C(\overline{a}) = \eta_C(a)^*$. If (and only if) $a$ is its own anti-particle, then it is an eigenstate of $C$ [2] and $\eta_C(a) = \eta_C(\overline{a}) = \pm 1$. Examples of such eigenstates are mesons composed of a quark and anti-quark of the same flavor ($q\overline{q}$), such as the $\pi^0$, $\phi$, and $\rho^0$. The eigenvalues of $C$ for $q\overline{q}$ mesons are $\eta_C = (-1)^{L+S}$, where $L$ is the meson's orbital angular momentum quantum number and $S$ is its spin. An eigenstate with an eigenvalue of $+1$ is said to be even under charge conjugation; if the eigenvalue is $-1$, it is said to be odd. Eigenvalues of the

[2] If an equation can be written as $\mathrm{A}|a\rangle = \lambda|a\rangle$, the state $|a\rangle$ is said to be an eigenstate of the operator A, and $\lambda$ is its eigenvalue.

Table 1.4: Eigenvalues of $C$ and $P$ for some $q\bar{q}$ mesons.

| Meson | $C$ | $P$ |
|---|---|---|
| $\pi^0$ | $+1$ | $-1$ |
| $\eta$ | $+1$ | $-1$ |
| $\rho^0$ | $-1$ | $-1$ |
| $\omega$ | $-1$ | $-1$ |
| $\phi$ | $-1$ | $-1$ |

charge conjugation operator for some of the mesons used in this analysis are listed in Table 1.4.

Another example of a symmetry operation is parity. The parity operator, $P$, is a unitary operator that reverses the sign of an object's spatial coordinates, such that $P\psi(t,\vec{r}) = \psi(t,-\vec{r})$. For a particle with four momentum $p = (E,\vec{p})$ and helicity $\lambda$, the parity transformation can be written

$$P|a(p,\lambda)\rangle = \eta_P|a(\tilde{p},-\lambda)\rangle = \eta_P|a_P\rangle \tag{1.3}$$

where $\tilde{p} = (E,-\vec{p})$ and $|a_P\rangle$ is the parity-transformed version of $|a\rangle$. Parity reverses the momentum direction of $|a\rangle$, but not its spin; therefore, the helicity $\lambda = s\cdot\hat{p}$ changes sign under parity. Similar treatment as for $C$ shows that eigenvalues of $P$ must also be $\pm 1$. Mesons are eigenstates of parity, with eigenvalues $\eta_P = (-1)^{L+1}$, where $L$ is again the meson's orbital angular momentum quantum number. We say an eigenstate has even parity if its eigenvalue is $+1$ and odd parity if its eigenvalue is $-1$. Eigenvalues of the parity operator for some of the mesons used in this analysis are listed in Table 1.4.

The $CP$ operation is then the application of the parity and charge conjugation operations to a system; that is, a particle turns into its anti-particle while at the same time the system is reflected and inverted. Eigenstates of $C$ and $P$, like $q\bar{q}$ mesons, are also eigenstates of $CP$, with eigenvalues $\eta_{CP} = \eta_C\eta_P$ for single particle systems; for systems of particles, we pick up an additional multiplicative factor of $(-1)^l$, where $l$

is the orbital angular momentum of the system. For future reference, the neutral $D$ mesons of interest in this document transform thus under $C$, $P$, and $CP$

$$\begin{array}{rclrcl} C|D^0> &=& |\overline{D^0}> & C|\overline{D^0}> &=& |D^0> \\ P|D^0> &=& -|D^0> & P|\overline{D^0}> &=& -|\overline{D^0}> \\ CP|D^0> &=& -|\overline{D^0}> & CP|\overline{D^0}> &=& -|D^0> \end{array} \tag{1.4}$$

Although the strong and electromagnetic interactions are invariant under the $C$ and $P$ operations, it came as quite a surprise to physicists to find that the weak interactions were not. Order was restored when it was postulated that although the weak interactions violated the $C$ and $P$ symmetries separately, the combined symmetry $CP$ would be respected.

### 1.3 Mixing in the $D^0 - \overline{D^0}$ System

Mixing is the spontaneous oscillation of a particle into its anti-particle. This behavior can happen in ground state electrically neutral mesons with net flavor, such as in the $K^0 - \overline{K^0}$ system where it was first observed [1], for example through "box" diagrams like the one shown in Fig. 1.1. Other systems in which mixing can occur include the $D^0 - \overline{D^0}$, $B_d^0 - \overline{B_d^0}$, and $B_s^0 - \overline{B_s^0}$ systems. There are many references describing the mixing phenomenon, particularly in the $K^0 - \overline{K^0}$ and $B_d^0 - \overline{B_d^0}$ systems; some good examples exist [2, 3, 4, 5, 6]. In this section, we summarize this work and see what it can tell us about mixing in the $D^0 - \overline{D^0}$ system.

A similar notation can be used to describe all the systems in which mixing can occur. We therefore denote the eigenstates of flavor as $P^0$(=$K^0$, $D^0$, $B_d^0$, $B_s^0$) and $\overline{P^0}$. We can consider a wave function made of an arbitray linear combination of $P^0$ and $\overline{P^0}$ at time $t = 0$, and express that wave function at time $t = t$ as a linear combination

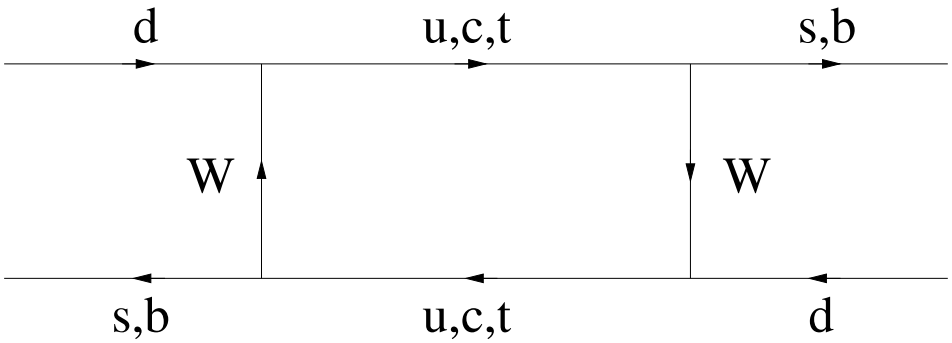


Figure 1.1: Box Diagram for $K^0 - \overline{K^0}$ and $B_d^0 - \overline{B_d^0}$ mixing.

of the flavor eigenstates and their decay products $|f\rangle$

$$|\psi(t)\rangle = a(t)|P^0\rangle + b(t)|\overline{P^0}\rangle + \sum_f c_f|f\rangle \tag{1.5}$$

where the $|f\rangle$ are the states into which $P^0$ and $\overline{P^0}$ can decay. As the system evolves in time, $P^0$ and $\overline{P^0}$ decay, so that probability migrates into the decay products $|f\rangle$.

We write the full Hamiltonian $H$ as the sum of two pieces

$$H = H_0 + H_w \tag{1.6}$$

The $H_0$ contains the strong and electromagnetic interactions and has $|P^0\rangle$ and $|\overline{P^0}\rangle$ as eigenstates. The $H_w$ contains the weak interactions responsible for the decay of $|P^0\rangle$ and $|\overline{P^0}\rangle$ states and their transformations among each other. The $H_w$ is a small perturbation on $H_0$.

Projecting into a space spanned by $|P^0\rangle$ and $|\overline{P^0}\rangle$, the evolution of $|\psi(t)\rangle$ is described by the time-dependent Schrödinger equation

$$i\frac{\partial}{\partial t}\begin{pmatrix} a(t) \\ b(t) \end{pmatrix} = \mathbf{H_{eff}}\begin{pmatrix} a(t) \\ b(t) \end{pmatrix} = \begin{pmatrix} H_{11} & H_{12} \\ H_{21} & H_{22} \end{pmatrix}\begin{pmatrix} a(t) \\ b(t) \end{pmatrix} \tag{1.7}$$

Assuming $CPT$ invariance gives

$$\equiv \left(\mathbf{M} - \tfrac{i}{2}\Gamma\right) \begin{pmatrix} a(t) \\ b(t) \end{pmatrix} \tag{1.8}$$

$$= \begin{pmatrix} M_0 - \frac{i}{2}\Gamma_0 & M_{12} - \frac{i}{2}\Gamma_{12} \\ M_{12}^* - \frac{i}{2}\Gamma_{12}^* & M_0 - \frac{i}{2}\Gamma_0 \end{pmatrix} \begin{pmatrix} a(t) \\ b(t) \end{pmatrix} \tag{1.9}$$

where $\mathbf{H_{eff}}$ is the projection of the full Hamiltonian $H$ into the subspace spanned by $|P^0\rangle$ and $|\overline{P^0}\rangle$. We have denoted the diagonal elements of $\mathbf{M}$ and $\Gamma$ as

$$M_{11} = M_{22} \equiv M_0 \quad , \quad \Gamma_{11} = \Gamma_{22} \equiv \Gamma_0 \tag{1.10}$$

which stems from the $CPT$ invariance. Note that the effective Hamiltonian is not hermitian, as probability can leak out of the space to the decay products $|f\rangle$.

The $\mathbf{M}$ is called the mass matrix, and $\Gamma$ is called the decay matrix. One can show by performing the perturbation theory analysis to second order [6] that the elements of $\mathbf{M}$ and $\Gamma$ are as follows:

$$\begin{aligned} M_{ij} &= m_P \delta_{ij} + \langle i|H_w|j\rangle + \mathcal{P}\sum_f \frac{\langle i|H_w|f\rangle\langle f|H_w|j\rangle}{m_P - E_f} \\ \Gamma_{ij} &= 2\pi \sum_f \langle i|H_w|f\rangle\langle f|H_w|j\rangle \delta(m_P - E_f) \end{aligned} \tag{1.11}$$

where $\mathcal{P}$ denotes the principal value prescription is applied when summing over the states $f$, avoiding states where $E_f = m_P$. In addition, we used

$$\begin{aligned} H_0|P^0\rangle &= m_P|P^0\rangle \\ H_0|\overline{P^0}\rangle &= m_P|\overline{P^0}\rangle \\ H_0|f\rangle &= E_f|f\rangle \end{aligned} \tag{1.12}$$

The values of the matrix elements in Equation 1.11 provide insight into the physical processes described in mixing. The diagonal terms of $\mathbf{M}$ are dominated by the eigenvalue $m_P$ of $H_0$, which makes sense as the strong interactions are responsible for binding the constituent quarks into mesons. The off-diagonal elements of $\mathbf{M}$ describe transitions between the $|P^0\rangle$ and $|\overline{P^0}\rangle$ (mixing!) through intermediate states $|f\rangle$. These states must be virtual (off-shell), as the principal value prescription excludes the on-shell component where $m_P = E_f$. The term $\langle i|H_w|j\rangle$ corresponds to a $\Delta S = 2$ interaction. Turning to the decay matrix $\Gamma$, we can see that diagonal elements arise from the allowed decays of $P^0 \to f$ and $\overline{P^0} \to \overline{f}$, with the states $f$ being on-shell due to the $\delta(m_P - E_f)$. Finally, the off-diagonal elements of $\Gamma$ describe transitions between $|P^0\rangle$ and $|\overline{P^0}\rangle$ (mixing!) through real, on-shell intermediate states $f$. However, $f$ must be a state into which both mesons can decay, thus describing processes $P^0 \to f \to \overline{P^0}$ and $\overline{P^0} \to f \to P^0$.

We can solve for the eigenstates of $\mathbf{H_{eff}}$. We can rewrite $\mathbf{H_{eff}}$ as a diagonal piece and an off-diagonal piece (commonly referred to as the mixing matrix, for reasons that soon become clear)

$$\mathbf{H_{eff}} = \begin{pmatrix} H_{11} & 0 \\ 0 & H_{11} \end{pmatrix} + \begin{pmatrix} 0 & H_{12} \\ H_{21} & 0 \end{pmatrix} \tag{1.13}$$

$$= \begin{pmatrix} M_0 - \frac{i}{2}\Gamma_0 & 0 \\ 0 & M_0 - \frac{i}{2}\Gamma_0 \end{pmatrix} + \begin{pmatrix} 0 & M_{12} - \frac{i}{2}\Gamma_{12} \\ M_{12}^* - \frac{i}{2}\Gamma_{12}^* & 0 \end{pmatrix} \tag{1.14}$$

We note that eigenstates of the off-diagonal piece are also eigenstates of $\mathbf{H_{eff}}$. These eigenstates are the mass (also known as physical) eignestates; these are the states we can observe.

The physical eigenstates are written as

$$|P_1\rangle = \frac{1}{\sqrt{|p|^2+|q|^2}}\left(p|P^0\rangle + q|\overline{P^0}\rangle\right)$$
$$|P_2\rangle = \frac{1}{\sqrt{|p|^2+|q|^2}}\left(p|P^0\rangle - q|\overline{P^0}\rangle\right). \tag{1.15}$$

Solving for the eigenvalues of $\mathbf{H_{eff}}$, we find

$$\left(\frac{q}{p}\right)^2 = \frac{H_{21}}{H_{12}} = \left(\frac{M_{12}^* - \frac{i}{2}\Gamma_{12}^*}{M_{12} - \frac{i}{2}\Gamma_{12}}\right) \tag{1.16}$$

and the eigenvalues $\mu_{1,2}$ are

$$\mu_{1,2} = H_{11} \pm (H_{12}H_{21})^{\frac{1}{2}} = M_0 \pm (H_{12}H_{21})^{\frac{1}{2}} = M_{1,2} - \frac{i}{2}\Gamma_{1,2} \tag{1.17}$$

where

$$\begin{aligned} M_{1,2} &= \Re\mu_{1,2} \\ &= M_0 \pm \Re\,(H_{12}H_{21})^{\frac{1}{2}} \\ &= M_0 \pm \Re\left(\left(M_{12}^* - \frac{i}{2}\Gamma_{12}^*\right)\left(M_{12} - \frac{i}{2}\Gamma_{12}\right)\right)^{\frac{1}{2}} \end{aligned}$$

and

$$\begin{aligned} \Gamma_{1,2} &= \Gamma_0 \mp 2\Im\,(H_{12}H_{21})^{\frac{1}{2}} \\ &= \Gamma_0 \mp 2\Im\left(\left(M_{12}^* - \frac{i}{2}\Gamma_{12}^*\right)\left(M_{12} - \frac{i}{2}\Gamma_{12}\right)\right)^{\frac{1}{2}} \end{aligned} \tag{1.18}$$

Note that the signs "$\pm$" of the eigenvalues do not have to correspond to the signs denoting the eigenstates, due to the square root. The mass and width splittings

between the physical eigenstates are then

$$\begin{aligned} \Delta M &= M_- - M_+ = -2\Re\left(H_{12}H_{21}\right)^{\frac{1}{2}} \\ \Delta\Gamma &= \Gamma_- - \Gamma_+ = 4\Im\left(H_{12}H_{21}\right)^{\frac{1}{2}} \end{aligned} \tag{1.19}$$

For completeness, the lifetimes are then

$$\begin{aligned} \tau_{1,2} &= \frac{1}{\Gamma_{1,2}} \\ &= \frac{1}{\Gamma_0}\left(\frac{1}{1 \mp \frac{\Delta\Gamma}{2\Gamma_0}}\right) \end{aligned} \tag{1.20}$$

and the physical states evolve in time according to

$$|P_{1,2}(t)\rangle = e^{-iM_{1,2}t - \frac{1}{2}\Gamma_{1,2}t}|P_{1,2}(t=0)\rangle. \tag{1.21}$$

Let's take a moment to summarize this remarkable result. Particles are typically produced as eigenstates of flavor, but if they can mix, then the physical eigenstates they decay as are not the same as the states in which they were produced! The physical eigenstates have different masses, decay widths, and lifetimes than the eigenstates of flavor. Furthermore, there are two sources of mixing (the off-diagonal terms in the mass and decay matrices) and they describe very different physical processes; mixing through either real or virtual intermediate states, respectively. [3]

The limit of $CP$ invariance for $H$ (and therefore $\mathbf{H_{eff}}$) deserves further discussion. In this limit, $M_{12}$ and $\Gamma_{12}$ are real, resulting in $|q/p| = 1$. The physical

---

[3] We do not address the possibility of mixing through $\Delta P(= S, C, B) = 2$ "superweak" interactions.

eigenstates $|P_{1,2}\rangle$ become the eigenstates of $CP$, $|P_{\pm}\rangle$

$$|P_{\pm}\rangle = \frac{1}{\sqrt{2}}\left(|P^0\rangle \pm |\overline{P^0}\rangle\right) \tag{1.22}$$

with

$$\begin{aligned} CP|P_+\rangle &= \quad |P_+\rangle \\ CP|P_-\rangle &= -|P_-\rangle \end{aligned} \tag{1.23}$$

and from 1.19 the mass and width splittings between the physical eigenstates simplify to $|\Delta M| = 2M_{12}$ and $|\Delta\Gamma| = 2\Gamma_{12}$.

## 1.4 Using $CP$ Eigenstate Decays to Probe Mixing

In a $P^0 - \overline{P^0}$ system exhibiting mixing, the relative amount of constituent flavor (or equivalently, $CP$) eigenstates in an initial state can be probed with decays of the physical mass eigenstates into $CP$ eigenstate final states.

It is convenient to introduce dimensionless mixing parameters $x$ and $y$, which are defined as

$$\begin{aligned} x &\equiv \frac{\Delta M}{\Gamma_0} \\ y &\equiv \frac{\Delta\Gamma}{2\Gamma_0} \end{aligned} \tag{1.24}$$

We have already seen in Equation 1.21 that mixing manifests itself partly as a difference in lifetime between the flavor eigenstates $|P^0\rangle$ and $|\overline{P^0}\rangle$ and the physical mass eigenstates $|P_{\pm}\rangle$. So, how to observe mixing? We can interrogate the distribution of times in the decays of the states $|P^0(t)\rangle$, which is initially pure $|P^0\rangle$, and $|\overline{P^0(t)}\rangle$, which starts at $t = 0$ as pure $|\overline{P^0}\rangle$. Using equations 1.15 and 1.21 and normalizing $p$ and $q$ such that $|p|^2 + |q|^2 = 1$, we have

$$|P^0(t)\rangle = f_+(t)|P^0\rangle + \frac{q}{p} f_-(t)|\overline{P^0}\rangle$$
$$|\overline{P^0}(t)\rangle = \frac{q}{p} f_-(t)|P^0\rangle + f_+(t)|\overline{P^0}\rangle \tag{1.25}$$

where

$$f_+(t) \equiv e^{-iM_0 t - \frac{1}{2}\Gamma_0 t} \cos\left[\left(\Delta M - \frac{i}{2}\Delta\Gamma\right)\frac{t}{2}\right]$$
$$f_-(t) \equiv e^{-iM_0 t - \frac{1}{2}\Gamma_0 t} i \sin\left[\left(\Delta M - \frac{i}{2}\Delta\Gamma\right)\frac{t}{2}\right] \tag{1.26}$$

We define the amplitudes for the decays of the flavor eigenstates into a final state $f$ ($P^0 \to f$ and $\overline{P^0} \to f$) and its $CP$ conjugate state $\overline{f}$ ($P^0 \to \overline{f}$ and $\overline{P^0} \to \overline{f}$) as

$$A_f \equiv \langle f|H|P^0\rangle \qquad \overline{A}_f \equiv \langle f|H|\overline{P^0}\rangle$$
$$A_{\overline{f}} \equiv \langle \overline{f}|H|P^0\rangle \qquad \overline{A}_{\overline{f}} \equiv \langle \overline{f}|H|\overline{P^0}\rangle \tag{1.27}$$

then the decay amplitudes for the our physical eigenstates are

$$\langle f|H|P^0(t)\rangle = f_+(t)A_f + \frac{q}{p} f_-(t)\overline{A}_f$$
$$\langle f|H|\overline{P^0}(t)\rangle = \frac{p}{q} f_-(t)A_f + f_+(t)\overline{A}_f$$
$$\langle \overline{f}|H|P^0(t)\rangle = f_+(t)A_{\overline{f}} + \frac{q}{p} f_-(t)\overline{A}_{\overline{f}}$$
$$\langle \overline{f}|H|\overline{P^0}(t)\rangle = \frac{p}{q} f_-(t)\overline{A}_{\overline{f}} + f_+(t)\overline{A}_{\overline{f}}. \tag{1.28}$$

For convenience, we define the ratios

$$\lambda_f \equiv \frac{q}{p}\frac{\overline{A}_f}{A_f} \qquad \lambda_{\overline{f}} \equiv \frac{p}{q}\frac{A_{\overline{f}}}{\overline{A}_{\overline{f}}} \tag{1.29}$$

then the time-dependent decay rates are

$$\begin{aligned} R(P^0(t) \to f) &\propto |\langle f|H|P^0(t)\rangle|^2 \\ &\propto \frac{|A_f|^2 e^{-\Gamma_0 t}}{2}\Bigg[\left(1-|\lambda_f|^2\right)\cos\left(\Delta M t\right) \\ &\qquad + \left(1+|\lambda_f|^2\right)\cosh\left(\frac{\Delta\Gamma t}{2}\right) \\ &\qquad - 2\Im\left(\lambda_f\right)\sin\left(\Delta M t\right) \\ &\qquad + 2\Re\left(\lambda_f\right)\sinh\left(\frac{\Delta\Gamma t}{2}\right)\Bigg] \end{aligned}$$

$$\begin{aligned} R(\overline{P^0}(t) \to f) &\propto |\langle f|H|\overline{P^0}(t)\rangle|^2 \\ &\propto \frac{|A_f|^2 e^{-\Gamma_0 t}}{2}\left|\frac{p}{q}\right|^2\Bigg[\left(|\lambda_f|^2-1\right)\cos\left(\Delta M t\right) \\ &\qquad + \left(1+|\lambda_f|^2\right)\cosh\left(\frac{\Delta\Gamma t}{2}\right) \\ &\qquad + 2\Im\left(\lambda_f\right)\sin\left(\Delta M t\right) \\ &\qquad + 2\Re\left(\lambda_f\right)\sinh\left(\frac{\Delta\Gamma t}{2}\right)\Bigg] \end{aligned} \tag{1.30}$$

and for decays into $\overline{f}$ final states

$$\begin{aligned} R(P^0(t) \to \overline{f}) &\propto |\langle \overline{f}|H|P^0(t)\rangle|^2 \\ &\propto \frac{|\overline{A}_{\overline{f}}|^2 e^{-\Gamma_0 t}}{2}\left|\frac{q}{p}\right|^2\Bigg[\left(|\lambda_{\overline{f}}|^2-1\right)\cos\left(\Delta M t\right) \\ &\qquad + \left(1+|\lambda_{\overline{f}}|^2\right)\cosh\left(\frac{\Delta\Gamma t}{2}\right) \\ &\qquad + 2\Im\left(\lambda_{\overline{f}}\right)\sin\left(\Delta M t\right) \\ &\qquad + 2\Re\left(\lambda_{\overline{f}}\right)\sinh\left(\frac{\Delta\Gamma t}{2}\right)\Bigg] \end{aligned}$$

$$
\begin{aligned}
R(\overline{P^0}(t) \to \overline{f}) &\propto |\langle \overline{f}|H|\overline{P^0}(t)\rangle|^2 \\
&\propto \frac{|\overline{A}_{\overline{f}}|^2 e^{-\Gamma_0 t}}{2}\Bigg[\left(1-|\lambda_{\overline{f}}|^2\right)\cos\left(\Delta M t\right) \\
&\qquad + \left(1+|\lambda_{\overline{f}}|^2\right)\cosh\left(\frac{\Delta\Gamma t}{2}\right) \\
&\qquad - 2\Im\left(\lambda_{\overline{f}}\right)\sin\left(\Delta M t\right) \\
&\qquad + 2\Re\left(\lambda_{\overline{f}}\right)\sinh\left(\frac{\Delta\Gamma t}{2}\right)\Bigg] \qquad (1.31)
\end{aligned}
$$

It is obvious from the the equations above that the distribution of decay times generally deviates from a pure exponential, and the deviation is expressed in terms of the quantities which characterize mixing, $\Delta M$ and $\Delta\Gamma$. If $\Delta M$ and $\Delta\Gamma$ are both zero (no mixing), the distribution of decay times returns to a simple exponential.

If we return to the limit of $CP$ invariance, then $\left|\frac{p}{q}\right| = 1$. The rates in equations 1.30 (and 1.31) can be combined, resulting in

$$
\begin{aligned}
R(P^0(t) \to f) + R(\overline{P^0} \to f) &\propto |A_f|^2 e^{-\Gamma_0 t}\Bigg[\left(1+|\lambda_f|^2\right)\cosh\left(\frac{\Delta\Gamma t}{2}\right) \\
&\qquad + 2\Re\left(\lambda_f\right)\sinh\left(\frac{\Delta\Gamma t}{2}\right)\Bigg] \\
R(P^0(t) \to \overline{f}) + R(\overline{P^0} \to \overline{f}) &\propto |\overline{A}_{\overline{f}}|^2 e^{-\Gamma_0 t}\Bigg[\left(1+|\lambda_{\overline{f}}|^2\right)\cosh\left(\frac{\Delta\Gamma t}{2}\right) \\
&\qquad + 2\Re\left(\lambda_{\overline{f}}\right)\sinh\left(\frac{\Delta\Gamma t}{2}\right)\Bigg] \qquad (1.32)
\end{aligned}
$$

One can see that by studying the combined time-dependent rates, we are sensitive only to $\Delta\Gamma$. Similarly, by studying the difference in rates, we are sensitive to $\Delta M$. Further, if $f$ is a $CP$ eigenstate ($|\overline{f}\rangle = CP|f\rangle = \eta_{CP}(f)|f\rangle$), then the distribution of times (in the "combined" case) can be expressed as

$$R(P^0(t) \to f) + R(\overline{P^0} \to f) \propto 2|A_f|^2 e^{-\Gamma_0 t}\left[\cosh\left(\frac{\Delta\Gamma t}{2}\right) + \eta_{CP}(f)\sinh\left(\frac{\Delta\Gamma t}{2}\right)\right]$$
$$\propto 2|A_f|^2 e^{-\Gamma_0 t} e^{\eta_{CP}(f)\Delta\Gamma\frac{t}{2}}$$
$$\propto 2|A_f|^2 e^{-\Gamma_0(1-\eta_{CP}(f)y_{CP})t} \tag{1.33}$$

where the subscript $CP$ has been added to $y$ to denote that $CP$ invariance is assumed. We note this rate is again a simple exponential!

Also in the $CP$ conserving limit, we can regard $D^0$ decays to non-$CP$ eigenstates as equal admixtures of $CP$ even and odd components; call them $\overline{CP}$. We can then rewrite $y_{CP}$ as

$$y_{CP} = \frac{\tau_{\overline{CP}}}{\tau_{CP+}} - 1 \qquad \text{CP Even}$$
$$y_{CP} = 1 - \frac{\tau_{\overline{CP}}}{\tau_{CP-}} \qquad \text{CP Odd} \tag{1.34}$$

It is important to note that in the $CP$ conserving limit, $|P_+\rangle(|P_-\rangle)$ corresponds to $|P_2\rangle(|P_1\rangle)$.

So, in the limit of $CP$ invariance, mixing due to the difference in the widths of the physical eigenstates can be seen as the difference in lifetimes between a $CP$ eigenstate final state and another final state which is not a $CP$ eigenstate (or has different eigenvalue $\eta_{CP}$). This is our analysis. We compare the lifetimes of $CP$ even states $KK$ and $\pi\pi$ to that of $\overline{CP}$ state $K\pi$.

## 1.5 Theoretical Expectations for $y_{CP}$ and Current Experimental Limits

A large collection of theoretical $D^0 - \overline{D^0}$ mixing predictions are summarized in reference [7], covering a time range of nearly 20 years. There are several things to note about this these predictions. First, mixing predictions for $x$ and $y$ tend to be

small, and cover many orders of magnitude ($\approx 10^{-1} - 10^{-8}$ for either quantity). We expect both of these parameters to be small in the Standard Model; $x$ should be small because all the quarks in the box diagram have masses that are basically degenerate on the scale of $M_W$, and $y$ should be small because long distance effects are expected to be negligible [8]. Second, the upper limit of all mixing predictions is within reach of current experiments. Third, non-Standard Model physics tends to enhance the predictions for $x$. This is because such models tend to allow heavy particles into the box diagram. The prospects for $y$, on the other hand, do not improve with such the additions to the particle zoo [9].

A plot of current experimental limits on $y$ in the CP conserving limit ($y_{CP}$) from studies of $D$ meson decays into CP eigestates is shown in Figure 1.2. These results are documented in references [8, 10, 11]. The BELLE, FOCUS, the E791 $KK$ analyses are of the same style as the one presented here (though we use the $\pi\pi$ decay channel, as well). Therefore, these results are directly comparable to the one we present later. The tightest limits shown on Figure 1.2 come from FOCUS. Expressed as a 95% confidence level interval, FOCUS finds:

$$0.0034 < y_{CP} < 0.0650$$

This is not quite consistent with zero, which is very interesting. The FOCUS result is the first result to be even mildly inconsistent with zero.

Other analyses have also provided insight on $D^0 - \overline{D^0}$ mixing. The CLEO "wrong sign $D$" analysis [12] is not sensitive to $x$ or $y$ by themselves, but to the total mixing rate:

$$R_{mix} = \sqrt{x^2 + y^2} = \sqrt{x'^2 + y'^2}$$

where $x'$ and $y'$ are just $x$ and $y$ rotated by $\delta$:

$$x' = x\cos\delta + y\sin\delta$$
$$y' = y\cos\delta - x\sin\delta$$

and $\delta$ is a stong phase diference between the right- and wrong-sign $K\pi$ decay amplitudes. At the 95% confidence level, this result is:

$$(1/2)\ x'^2 < 0.00041$$
$$-0.058 < y' < 0.010$$

with no assumption about CP violation.

The E791 $K\ell\nu$ analysis [13] is sensitive only to $R_{mix}$; the limits derived from this analysis carves out a semi-circle in the $xy$ plane. They find

$$R_{mix} < 0.0050$$

at the 90% confidence level.

To summarize, with current experimental sensitivities (particularly from CLEO and FOCUS) in the few percent range, it may be that a mixing signal is just around the corner. If a signal is seen above the $10^{-3}$ level, it would favor a "new physics" explanation.

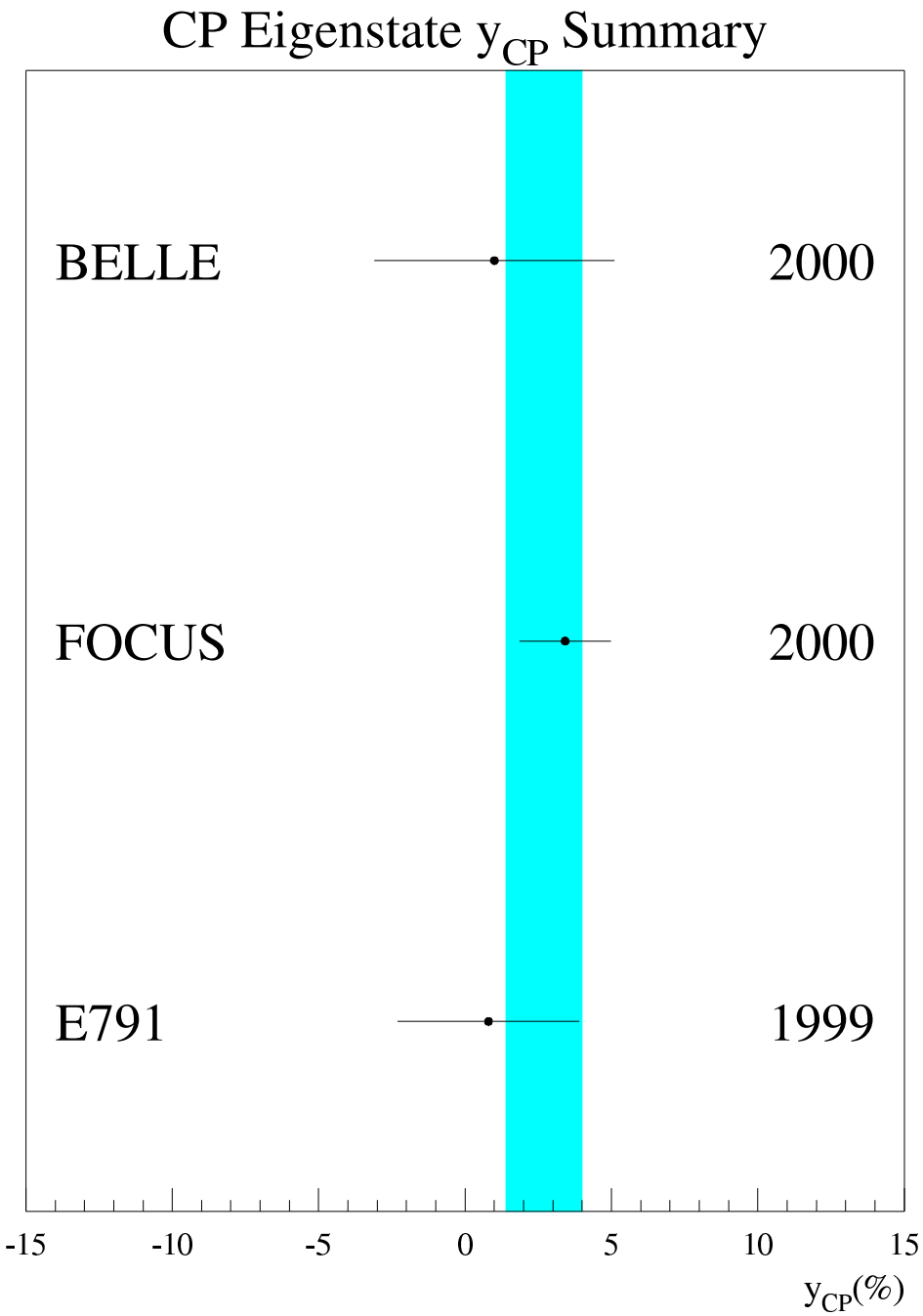


Figure 1.2: Experimental limits on $y_{CP}$ from CP eigenstate decays of $D$ mesons. The error bars shown are $1\sigma$ errors (the statistical and systematic errors added in quadrature).

# CHAPTER 2
# EXPERIMENTAL APPARATUS

The $D$ mesons we want to study are produced only in a high energy environment and decay very quickly into daughter particles which fly away at relativistic speeds. In order to study such particles, an environment capable of producing and detecting such particles and detecting must be created. There are tremendous technical challenges in creating such an apparatus and in analyzing the data which comes out of it. The solutions to these challenges are many, and as one might guess they have evolved over time as technology has progressed. As documenting the complete history of particle physics techniques is clearly beyond the scope of this work, we instead focus in this chapter on the apparatus used for this analysis, namely the CESR $e^+e^-$ collider and the CLEO detector.

## 2.1 The Cornell Electron Storage Ring

The Cornell Electron Storage Ring (CESR) is a circular electron-positron collider located at Cornell University's Wilson Laboratory in Ithaca, New York. The layout of Wilson Laboratory's accelerator facility is shown in Fig. 2.1.

CESR is staffed by accelerator physicists and students primarily involved in the development, operation, maintenance, and construction of accelerator machinery. CESR itself has been around for quite a long time; it has provided $e^+e^-$ collisions and synchrotron radiation for several experiments since it came online in 1979. During the decade of the 1990s, which is the time scale relevant for this analysis, $e^+e^-$ collisions occurred only in the south interaction region (at the bottom of Fig. 2.1), where the CLEO II detector is depicted.

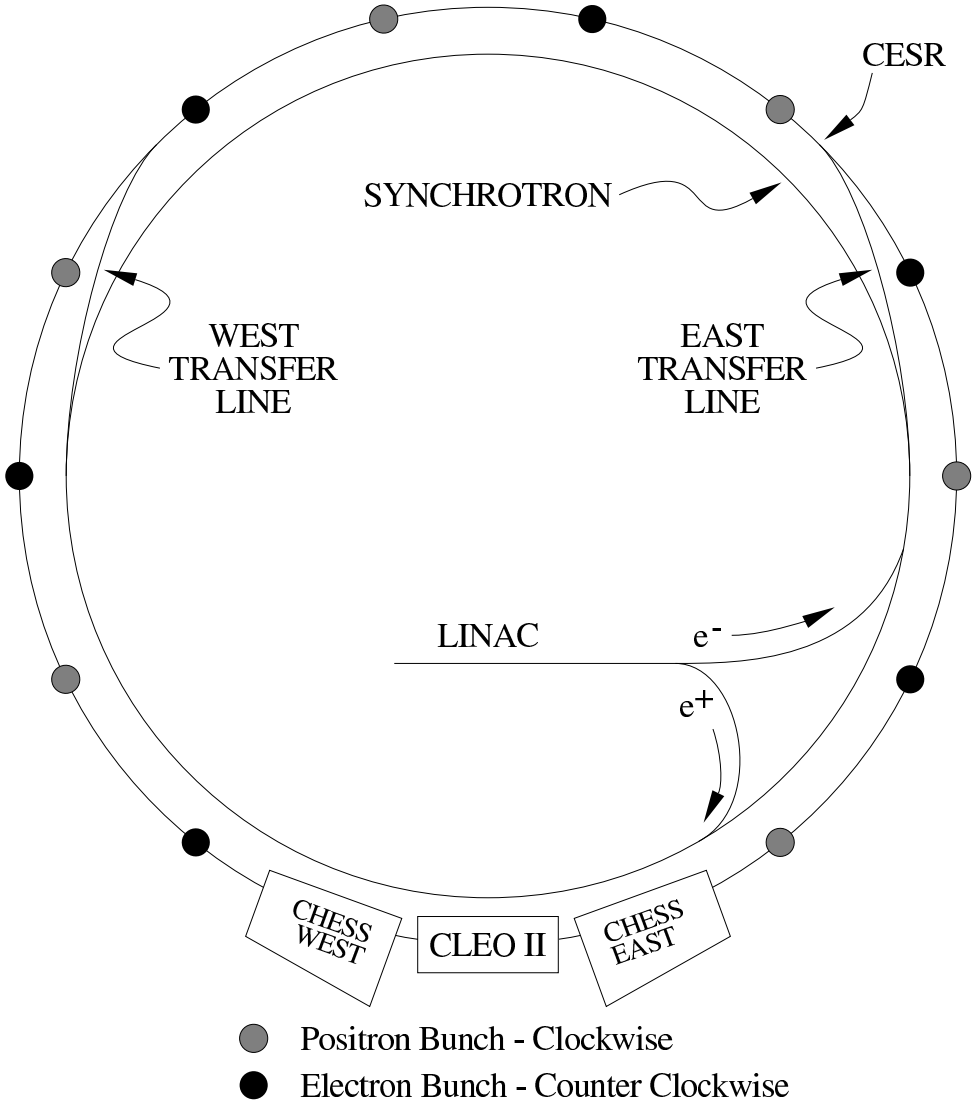


Figure 2.1: Schematic of the Wilson Laboratory accelerator facility. CESR and the synchrotron are in the same tunnel, about 40 feet beneath Cornell University's Alumni Fields. The circumference of CESR is 768 meters.

Running CESR in "HEP" (high energy physics) mode involves creating, accelerating, storing, and colliding beams of electrons and positrons so that the resident experiments can take data. These processes are accomplished serially and then repeated for several days or even weeks at a time. "HEP" mode is normally interrupted by scheduled periods of "machine studies" for study and experimentation with new running conditions (there is always something to learn and improve) as well as regular maintenance of the accelerator components; such down times typically last a few days. More extensive maintenance and upgrades to the accelerator requiring down times lasting a few to many weeks are less common, happening perhaps a couple times per year.

The act of creating, accelerating to operating energy, and storing of electron and positron beams is known as a "fill". Normally, the fill process entails the replenishing (or creation) of electron and positron currents lost to some nominal amount. Once the beams are then prepared for collision, or "tuned", collisions can begin. When in HEP mode, CESR provides colliding beams for a predetermined length of time; this is what is known as a "run". Over the years, the length of a run has varied somewhat, but has generally been on order of one hour. When a run is ended, the process begins again. During the 1990s, there were over 31,000 HEP runs.

As Fig. 2.1 suggests, CESR is composed of several major components, each of which performs a specific function in the arduous task of creating $e^+e^-$ collisions. These components and their purpose are described in the subsections below.

### 2.1.1 Linear Accelerator

In order for $e^+e^-$ collisions to occur, electrons and positrons must somehow be produced in the first place. This is the job of a special 30 meter section of vacuum pipe called the Linear Accelerator (LINAC), and the process is called "filling" the synchrotron. The fill procedure is sequential: positrons first, then electrons.

The positron filling procedure is as follows. First, electrons are created by boiling them off of a filament wire located at the back of the LINAC (the electron gun), just like inside the picture tube of a television. These electrons are accelerated by electromagnetic fields in a series of Radio Frequency Acceleration Cavities (RF Cavities) towards a tungsten target located about halfway down the LINAC. The collision between the 140 $MeV$ electrons and the target creates a spray of electrons, positrons, and photons. The electrons are cleared away with magnetic fields and the positrons are accelerated down the remainder of the LINAC, ultimately reaching an energy of about 200 $MeV$. At the end of the LINAC, the positrons are introduced into the synchrotron. The electron filling procedure is identical, except that the tungsten target is moved out of the way; the conversion process is not necessary, as we already have electrons from the electron gun. The total filling time for electrons and positrons in normal running conditions is about 10 minutes.

We skipped an important detail. The astute reader probably noticed the tremendous bulbs on the CESR ring in Fig. 2.1 labelled "Positron Bunch" and "Electron Bunch". No, they are not really that big; the bunches of positrons and electrons fit quite comfortably inside of all of CESR's vacuum pipes. The electron and positron beams are not continuous; instead they are grouped in bunches. The creation of these bunches begins in the LINAC's "prebuncher" component. The prebuncher is a short series of cavities positioned immediately outside the electron gun. When filling the electrons and positrons, the electron gun is fired repeatedly; each pulse resulting in a stream of electrons approximately 3 feet long. The electron pulses are compressed in the prebuncher with electromagnetic fields to the width of a dime.

### 2.1.2 Synchrotron

The synchrotron is a circular accelerator in which electrons and positrons from the LINAC are accelerated to operating energy. The electrons and positrons and travel inside a vacuum pipe in opposite directions (viewed from above, electrons go

counterclockwise, and the positrons clockwise) in circular orbits. Steering is accomplished via magnetic field, and acceleration by radio frequency electromagnetic field. As the particles' speed increases, these fields must be adjusted in a synchronized manner to keep the radius of the orbit constant.

For most of the circumference of the ring the particles travel in vacuum between the poles of bending magnets, arranged in 192 3-meter long sections. At four places in the ring the beam passes through a 3-meter long linear accelerator. After approximately 4000 laps around the synchrotron (about 1/100th of a second), electron and positron bunches have reached operating energy, about 5.3 GeV each, and are ready for injection into the storage ring.

### 2.1.3 Storage Ring

The positron and electron beams are transferred into the storage ring (CESR) via transfer lines that connect the synchrotron to CESR. This process is known as "injection". There is one transfer line for positrons ("west") and one for electrons ("east"). At this point, the electron and positron buches are travelling at speeds over 99.9999995% of the speed of light. The purpose of the storage ring is to keep the beams of electron and positron bunches constant and at the same time arrange for a high rate of $e^+e^-$ collisions in the interaction region.

The storage ring uses the same guide field principle as the synchrotron; that is, particles travel in a (roughly) circular orbit in vacuum under the influence of a magnetic field. Each electron or positron spends less than one-hundredth of a second in the synchrotron, but once it is transferred to the storage ring it must coast there for up to several hours. This puts very strict demands on the precision of the ring of magnets and on the quality of the vacuum. The electrons and positrons can strike and scatter off of any gas molecules they encounter in the beampipe. If there are too many gas molecules, this ultimately leads to loss of the beams. Therefore, the

residual air in the path of the beam particles must be kept about one hundred million times less dense than in the normal atmosphere.

The orbits of the electrons and positrons bring them into collision only at the interaction region (at the center of the CLEO detector). As mentioned above, a magnetic fields are used to make the particle orbits roughly circular; a total of 86 dipole-type magnets are used to accomplish this. Another 106 quadrupole magnets are used to keep the beams focused, as we wish the particles to remain in tight bunches. A small number of sextupole and octupole magnets make subtle corrections to the orbits. The sequence of dipoles and quadrupoles repeats itself around the 768 meter circumference of the ring.

The particles coasting around the storage ring radiate a beam of X-rays like a headlight on a train, losing about 1.2 $MeV$ per turn around the ring. The power level of this "synchrotron radiation" is about half a megawatt. It strikes the vacuum chamber in a narrow stripe, depositing energy on the vacuum chamber wall. The heat generated must be carried away by water circulating through a channel in the vacuum chamber wall. The lost energy is restored to the circulating beam by radio-frequency (RF) cavities similar to those in the synchrotron and linac, although the beam is not actually accelerated. The RF system operates at a frequency of 500 million cycles per second (MHz) and is powered by a system rather like a television transmitter. The intense synchrotron radiation is not simply a useless byproduct of acceleration; it is used for experiments in the CHESS area (to the left and right of CLEO in Fig 2.1).

We have previously stated that electrons and positrons travel around the storage ring in bunches, as opposed to a continuous stream. In fact, there is actually finer structure than this. The bunch structure is more appropriately described as equally spaced trains with up to five cars each that can be populated with electrons and positrons. In each train (or "bunch-train"), the cars are closely spaced, about 14 ns apart. This fact requires that when the beams are ultimately crossed in the interaction

region, that they cross at an angle in order to prevent "parasitic" crossings away from the nominal interaction point. In the 1990s, CESR ran with nine trains of electrons and positrons and up to three cars populated with approximately around $1.5 \times 10^{11}$ particles each (mid-1990s running). At 5.3 $GeV$, the cars are circling the storage ring at 396 kHz. It should be noted that CESR developed the idea of bunch-train operations and was the first accelerator to use them in production. It is one of many $e^+e^-$ collision rate enhancement techniques CESR has come up with which has been adopted at other laboratories, including CERN, SLAC, and KEK.

Certainly, we do not want the beams to collide anywhere besides the interaction region (where the detector is), so the orbits are not perfect circles. Large capacitors called "horizontal separators" are used to knock the bunches slightly out of the circle, the species moving in opposite directions. In the end, the orbits are shaped like a pretzel.

The behavior of collections of charged particles in a storage ring is a complicated field of its own, whose details are certainly beyond the scope of this work. Suffice it to say that we have not discussed many of the important effects which complicate the operation of a real-world storage ring, or the technically challenging solutions which must be implemented to make it all work. To that end, the CESR staff has constructed a system with sophisticated computer control, monitoring, and feedback systems which communicate with the magnets and the RF system in all of the accelerator components.

#### 2.1.3.1 Interaction Region

The interaction region (IR) is where the electron and positron bunches pass through each other, which they do about 3.6 million times per second. The IR is in a special segment of the accelerator vacuum system; it is the part which passes through the heart of the CLEO detector. Indeed, this beam pipe is as much a part of CLEO as it is of CESR. This is because the particles created in an $e^+e^-$ annihilation must

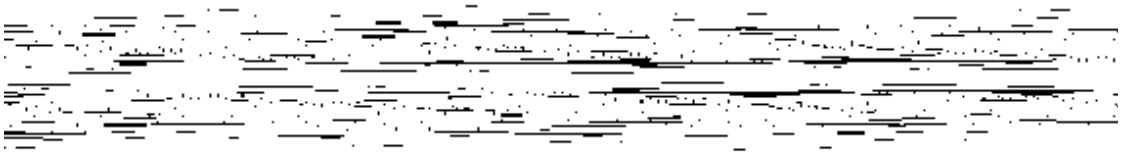

Figure 2.2: The CLEO II.V beam pipe.

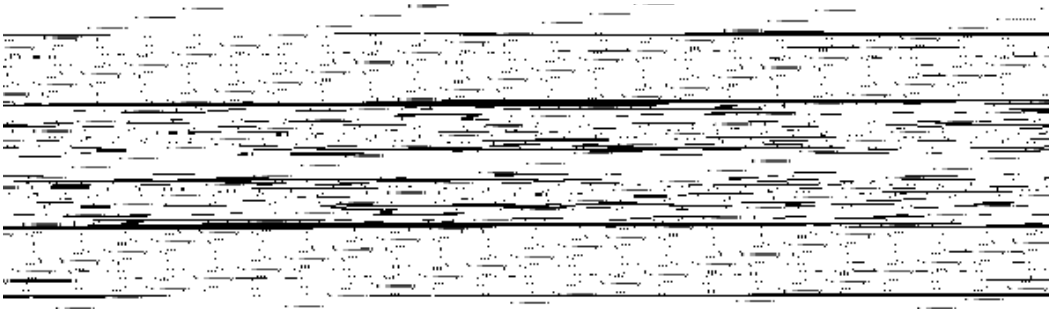

Figure 2.3: The CLEO II.V beam pipe surrounded by the Silicon Vertex Detector and Vertex Detector.

first pass through the walls of this segment of the beam line before encountering the instrumented CLEO detector material. The pipe is therefore made of a low mass material and is very thin in order to reduce scattering. If this were not the case, charged particles emerging from the $e^+e^-$ interaction point and subsequently tracked in the CLEO tracking system would not point back to the place they began. There were two beam pipes used during the CLEO II's lifetime. The first version was used from 1989 to 1995; it had an inner radius of 3.5 centimeters and was 0.5 millimeters thick. The second was installed as part of "Phase II" of the CESR/CLEO Upgrade Project [18] in the summer of 1995. The inner radius of the beam pipe was reduced to 1.875 centimeters, and the thickness was approximately 1 millimeter. The second beam pipe was actually double-walled, so it isn't actually twice as thick as the previous version. Between the walls, water was used for cooling in order to compensate for the extra heat resulting from higher beam currents. Both beam pipes were made of beryllium. Figures 2.2 and 2.3 show pictures of the second version of the beam pipe.

If the accelerator is performing well, a high collision rate is the result. Indeed, the ability to have a high collision rate is crucial for the success of an accelerator and the experiments it serves. The figure of merit is then the number of possible collisions per second per unit area; this is called the luminosity. The higher the luminosity, the larger the rate for $e^+e^-$ collisions. And the larger the number of collisions, the larger the data samples we have to study. The luminosity is given as

$$\mathcal{L} = fn\frac{N_{e^+}N_{e^-}}{A} \tag{2.1}$$

where $f$ is the frequency of revolution for each train, $n$ is the number of populated cars in each train for each particle species, $A$ is the cross-sectional area of the cars, and $N_{e^+}$ and $N_{e^-}$ are the numbers of positrons and electrons per car, respectively.

In order to maximize the luminosity, the beams are focused to be as small as possible at the IR. Typically, each car is about 2 cm long (along the beamline), 300 $\mu$m wide (in the plane of the ring), and 8 $\mu$m high (normal to the ring). Over time, CESR has found ways to increase the luminosity while retaining stable running conditions by adding more current (increase $N_{e^+}$ and $N_{e^-}$) and filling more cars ($n$). Fig. 2.4 shows the CESR luminosity hisory, as seen by the CLEO II.V experiment.

During the 1990s, CESR held and constantly improved upon the world record for luminosity until the February 1999 shutdown for the next incremental upgrade to the machine and the CLEO detector. The highest luminostiy achieved by CESR before the shutdown was $8.0 \times 10^{32} cm^{-2} sec^{-1}$, exceeding the Phase II design goal by 33%. The excellent performance of CESR during this time allowed the accumulation of far more data than at any other experiment. There are many accelerators of higher energy than CESR, but there are none which even came close to the luminosity CESR delivered in this time. All this on a tight budget to boot. In the future, however, CESR will have to fight hard for the luminosity crown with new accelerators online at

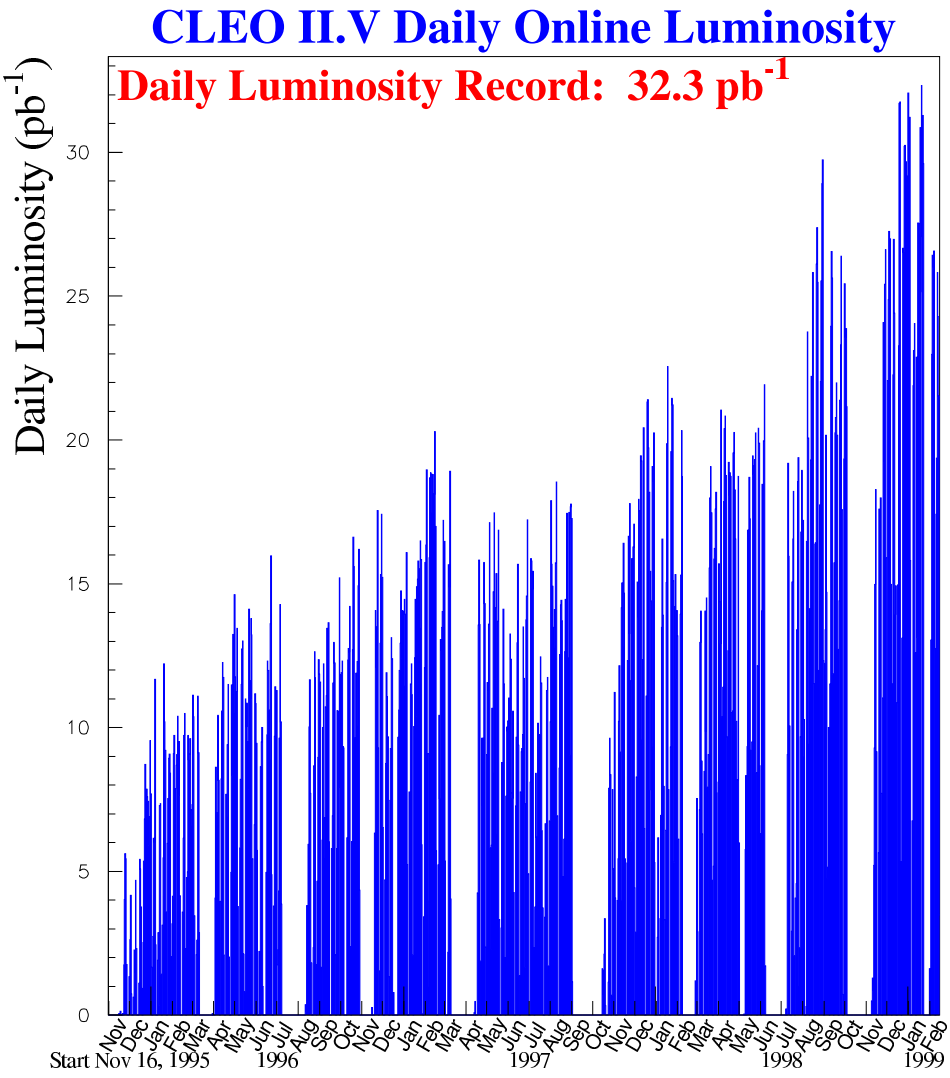


Figure 2.4: Daily luminosity delivered to the CLEO II.V experiment.

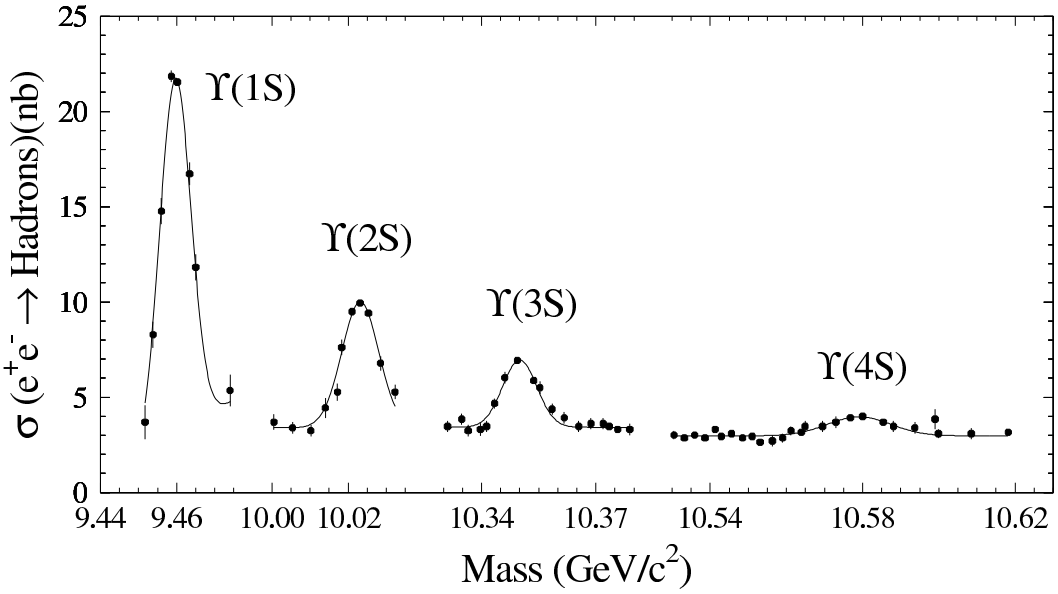


Figure 2.5: Cross section versus Mass.

SLAC and KEK. At the time of this writing, the new PEP-II storage ring at SLAC has shattered the CESR record by attaining luminosity of $1.43 \times 10^{33} cm^{-2} sec^{-1}$. Meanwhile, the Phase III upgrade of CESR has been installed is being commissioned.

## 2.2 The Upsilon System

Why is the CESR beam energy 5.3 $GeV$? As one might imagine, there is a very good reason for this.

As originally designed, CESR could run at center of mass energies as high as 16 $GeV$. However, at a fixed target experiment at Fermilab in 1977 the $\Upsilon$ family of resonances was discovered. These resonances are shown in Fig. 2.5. Though the Fermilab experiment was unable to resolve the members of this new family as separate entities, they were immediately believed to be the bound states of a new flavor, bottom, just as the observation of the $J/\psi$ signalled the discovery of charm. CESR's first achievement was the resolution of the first three states in $\Upsilon$ family; the $\Upsilon$(1S), $\Upsilon$(2S), and $\Upsilon$(3S). Discovery of the $\Upsilon$(4S) followed shortly in 1980. The $\Upsilon$(4S) turns out to be a very interesting state indeed.

In Fig. 2.5, one can tell that there is an obvious difference in the widths between the $\Upsilon$(4S) and the $\Upsilon$(1S), $\Upsilon$(2S), or $\Upsilon$(3S). This implies that the $\Upsilon$(4S) has decay channels open to it that the others do not have. These decay modes are $B^+B^-$ and $B^0\overline{B^0}$, which the $\Upsilon$(4S) is just massive enough to produce. $\Upsilon$(4S) decays nearly 100% of the time to $B^+B^-$ and $B^0\overline{B^0}$ in approximately equal proportions. This makes the $\Upsilon$(4S) an ideal laboratory to study the characteristics of the $B$ meson, and is why CESR runs with the beam energies it does.

Fig. 2.5 is interesting for another reason. One can see that the $\Upsilon$ resonances are all sitting on a considerable amount of hadronic "background". This background is composed primarily of $e^+e^- \rightarrow q\overline{q}$, where $q$ is a light quark ($udsc$). We call this process "continuum". There is also some contribution from $e^+e^- \rightarrow \tau^+\tau^-$, where one of the $\tau$ leptons decays into hadronic products. Hadronic data collected at the $\Upsilon$(4S) os dominated by continuum, where the cross section outnumbers that of $B\overline{B}$ production by about 4:1.

CESR spends about 2/3 of its time running on the $\Upsilon$(4S) resonance, with the remainder of the time spent just below it. This is done in order to collect large amounts of data we know contains no $B$ mesons. The study of the continuum is very important to $B$ meson analyses. A $B$ meson physicist ultimately wishes to remove the continuum as much as possible; the continuum-only data is an independent data sample which allows them to study how to best go about that.

But in this analysis, the tables are reversed. We want to measure the $D^0$ lifetime. To do so, we need to know where it starts with high precision. For $D$ mesons which are decay products of $B$ mesons, we cannot measure the $D$ production point ($B$ decay vertex) without reconstructing the $B$ meson, which simply cannot be done with high efficiency. Therefore it is the continuum which is interesting to us, and the $B\overline{B}$ events are a background we must find a way to remove from our data sample.

## 2.3 The CLEO Experiment

In an $e^+e^-$ annihilation at CESR energies, the vast majority of the time the $e^+e^-$ interact electromagnetically, creating a photon [1]. This interaction, like all others, must conserve energy and momentum. The produced photon then has energy which is the sum of the energies of the $e^+$ and $e^-$ (in the neighborhood of 10.58 $GeV$), and a very tiny momentum, as the incident $e^+$ and $e^-$ momenta nearly cancel each other out. The energy of a particle is related to its rest mass and momentum through the relativistic energy-momentum equation, written as

$$E = \sqrt{p^2 + m^2} \tag{2.2}$$

This means that the photon produced from an $e^+e^-$ collision at CESR has mass. This is a common situation in an $e^+e^-$ collider; indeed this fact is exploited in the design of such facilities. Such a photon, written as $\gamma^*$, is referred to as "off mass shell" or as a "virtual" photon because real photons have mass of zero (see Table 1.3). Virtual photons are unstable, and decay immediately into "real" (or "on shell") daughters. It is at this point we enter the world of particle detectors.

Particle detectors everywhere have at least one thing in common; they are made of matter. As we described in Chapter 1, matter can interact with other matter. Particle detectors are sensitive to such interactions and are instrumented to record information about the interaction. Using this information, humans can determine some of the properties of the incident particle, such as its energy, momentum, and mass.

---

[1] Recall from Table 1.2 that $e^+$ and $e^-$ both have weak isospin, and can interact weakly. It is certainly true that, even though CESR's energy scale is small compared to the mass of the $Z^0$, an $e^+e^-$ annihilation could result in an off-shell $Z^0$. However, the ratio of the electromagnetic to weak coupling constants is large, so electromagnetic interactions dominate

There are many ways in which the $\gamma^*$ can decay. In this analysis, the process of interest is $e^+e^- \rightarrow \gamma^* \rightarrow hadrons$ [2], where one or more of the hadrons or its decay products is a $D^0$ (or $\overline{D^0}$) meson. The $D$ mesons themselves are unstable, and quickly decay into lighter particles. It is these particles that we detect.

In this analysis, we use the CLEO II.V detector to find the daughters of the $D$ mesons. In the following sections, we discuss some of the particle detection schemes and techniques implemented in the CLEO detectors, and how the raw detector data is transformed into measurements of particle energy, momenta, and trajectories.

### 2.3.1 The CLEO II Detector

The CLEO II detector is a versatile, general purpose detector of cylindrical geometry with excellent charged particle and photon detection capabilities. It is thoroughly described in reference [14]. As implied by the name, CLEO II is not the only CLEO detector which has existed. CLEO II was preceded by CLEO I.V and the original CLEO detectors. Compared with the previous versions of CLEO, CLEO II was a major upgrade, with many detector elements replace with new ones.

A side view of CLEO II is shown in Fig. 2.6, and a close up view of one quadrant is shown in Fig. 2.7. As one can see, CLEO II is a composite of many detector elements. These subdetectors are typically arranged as concentric cylinders centered around the beam pipe. The entire detector is approximately cube shaped, with one side measuring about 6 meters, and weights over 1000 tons. CLEO II operated in this configuration from 1989 to 1995.

---

[2] The hadronization mechanisms describing the production of hadrons from the $\gamma^*$ will not be discussed in this document. Suffice to say that $e^+e^- \rightarrow \gamma^* \rightarrow hadrons$ is just one of the many processes possible in $e^+e^-$ annihilation, and is the process of interest in this analysis.

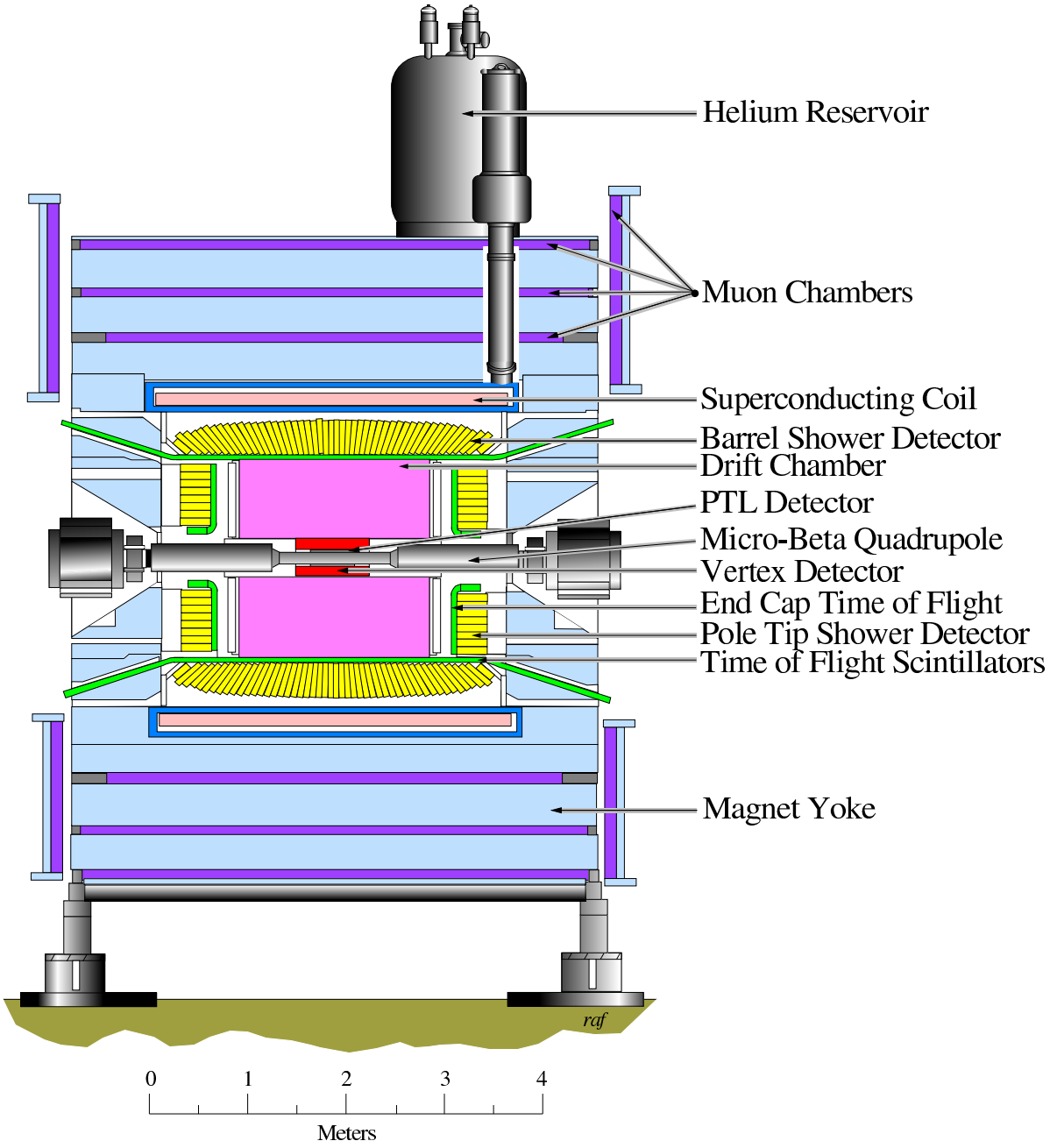


Figure 2.6: A side view of the CLEO II detector.

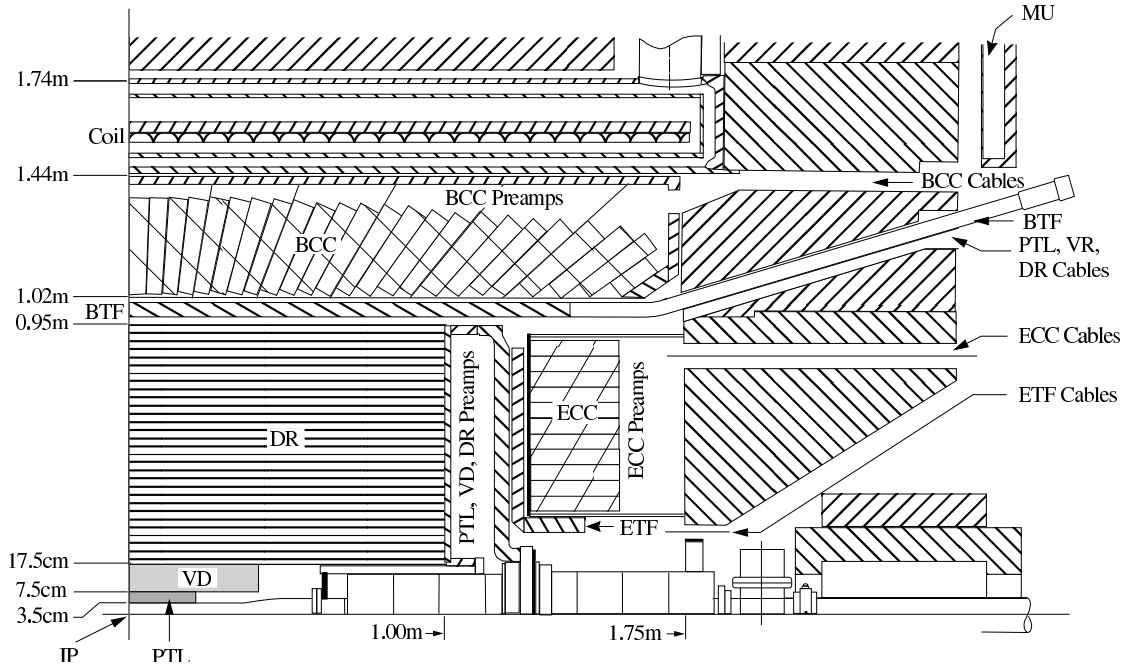


Figure 2.7: A side view of a quadrant of the CLEO II detector.

It will be useful at this point to define the coordinate system relavent to the CLEO detector. The $x$ direction points south of the ring at the interaction point, $y$ points upwards, and $z$ is the direction of the positrons (west). The azimuthal angle $\phi$ is defined in the canonical way, with $\phi = 0$ along the $+x$ direction. The polar angle $\theta$ is measured from the positive $z$ axis.

#### 2.3.1.1 Superconducting Coil

All the CLEO detector subsystems except for the muon chambers are located inside a superconducting coil. The purpose of the coil is to provide the 1.5 Tesla magnetic field used to bend the paths of charged particles in the tracking system. The magnetic field points in the $-z$ direction (east). By measuring how much a charged particle bends, experimenters can measure the momentum of the particle. The helium reservoir shown in Fig. 2.6 at the top of CLEO II contains the liquid helium required to keep the coil in a superconducting state.

#### 2.3.1.2 Charged Particle Tracking System

After particles from the interaction point pass through the beam pipe, they begin to encounter the active detector elements of the tracking system. In CLEO II, there are three main components of the tracking system, all designed to measure a charged particle's position at various points along its trajectory; the tracking system is not sensitive to particles with no electric charge. The tracking system's components all fall into a category of tracking devices known as drift chambers. As a result, they all have the same principle behind their operation.

A drift chamber is a volume of gas (typically a mixture of organic and inert gases) with an array of anode wires and cathode wires[3] or metallic surfaces running through it. The anodes are kept at high (positive) voltage, which provides an electric field throughout the chamber. The cathodes are held at ground, and shape the electric field so that fields from neighboring anode wires do not interfere with each other. The wires are often arranged in "drift cells" centered on the anode. Typically, there are several to many layers of such cells in a drift chamber, with each layer containing many individual cells arranged in an appropriately symmetric geometry.

As a charged particle passes through the chamber, it interacts electromagnetically with the gas molecules in the chamber in a process called ionization; that is, an incident charged particles ionizes gas molecules along its trajectory. The electrons from the ionized gas molecules then "drift" in the electric field toward the nearest anode wire. As the electron gets very close to the anode, the electric field becomes very strong which causes an avalanche whereby further ionization is induced. The result of the avalanche is a tremendous number of electrons collapsing upon the wire

[3]Anode and cathode wires are often called "sense" and "field" wires, respectively. I will use anode and sense, and cathode and field, interchangeably.

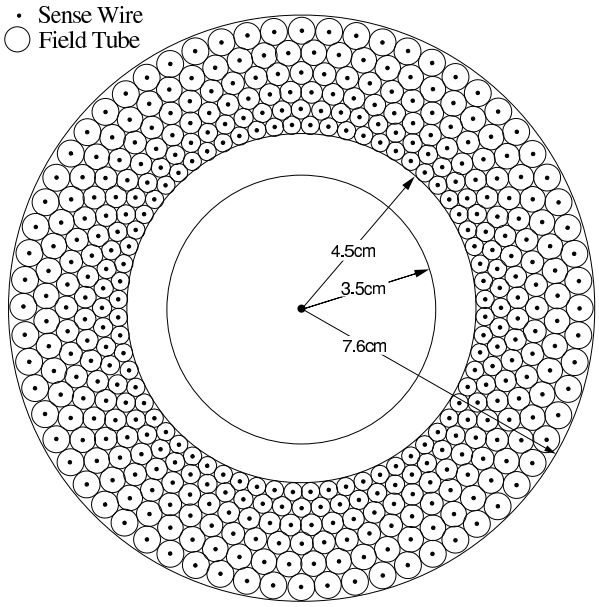


Figure 2.8: Cross Section of the Precision Tracking Layers.

in a very short amount of time (less than one nanosecond). When this happens to a sense wire, we say that the wire is "hit".

The current on the anode wire from the avalanche is collected and amplified by electronics at one or both ends of the anode wire. Typically, an ADC and a TDC is found among the components of a drift chambers' readout electronics. The ADC measurement corresponds to the amount of charge collected on the wire, and the TDC measurement corresponds to the "time" of the hit. A calibration is determined that maps the ADC values into specific ionization measurements of the incident particle, thereby providing some information on the particle's mass and species. A calibration is also found to turn the TDC values into drift distances; that is, the distance of closest approach an incident particle makes to the anode wire (see [16] for further discussion).

The innermost tracking chamber in CLEO II is the Precision Tracking Layers, also known as the "PT" or "PTL". A cross section of the PTL is shown in Fig. 2.8. The PTL is a six layer device, with 64 straw tubes per layer. Each tube has an anode

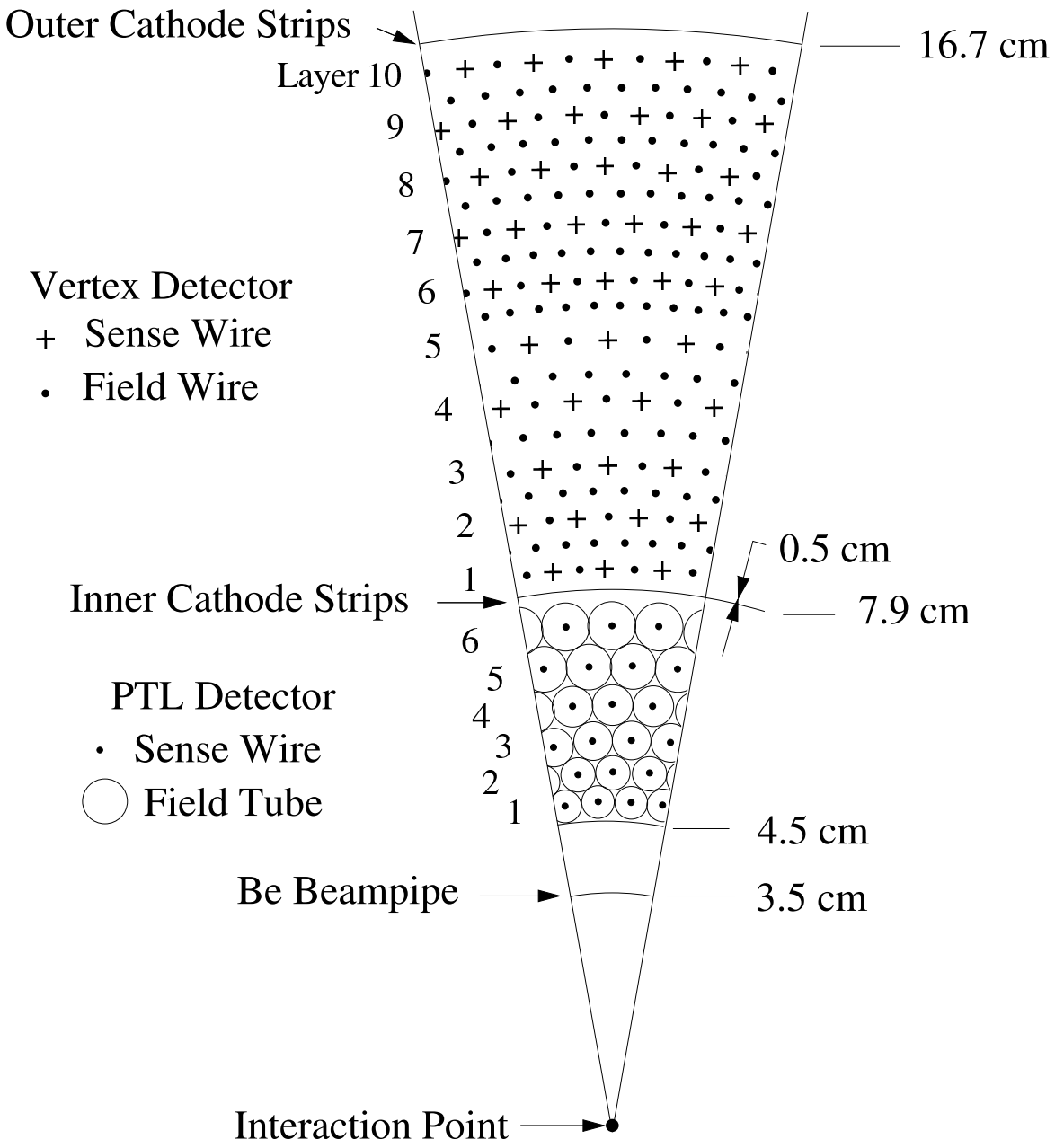


Figure 2.9: The Vertex Detector anodes.

wire going down the middle of it. The anode wires are gold-plated tungsten, with a diameter of 15 $\mu$m. The tubes themselves are compose of aluminized mylar. The tubes are all glued together, with pieces of G10 plastic functioning as endplates to hold the anodes. During CLEO II, there were two gases used in the PTL tubes. At first, a 50-50 mix of argon and ethane was used. In 1992, the gas was switched to dimethyl ether, which gives better position resolution. The PTL sense wires are only capable of making $r - \phi$ measurements.

After exiting the PTL, the next device a particle encounters is the Vertex Detector (VD). The layout of the VD wires are shown (with the PTL inside) in Fig. 2.9. The VD is a bit different than the PTL - it is not a straw tube device. Wires are used instead of tubes to define the boundaries of the drift cells. This reduces the amount of material an incident particle has to go through (and is a lot cheaper), but has more complicated isochrones (an isochrone is the collection of points in a cell whose drift times are the same). There are 10 layers of hexagonal drift cells in the VD, with 64 cells per layer in layers 1-5, and 96 cells per layer in layers 6-10, for a total of 800 drift cells in all. The sense wires are composed of a nickel-chromium alloy, and field wires of gold-plated aluminum. The diameter of the sense wires is 20 $\mu$m. There are two thicknesses of field wires used in the VD; the thicker 162.5 $\mu$m diamter wire is used in layers 1, 2, 6, and 7, and 142.2 $\mu$m diameter wire is used everywhere else. The gas is a 50-50 mix of argon-ethane. Gas is introduced into the VD through through four "gas holes" in layer 5. The cells occupied by the gas holes do not contain sense wires. The endplates through which the wires are threaded and gas introduced are again made of G10, and the inner and outer walls of the device are carbon filament tubes.

The VD sense wires are instrumented on both ends of the wire. This allows $z$ measurements to be made via the "charge division" method. For further details

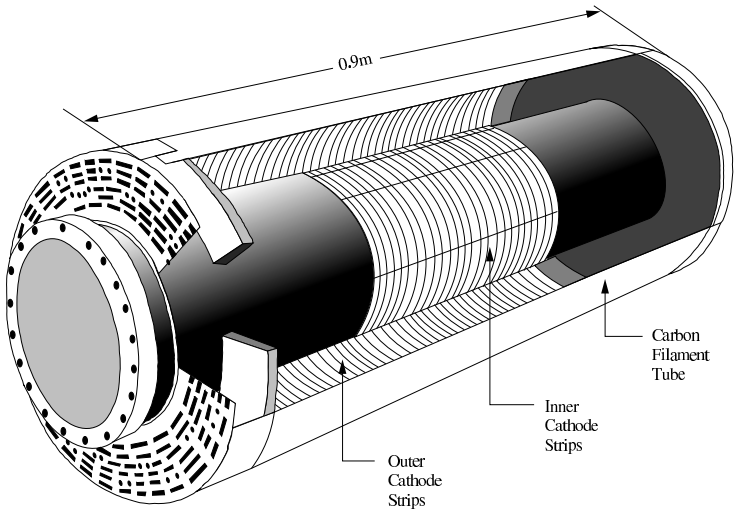


Figure 2.10: The Vertex Detector cathodes.

Table 2.1: Parameters of Vertex Detector cathode layers.

| Layer | # of $\phi$ segments | # of $z$ segments | Pad size in $z$ (mm) |
|---|---|---|---|
| VD Inner | 8 | 64 | 5.85 |
| VD Outer | 8 | 96 | 6.85 |

regarding charge division see reference [17]. The VD sense wires of course can make $r-\phi$ measurements, as well.

The VD also has segmented cathode strips on the surface of the inner and outer walls of the chamber. These are shown in Fig. 2.10. The segmentation is in $\phi$ and $z$, though it is much finer in $z$ in order to make $z$ position measurements along a charged particle's trajectory. The cathode strips also serve to shape the sense wire's field cage in layers 1 and 10 on the inner and outer edges, respectively. A table parameters describing the VD cathode layers is displayed in Table 2.1.

The outermost tracking chamber is the main drift chamber, or just DR. The layout of the DR anode wires are shown in Fig. 2.11. It is much large in volume than the inner two tracking devices. A total of 12,240 sense and 36,270 field wires are arrange in 51 layers of roughly square cells. The number of cells per layer is

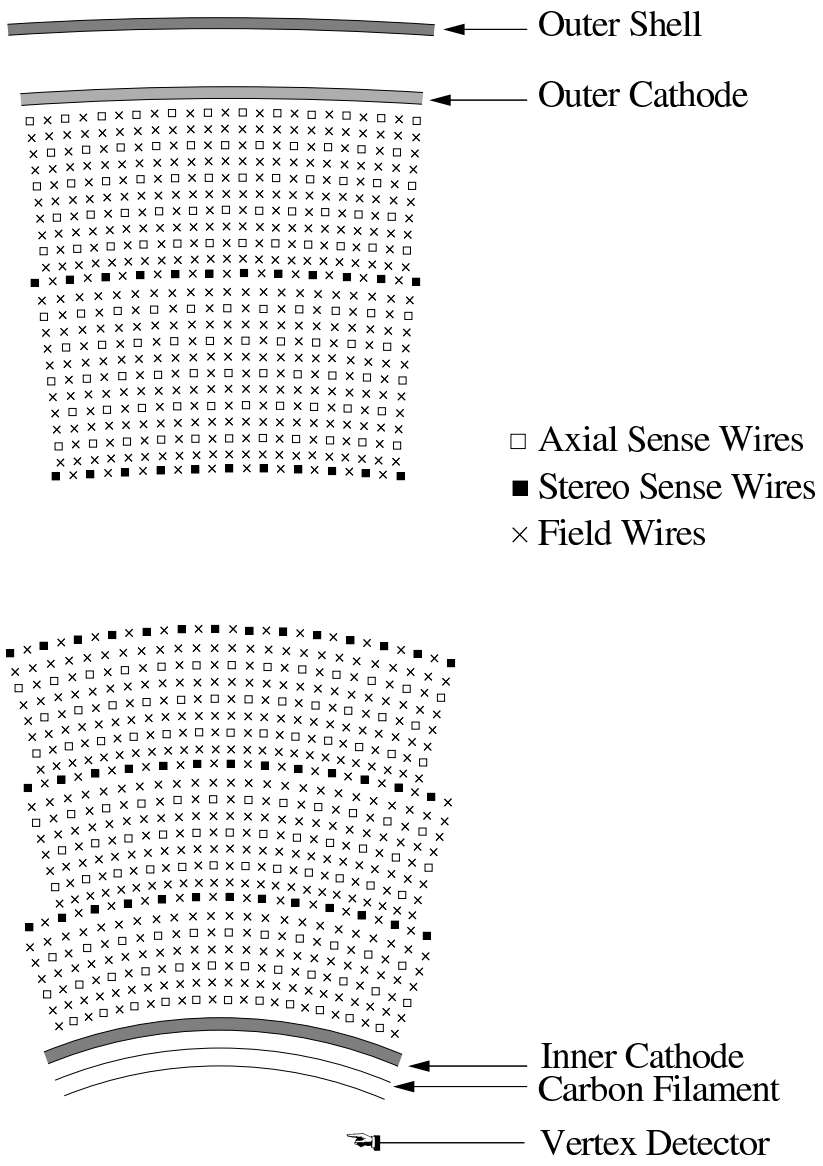


Figure 2.11: The Drift Chamber anodes.

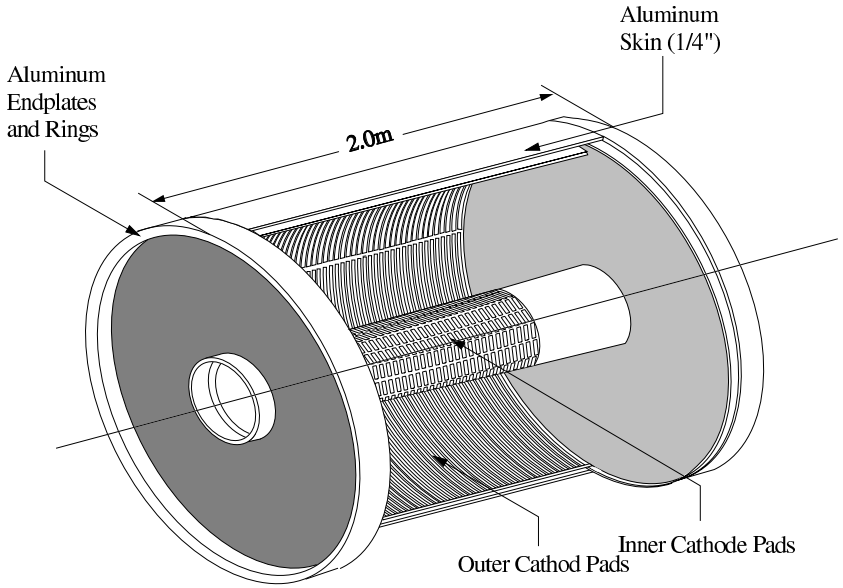


Figure 2.12: The Drift Chamber cathodes.

such that the cell size is approximately constant. Forty of the 51 layers have their sense wires parallel to the beam line ($z$ axis), but 11 layers are so-called "stereo" layers and have their sense wires strung at a small "stereo" angle to the $z$ axis. The stereo layers are then able to provide some measurement of the $z$ position along a track's path. The down side of the stero angle approach is that position resolution is easily harmed by the fact that the cell's isochrones are a function of $z$. This makes calibration of the drft time-to-distance relationship more difficult (and it is already difficult). The sense wires are 20 $\mu$m diameter gold-plated tungsten. There are again two types of field wires. Field wires in DR layers 1 through 40 are 110 $\mu$m diameter gold-plated aluminum, and in layers 41 through 51 are 110 $\mu$m diameter gold-plated copper-beryllium. The wires are supported by 3.175 cm thick aluminum endplates, and the gas in the chamber is again the 50-50 mix of argon-ethane. The inner wall of the chamber is a carbon filament reinformed epoxy tube, and the outer wall is a composite of panels.

As in the VD, segmented cathode surfaces shape the field cage on the inner surface of the innermost layer and on the outer surface of the outermost layer. The

Table 2.2: Parameters of DR cathode layers.

| Layer | # of $\phi$ segments | # of $z$ segments | Pad size in $z$ (mm) |
|---|---|---|---|
| DR Inner | 16 | 96 | 10.00 |
| DR Outer | 8 | 192 | 9.50 |

DR cathodes are shown in Fig. 2.12, and a table describing their parameters is shown in Table 2.2.

#### 2.3.1.3 Time of Flight System

The time of flight system is composed of a series of plastic scintillators and is arranged as two endcaps and a barrel. As the name suggests, the purpose of this systme is to measure the time a particle spends "in flight"; i.e. the time a particle takes to travel from the interaction point to the scintillators. Time of flight information is used in several ways; to trigger the detector, to identify the which car in the train a collision came from, and to provide a means of particle identification.

In the barrel section there are 64 scintillators, each 10 cm wide and 279.4 cm long. The angular coverage of the barrel region is $\theta$ between 35 and 145 degrees. In each endcap there are 28 pie-slice shaped scintillators arranged around the beam pipe covering polar angles between 18 and 37 degrees on the west side, and 143 to 162 degrees on the east. The scintillators are all about 5 centimeters thick. The tiny amount of overlap between the barrel and endcap systems can be seen most easily in Fig. 2.7.

#### 2.3.1.4 Crystal Calorimeter

The crystal calorimeter is composed of 7800 thallium-doped CsI crystals, and like the time of flight, is arranged as two endcaps and a barrel. The barrel contains 6144 crystals, and each one is pointed towards the interaction point so that photons originating there strike the barrel crystal faces at nearly normal incidence (this can

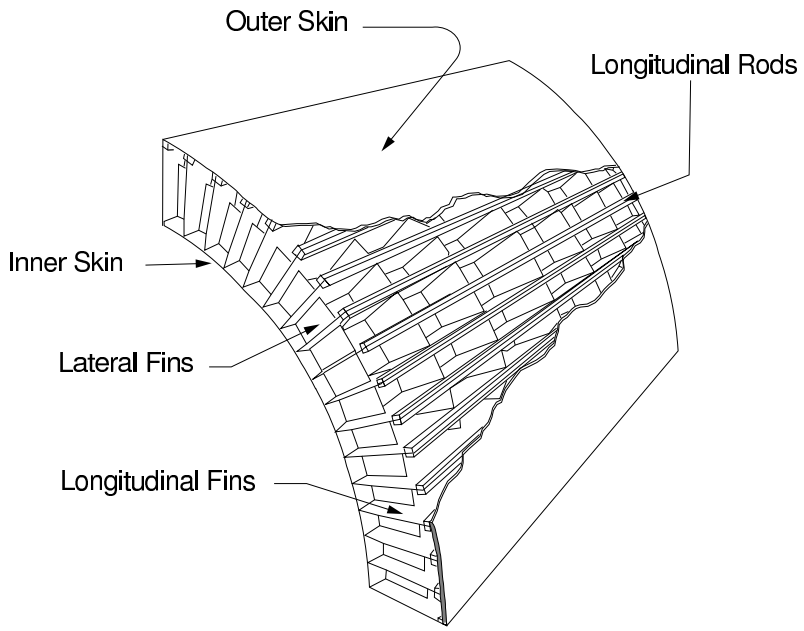


Figure 2.13: Crystal Calorimeter Barrel.

be seen in Figures 2.6 and 2.7). The 828 crystals in each endcap are aligned with the $z$ axis. Each crystal is approximately 5 cm square and 30 cm long.

Photodiodes are attached to the back of each crystal to convert light into electrical signals. For redundancy, there are four photodiodes per crystal. When the crystals are read out, a mixer/shaper card sums the four signals from each crystal and shapes the signal for input into an ADC.

A section of the barrel crystal holder is shown in Fig. 2.13. A quadrant of an endcap crystal holder shown in Fig. 2.14.

#### 2.3.1.5 Muon System

Like the crystal calorimeter and time of flight systems, the muon system is arranged as two endcaps and a barrel. The purpose of the muon system, as the name implies, is to identify the passage of a muon.

The muon detectors are plastic streamer counters that are approximately 5 m long and 8.3 cm wide. The counters are placed in between layers of iron, which only mouns can penetrate with high efficiency. In each gap between the iron, there are

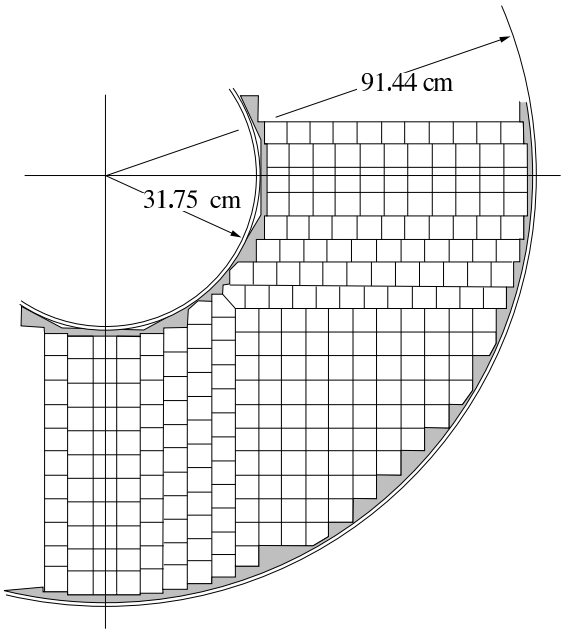


Figure 2.14: Crystal Calorimeter Endcap.

three layers of counters. Each counter contains eight compartments containing an anode wide and is filled with a 50-50 mix of argon-ethane gas. The anode wires are 50 $\mu$m in diameter, and are made of silver-plated copper-beryllium. Each anode is surronded on three sides with graphite cathodes, and within a counter, all the anode wires are ganged together. When a hit is recorded, the anode wire position provides the $\phi$ coordinate of the hit, and charge division is used to extract the $z$ coordinate.

### 2.3.2 The CLEO II.V Detector

After a several month shutdown for the installation of the Phase II CESR/CLEO Upgrade, CLEO II.V began taking data in November 1995. This upgrade included the replacement of the beam pipe as mentioned in Section 2.1.3.1, as well as the removal of the PT and installation of a new tracking device to take its place: the Silicon Vertex Detector (SVX). The SVX is described in reference [19]. A diagram of it is shown in Fig. 2.15.

The SVX is not a drift chamber; it is a silicon strip detector, and the means of operation are quite different from those of the tracking devices we have discussed

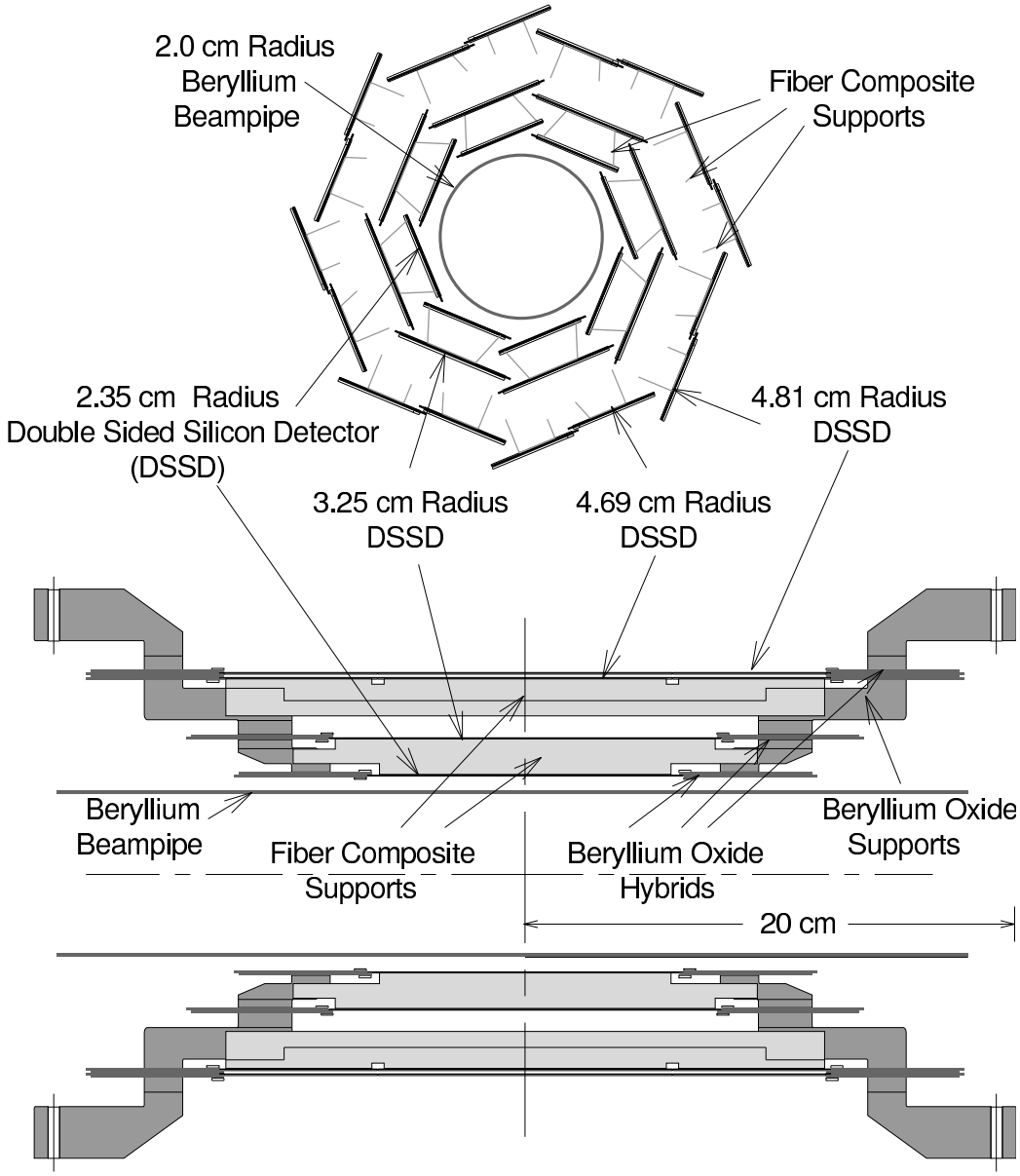


Figure 2.15: The CLEO II.V Silicon Vertex Detector.

so far. The SVX is a three layer device consisting of 96 silicon wafers, each 300 $\mu$m thick. As shown in Fig. 2.15, the wafers are arranged into octants; each octant has 12 wafers. The octants can be seen in the $r-\phi$ view to overlap each other slightly in the corners, and results in tracks which can have hits on two different wafers in a layer. This is useful in aligning the detector. A thorough summary of the parameters describing the SVX can be seen in Table 2.3.

The wafers are instrumented and read out on both sides; hence the name "Double Sided Silicon Detector" (DSSD) used in Fig. 2.15. The instrumentation on each side consists of an array of aluminum strips on the wafer surface. These strips are ultimately connected to preamplifiers stationed at the end of the detector. On the top of the wafer (facing away from the beam line), the aluminum strips sit atop $p$ type implants, with strips and implants parallel to the beam. On the bottom of a wafer (facing the beam line), the strips connect to $n$ type implants, with strips and implants perpendicular to the beam. The entire wafer forms a $p-n$ junction. When reverse bias is applied across the wafer, a sensitive region depleted of mobile charge is formed.

Charged particles traversing the wafer lose energy as in any other material. In the sensitive region of a silicon wafer, this lost energy is used to create electron-hole pairs. Approximately 3.6 $eV$ is required to create a single electron-hole pair, much lower than the ionization energy in drift chamber gases (40 to 100 $eV$). For minimum ionizing particles in the CLEO SVX, this translates to about 21,000 pairs. The electrons and holes then travel (in opposite directions) in the electric field applied by the bias to the surfaces of the wafers and end up on the strips. In this way, the appearance of charge on a strip (a "hit" strip) indicates the passage of a charged particle. Since the strips on the top of the wafer ($p$ side) are parallel to the beam, they provide measurements of the $\phi$ location of the track at the center of the wafer (this is why the top of the wafer is called the $r-\phi$ side). Similarly, the strips on the

bottom of the wafer ($n$ side) measure the $z$ position and motivate the term $z$ side referring to the bottom of a wafer.

Previously, we mentioned that the readout electronics are mounted on the ends of the detector. On the $r-\phi$ side, the strips run parallel to the beam line, making readout a straightforward process. However, the $z$ side strips themselves are perpendicular to the beam. Reading them out directly would require the front end electronics to be placed in the tracking volume, leading to increased multiple scattering as charged particles interacted with the material of the electronics. Increased multiple scattering results in degradation of tracking resolution. So instead, the $z$ side strips are connected to traces which carry the signals to the ends of the detector. Each trace is connected three strips thereby "ganging" the strips together. Ganging leads to ambiguity in which strip actually collected charge, and therefore makes tracking more difficult. The ganged strips are spaced far apart to minimize this effect. However, this significantly reduces the number of channels the front end electronics has to deal with.

In all, the SVX contains 26,208 "read out" strips, or active channels. This is more than the rest of the channels in the entire detector combined. To read out the entire detector every event would slow down the data aqcuisition system to a crawl. Therefore, the events are sparsified online which drops channels which do not have any charge. Unlike the sparsifiers used in the other detector subsystems which are implemented in hardware, the SVX sparsifier is a program that runs on the same Motorola 68040 CPU chips found in older Apple and Amiga personal computers. The advantage of running a software sparsifier is that its algorithm can be changed easily. The disadvantage is that it is not as fast as a sparsifier implemented in hardware.

Other changes resulting the Phase II upgrade included changing the gas in the DR from the 50-50 mix of argon-ethane to 60-40 helium-propane. The helium-propane mixture has better position resolution due to the greater number of primary

ions created per unit length of cell traversed (bigger hydrocarbon molecules). In addition, hit efficiency at the edge of a drift cell was improved [20]. Another change was the installation of multi-hit electronics on one side of the VD as part of research and development for the Phase III upgrade [21]. Though these electronics were not used for tracking, their presence (or rather the removal of the old electronics) did have some effect on CLEO II.V tracking performance; the multihit electronics do not have ADCs. This makes the method of charge division impossible for assigning a $z$ measurement to a VD hit. In CLEO II, tracking of low momentum charged particles often relied on charge division hits to provide this $z$ information.

The major effect in the Phase II upgrade, however, was brought on by installation of the SVX. Exchanging the PT for the SVX provided significant improvements to the tracking system. This is for two reasons. First, the SVX measures both the $r-\phi$ and the $z$ position of a track with a single layer. The PT, on the other hand, had no ability to make a $z$ measurement at all. Second, the position resolution afforded by the SVX is much better than the PT, even in $r-\phi$ where the PT was already the highest resolution tracking device, far better than the VD or DR. The improvement in the $z$ and $\theta$ resolution on a charged particle's trajectory is dramatic. The result is that after the Phase II upgrade, CLEO is in an excellent position to make precision lifetime measurements short-lived particles.

Table 2.3: Silicon Vertex Detector parameters.

| | Layer 1 | Layer 2 | Layer 3 |
|---|---|---|---|
| Radius to inner surface | 23.5 mm | 32.5 mm | 46.9,48.1 mm |
| Total length | 65.580 mm | 81.270 mm | 2×65.580 mm |
| Total width | 22.568 mm | 30.128 mm | 2×22.568 mm |
| Active length | 59.535 mm | 76.356 mm | 2×59.525 mm |
| Active width | 21.168 mm | 28.890 mm | 2×21.168 mm |
| cos$\theta$ coverage | 0.92 | 0.92 | 0.92 |
| Thickness | 300 $\mu$m | 300 $\mu$m | 300 $\mu$m |
| Number of DSSD detectors | 16 | 16 | 64 |
| Number of CAMEX chips | 96 | 128 | 96 |
| Number of JAMEX chips | 0 | 0 | 96 |
| Readout bond pad pitch | 97 $\mu$m | 97 $\mu$m | 97 $\mu$m |
| Number of active channels | 6048 | 8064 | 12096 |
| Detector Outer Side ($r$-$\phi$, $\sigma = 12\mu$m) | | | |
| Implant | | p-type | |
| Number of implants | 753 | 1005 | 3012 |
| Implant width | 10 $\mu$m | 10 $\mu$m | 10 $\mu$m |
| Implant pitch | 28 $\mu$m | 28.5 $\mu$m | 28 $\mu$m |
| Readout width | 5 $\mu$m | 5 $\mu$m | 5 $\mu$m |
| Readout pitch | 112 $\mu$m | 114 $\mu$m | 112 $\mu$m |
| Readout strips | 189 | 252 | 378 |
| Detector Inner Side ($r$-$z$, $\sigma = 30\mu$m) | | | |
| Implant | | n-type | |
| Number of implants | 567 | 756 | 1134 |
| Implant width | 20 $\mu$m | 20 $\mu$m | 20 $\mu$m |
| Implant pitch | 105 $\mu$m | 101 $\mu$m | 105 $\mu$m |
| Approximate Barrier Width | 69 $\mu$m | 65 $\mu$m | 69 $\mu$m |
| Readout width | 5 $\mu$m | 5 $\mu$m | 5 $\mu$m |
| Readout pitch | 105 $\mu$m | 101 $\mu$m | 105 $\mu$m |
| Readout strips | 189 | 252 | 378 |

# CHAPTER 3
# ANALYSIS TECHNIQUE

In order to measure the mixing parameter $y$ in the $D^0\overline{D^0}$ system, we must obtain a large statistics sample of $D^0$ and $\overline{D^0}$ decays into $CP$ eigenstate final states, and measure a proper time for each $D^0$ or $\overline{D^0}$ parent. In this chapter, we describe the data samples used, the global event requirements imposed, and the selection criteria and technique used to choose and reconstruct such a sample. As the purity of the sample is an important issue, it is worth noting that a reconstructed $D^0$ or $\overline{D^0}$ candidate is just a candidate. We have no way of knowing whether or not it is real. Therefore, the efficiency of our selection criteria and their ability to reject false candidates ("background") is discussed.

## 3.1 Data Samples and Event Selection

The data used in this analysis were collected by the CLEO II.V detector. We use full sample of 9.0 $fb^{-1}$ taken on and near the $\Upsilon$(4S).

The data in this sample is logically divided into datasets, each of which corresponds to several months of data-taking; typically a few thousand runs. A boundary between datasets is created when changes that can affect either detector acceptance or resolution are imposed (such as opening the detector pole tips for maintenance).

The most detailed monte carlo simulation used in this analysis is based on GEANT [22], which incorporates a full detector simulation and response. The statistical advantage over the data is $\approx 8.25$ for the $KK$ and $\pi\pi$ samples, and $\approx 6$ for $K\pi$. The simulation included a proper luminosity-weighted sampling of the entire CLEO II.V dataset. This will account for run-dependent effects, such as variation in beam energy and calibration constants, to the best of our ability.

Most of the $e^+e^-$ collisions at this energy do not result in events containing hadrons, and are not interesting to this analysis. Therefore, we impose the following requirements to choose events likely to contain hadrons:

- The number of reconstructed charged tracks required to be $\geq 3$.
- If the number of charged tracks is 3 or 4, the total energy deposited in the calorimeter must be less than 65% of the beams' center of mass energy, $E_{CM}$, or the highest energy shower in the calorimeter must be less that 60% of $E_{beam}$.
- The total visible energy must be greater than 20% of $E_{CM}$.
- The total calorimeter energy must be greater than 15% of $E_{CM}$ or number of charged tracks greater than 4.
- Primary vertex position is required to be within 2 cm of origin in CLEO world coordinate system in $xy$, and within 7.5 cm in $z$.

The above criteria retain over 95% of *udsc* and more than 99% of $B\overline{B}$ events, while removing more than 99% of the ubiquitous $e^+e^- \to e^+e^-$ and $e^+e^- \to e^+e^-\gamma$ events.

As the performance of the tracking system is paramount in this analysis, we demand that the confidence level for the indentification of which car of the CESR bunch train the $e^+e^-$ annihilation orinated from is more than 0.5. This cut is $\approx$ 100% efficient for hadronic events. If the wrong car was selected, this would insert an incorrect offset of order of tens of nanoseconds (how much depends upon what car the event originated from and what car was mistakenly identified) into the determination of drift times, resulting in extremely poor tracking resolution.

## 3.2 Building Blocks

Excepting for some "uninteresting" types of events, we do not normally observe (detect) all the particles created by an $e^+e^-$ annihilation. Indeed, these "uninteresting" types of events are what our event selection criteria (described in Section 3.1) are designed to throw away! In the events which survive our selection criteria, the result of the $e^+e^-$ annihilation is usually the creation of many particles. Some of these particles leave evidence of their existence inside CLEO's various detector elements, and some do not.

A stable particle may not be directly observable by CLEO for many reasons. Maybe the particle simply does not interact sufficiently with the CLEO detector material in order for its trajectory to be detected - this is case with neutrinos, for example. Or perhaps the direction of the particle is such that it never traverses any of CLEO's detector elements - i.e., the particle escapes down the beam pipe. These are "missing" particles, and it is crucial for certain analyses (not this one) to employ techniques to try to recover such cases [28]. But there is another important reason a particle may not be directly detected by CLEO - it is not stable, and decays before encountering any of CLEO's detectors. For this class of particles, it may still be possible to "reconstruct" the momentum of the unstable particle and position of the decay point - if the daughter particles are detected.

In a High Energy Physics analysis, one build high level objects from more primitive ones. An example of this is the construction of tracks from the the low level hit information provided by the tracking chambers. The reconstruction of particle candidates is logically very similar - just as a track can be thought of as the "sum" of the hits used to form it, a particle which decays into a number of daughters can be viewed as the sum of those daughters. Applying the reconstruction methodology iteratively, complex decay chains and even entire events can be fully reconstructed.

In our $D^0$ reconstruction, the detected daughters of the $D^0$ decay are our "building blocks" for the $D^0$. For the $D^0$ decays we are interested in, those building blocks are $K$ and $\pi$ charged particles. Their selection criteria is described below.

## 3.3 Charged Particle Selection

The CLEO II.V detector's tracking chambers generally provide excellent momentum and position resolution for charged particle candidates. However, measuring the lifetime of a particle so short-lived as the $D^0$ is a hard business, and is near the limit of CLEO's resolution. We therefore use high quality track candidates to reconstruct the $D^0$.

To choose charged particle candidates of good quality, we require candidates to be successfully Kalman fit - this requirement ensures that the track parameters have proper ionization energy-loss corrections and the errors on the track's trajectory are reasonable. Tracks also must have mean residuals in the drift chamber of less than 1 mm. As the position resolution of a drift chamber hit is about 180 $\mu$m, this requirement removes only very poorly measured tracks.

As position information is paramount in lifetime determination, we demand each $D^0$ daughter candidate have two hits in each view ($r\phi$ and $rz$) of the highly position-sensitive SVX.

We also do not consider tracks whose momentum is less than 250 MeV as $D^0$ daughter candidates, as our simulation tells us that there are very few such candidates. Since low momentum charged particles tend not to have their trajectories reconstructed as well as high momentum particles, this criteria also removes some poorly measured candidates.

"Dredge" seeds are track candidates found by the pattern recognition in a last-ditch attempt to use all hits in the tracking system. Any hits left over from the more reliable pattern recognition methods are "dredged" into track candidates. These candidates tend to be complete figments of the tracker's imagination. Tracks whose seeds are from the "dredge" level of the pattern recognition are not considered, as "dredge"-ing is prone to making tracks which do not correspond to a real particle. Further, we demand that the tracks be approved by the track quality package TMNG, which removes yet more pattern recognition anomolies.

Finally, we demand that charged particle candidates are not part of a well identified $K^0_S$, $\Lambda$, or $\gamma$ conversion.

### 3.4 Neutral $D$ Meson Reconstruction

A $D^0$ candidate is formed by combining the 4-momenta of a set of vertex constrained charged particle candidates, which have passed the selection criteria of Sec-

tion 3.3; we consider all possible pairs of oppositely charged tracks under the $\pi^+\pi^-$, $K^+\pi^-$, $K^-\pi^+$, and $K^-K^+$ hypotheses. A covariance matrix describing the errors on the $D^0$ momentum and decay vertex position is calculated from the covariance matrices of the daughters.

To reduce the number of $D^0$ candidates from random combinations of tracks, we seek out $D^0$ candidates which come from the decay $D^{*+} \to D^0\pi_s^+$. To build the $D^*$ candidate, we trace the direction of the $D^0$ candidate's trajectory back from the reconstructed decay vertex to the beam spot. The $(x, y, z)$ coordinates along the $D^0$ trajectory that are most consistent with the beam (using the beam's covariance matrix) are identified, and a $\pi_s$ candidate is forced through this point. The selection of the $\pi_s$ candidates is the same as outlined in Section 3.3, except that the momentum requirement is lowered to 50 MeV, and we do not demand any SVX information. A $D^*$ candidate is the built from the refit $\pi_s$ and the undisturbed $D^0$ trajectories. This procedure improves the resolution on the mass difference, $\Delta m = m_{D^*} - m_D$ dramatically. We demand that $|\Delta m| = |m_{D^*} - m_D|$ is within 1 MeV of it's nominal value of 145.4 MeV.

A cartoon depicting of the construction of $D^0$ and $D^*$ candidates is shown in Figure 3.1.

In order to ensure $D^0$ candidates of good quality and to reduce background from random charged particles, we require the probability of vertex chi-squared for the $D^0$ decay vertex be greater than $10^{-3}$.

In CLEO's environment, a $D^0$ flies on order of 200 $\mu$m before decaying. This is not very far, and means that the $D^0$ decay vertex is very near to the high number of tracks emerging from the event's primary vertex (where the $e^+e^-$ collision took place). This means that many charged particles originating from the primary vertex pass our vertex quality selection criteria whether they come from from a $D$ meson or not. This kind of combinatoric background is mostly populated by low momentum

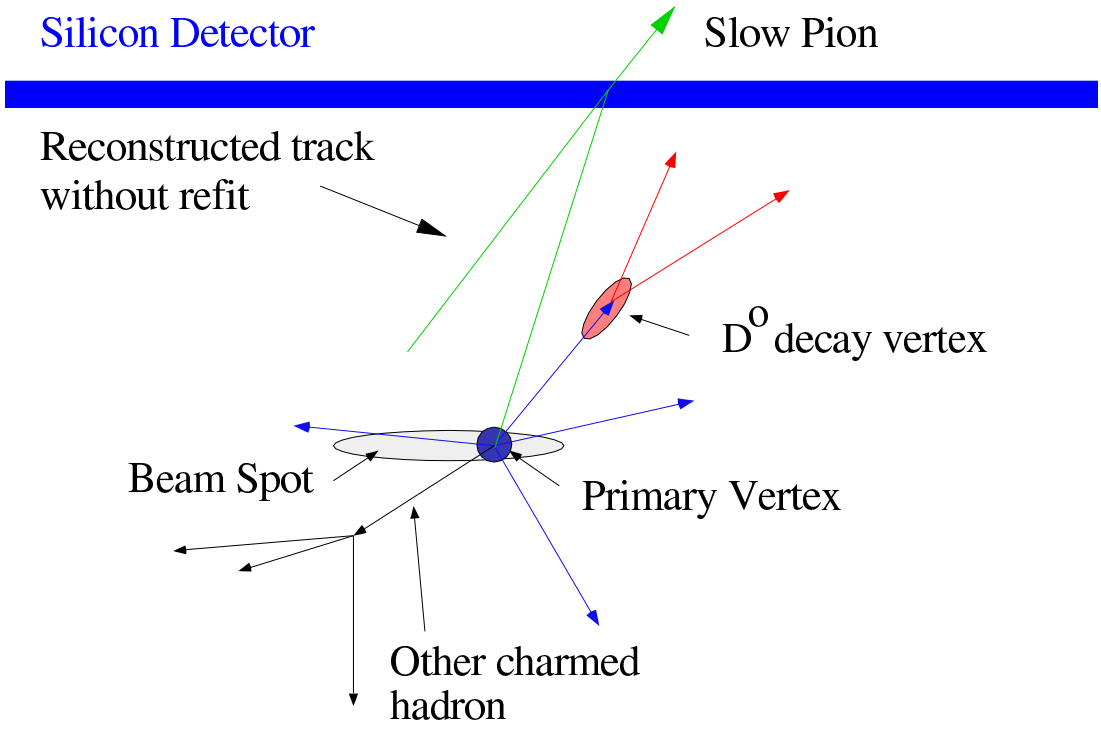


Figure 3.1: Diagram of $D$ and $D^*$ candidate reconstruction.

particles (whose errors are largest, and are therefore most likely to be "happy" to be constrained to the slightly displaced $D$ meson vertex). We can remove most of this background by cutting on $|cos(\theta^*)|$, where $cos(\theta^*)$ is defined by:

$$cos(\theta^*) = \frac{\vec{p}\,'_{dau} \cdot \vec{p}_D}{|\vec{p}\,'_{dau}||\vec{p}_D|} \tag{3.1}$$

and $\vec{p}\,'_{dau}$ is the momentum of one of the daughter tracks (we choose the one whose charge matches that of the $\pi_s$ candidate) in the rest frame of the $D$ candidate. That is, $\theta^*$ is the angle between the $D$ direction in the lab and the direction of the chosen daughter in the rest frame of the $D$. We expect that the distribution of $|cos(\theta^*)|$ for the signal is flat, and that for the background is peaked near one with the peak populated by random low momentum tracks which happen to be moving along (or against) the direction of the $D$ candidate's boost. This is indeed what we find. Demanding that $|cos(\theta^*)| < 0.8$ significantly reduces this background.

Recall that CLEO/CESR spends approximately two-thirds of its time running on the $\Upsilon(4S)$ resonance, which can decay to a pair of $B\overline{B}$ mesons. Though the $\Upsilon(4S)$ is just above threshold for $B\overline{B}$ production, the resulting $B$ mesons are not produced at rest, and on average fly about 30 microns before decaying. While 30 microns is quite a short distance, it is not completely negligible on the scale of the flight distance error on a reconstructed $D^0$. As a determination of the $D^0$ candidate lifetime requires precise knowledge of both the $D^0$ production and decay vertices, we therefore wish to exclude $D^0$s originating from a $B$ meson decay. At CLEO, $D^0$s originating from $B$ meson decay (directly or indirectly) have a strikingly different momentum distribution than $D^0$s produced by other means. This provides us with a powerful means to discriminate against $D^0$ candidates from $B$ mesons (see Figure 3.2); we require that the momentum of the $D^0$ candidate be greater than 2.3 $GeV/c$. This criteria removes $D^0$ candidates with poorest proper time resolution, so the significant loss of efficiency does not significantly affect the resolution on the fitted lifetimes.

Finally, we demand that for each $D^0$ candidate hypothesis ($\pi^+\pi^-$, $K^+\pi^-$, $K^-\pi^+$, and $K^-K^+$), we demand the invariant mass of all the other hypotheses is more than 4 $\sigma$ inconsistent with the nominal $D$ mass. This primarily keeps symmetric $K\pi$ decays out of our sample (i.e., $K^+\pi^-$ and $K^-\pi^+$ candidates formed with the same two tracks), where the assignment of tracking hypothesis kinematically is not obvious. It also keeps all our samples independent; that is, no pair of $D$ decay hypotheses uses the same distinct tracks.

## 3.5 Proper Time Measurement

The proper time elapsed between the production and decay of a neutral particle is given by

$$t = \frac{m}{c}\frac{(\vec{r}_{dec} - \vec{r}_{prod}) \cdot \hat{p}}{|\vec{p}|} \tag{3.2}$$

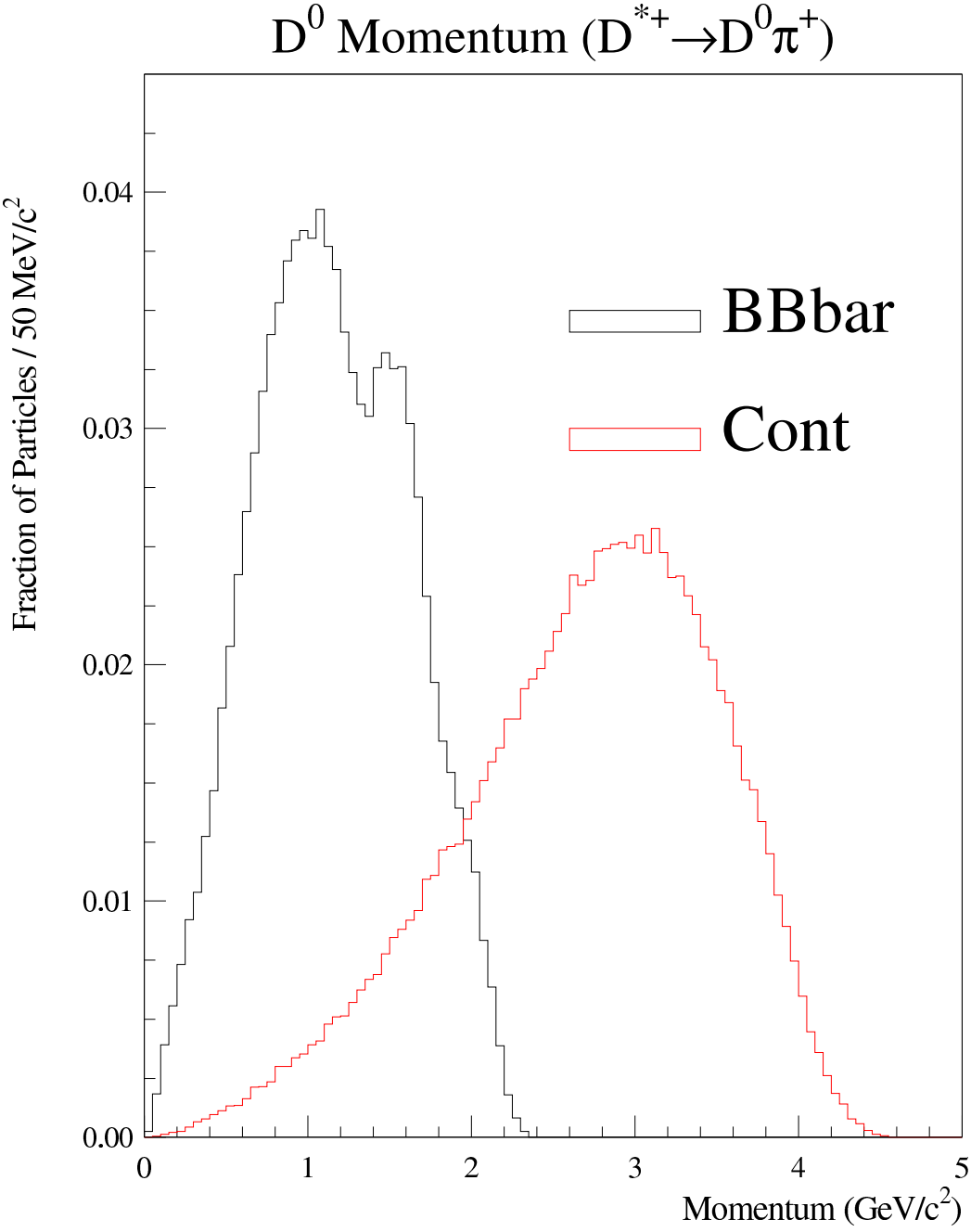


Figure 3.2: Neutral $D$ meson momentum spectrum from CLEO II.V monte carlo for $D$ mesons originating from $B$ meson events, and for $D$ mesons originating from *udsc* events (continuum).

where $m$ is the particle's mass, $\vec{r}_{dec}$ is it's decay vertex position, $\vec{r}_{prod}$ is it's production point, and $\vec{p}$ is it's momentum vector. We have $m$, $\vec{r}_{dec}$, and $\vec{p}$ from our $D$ meson reconstruction. What is left to estimate is the production vertex, $\vec{r}_{prod}$.

The beam position is an obvious candidate for $\vec{r}_{prod}$, as is the result of some primary vertex finding algorithm, perhaps using the beam position and size as a constraint. We elect not to use a primary vertex finding algorithm due to the introduction of bias in the $D$ decay length created when a track not belonging to the primary vertex is used to calculate it. If we build a primary vertex which contains any of the daughter tracks of a charmed meson on the "other side" of the event, the calculation of the vertex would be pulled away from its true value. The resulting bias is systematic, consistently farther away from the $D$ meson decay vertex than the truth, and leads to corresponding systematic biases in measured proper time. It is difficult in practice to avoid this kind of mistake, due to the small distances travelled by $D$ mesons and our finite detector resolution. The beam position, on the other hand, is an unbiased (if not optimal) estimator of an event's origin. Further, the beam position gives excellent resolution on the $y$ coordinate of $\vec{r}_{prod}$ ($\approx 10$ $\mu$m) due to its very small size in that dimension, and the beam position is uncorrelated with our $D$ meson candidate. So we elect to use the beam position as our estimator of $\vec{r}_{prod}$.

Rather than bend the reconstructed $D$ meson trajectory through $\vec{r}_{prod}$, we instead follow the $D$ meson trajectory to each of the coordinates of $\vec{r}_{prod}$ separately. We then have three measurements of the proper time:

$$\begin{aligned} t_x &= \frac{m}{c}\frac{(x_{dec} - x_{prod})}{p_x} \\ t_y &= \frac{m}{c}\frac{(y_{dec} - y_{prod})}{p_y} \\ t_z &= \frac{m}{c}\frac{(z_{dec} - z_{prod})}{p_z} \end{aligned} \tag{3.3}$$

and their associated errors:

$$\begin{aligned}
\sigma_{t_x}^2 = {t_x}^2 \Bigg\{ & \left(\frac{\sigma_m^2}{m^2}\right) + \left(\frac{\sigma_{p_x}^2}{{p_x}^2}\right) + \left(\frac{\sigma_{x_{dec}}^2+\sigma_{x_{prod}}^2}{(x_{dec}-x_{prod})^2}\right) \\
& + 2\Bigg[\left(\frac{-\sigma_{mp_x}}{mp_x}\right) + \left(\frac{\sigma_{mx_{dec}}}{m(x_{dec}-x_{prod})}\right) + \left(\frac{-\sigma_{x_{dec}p_x}}{(x_{dec}-x_{prod})}\right)\Bigg]\Bigg\} \\
\sigma_{t_y}^2 = {t_y}^2 \Bigg\{ & \left(\frac{\sigma_m^2}{m^2}\right) + \left(\frac{\sigma_{p_y}^2}{{p_y}^2}\right) + \left(\frac{\sigma_{y_{dec}}^2+\sigma_{y_{prod}}^2}{(y_{dec}-y_{prod})^2}\right) \\
& + 2\Bigg[\left(\frac{-\sigma_{mp_y}}{mp_y}\right) + \left(\frac{\sigma_{my_{dec}}}{m(y_{dec}-y_{prod})}\right) + \left(\frac{-\sigma_{y_{dec}p_y}}{(y_{dec}-y_{prod})}\right)\Bigg]\Bigg\} \\
\sigma_{t_z}^2 = {t_z}^2 \Bigg\{ & \left(\frac{\sigma_m^2}{m^2}\right) + \left(\frac{\sigma_{p_z}^2}{{p_z}^2}\right) + \left(\frac{\sigma_{z_{dec}}^2+\sigma_{z_{prod}}^2}{(z_{dec}-z_{prod})^2}\right) \\
& + 2\Bigg[\left(\frac{-\sigma_{mp_z}}{mp_z}\right) + \left(\frac{\sigma_{mz_{dec}}}{m(z_{dec}-z_{prod})}\right) + \left(\frac{-\sigma_{z_{dec}p_z}}{(z_{dec}-z_{prod})}\right)\Bigg]\Bigg\}
\end{aligned} \tag{3.4}$$

where we have used the fact that $\vec{r}_{prod}$ is uncorrelated with our $D$ meson candidate.

These three correlated proper time measurements can be combined into a single optimal estimator of the $D$ meson candidate's proper time and uncertainty [23]

$$\begin{aligned}
\bar{t} &= \sum_i w_i t_i \\
\sigma_{\bar{t}}^2 &= \sum_{ij} w_i w_j (V_t)_{ij}
\end{aligned} \tag{3.5}$$

where the indices $i$ and $j$ run over the coordinates, and

$$\begin{aligned}
w_i &= \frac{\sum_k (V_t^{-1})_{ik}}{\sum_{jk} (V_t^{-1})_{jk}} \\
(V_t)_{ij} &= \langle \delta t_i \delta t_j \rangle
\end{aligned} \tag{3.6}$$

are the weights and covariance matrix elements, and

$$\delta t_i = t_i \left( \frac{\delta m}{m} - \frac{\delta p_i}{p_i} + \frac{\delta x_{dec_i} - \delta x_{prod_i}}{(x_{dec_i} - x_{prod_i})} \right) \tag{3.7}$$

In this analysis, we use $\overline{t}$ and $\sigma_{\overline{t}}$ as our proper time and proper time uncertainty, respectively. Note that because of our choice of $\vec{r}_{prod}$, the contribution to $\overline{t}$ from the $z$ coordinate is negligible due to the large size of the beam in this coordinate ($\approx 3$ cm; this would not be true if we had better knowledge of $z_{prod}$); we include it anyway.

### 3.6 Lifetime Measurement

We extract the lifetime of our $D$ meson signals with an unbinned maximum likelihood fit. The inputs to the fit are the measured proper time, $t_i$, and proper time uncertainty, $\sigma_{t,i}$, and the reconstructed invariant mass, $m_i$. The mass is converted to a signal probability, $p_{\mathrm{Sig}_i}$, which is determined by a one dimensional binned fit to the full invariant mass distribution of the input sample.

In the proper time fit, the full likelihood function which is maximized has the following form:

$$\mathcal{L} = \mathcal{L}_{\mathrm{Sig}} + \mathcal{L}_{\mathrm{BG}}$$

That is, the total likelihood is the sum of two separable pieces, one for signal and one for background. Similarly, the background is divided into two components:

$$\mathcal{L}_{BG} = \mathcal{L}_{\mathrm{BG}_0} + \mathcal{L}_{\mathrm{BG}_\tau}$$

one component with lifetime and one without. Generally speaking, the components of the likelihood containing lifetime, $\mathcal{L}_{\mathrm{Sig}}$ and $\mathcal{L}_{\mathrm{BG}_\tau}$, are modelled as exponentials convoluted by a resolution function. The zero lifetime background piece, $\mathcal{L}_{\mathrm{BG}_0}$, is a delta function smeared by a resolution function.

The signal likelihood resolution function is the sum of three gaussians. The first gaussian is one whose width is the measured proper time error, $\sigma_{t,i}$, times some scale factor, $S_{\mathrm{Sig}}$ ; the $S_{\mathrm{Sig}}$ is meant to account for a possible uniform "mistake" in the

covariance matrix elements of the $D$ meson (and its daughters), as would be the case if there was an imperfect description of the detectors material used during track fitting. For the other two gaussians, the measured proper time errors are simply ignored and the widths, $\sigma_{\mathrm{Sig}_1}$ and $\sigma_{\mathrm{Sig}_2}$, and their normalizations, $f_{\mathrm{Sig}_1}$ and $f_{\mathrm{Sig}_2}$, can be fit for directly. In practice, $\sigma_{\mathrm{Sig}_2}$ is fixed to "something large"; we typically use 8 $ps$. This helps convergence. The purpose of these two gaussians is to model the proper time smearing when $\sigma_{t,i}$ does not represent the spread of the proper time distribution, as would be the case for hard multiple scattering or tracking system pattern recognition error of one or more of the $D$ meson daughters (we refer to these components as "mis-measured"). The sum of these three components to the likelihood is normalized by the total signal probability, $p_{\mathrm{Sig_i}}$, as determined by the fit to the invariant mass distribution. We further note that if we understand our detector well, we expect to find that the scale factor used in the first gaussian is close to 1 and the fraction of the signal in the other gaussians is near zero.

The treatment of the background is similar to that of the signal. The total background likelihood is normalized by the background probability, which is just $(1 - p_{\mathrm{Sig_i}})$. The likelihood considers two types of background: background with some lifetime $\tau_{\mathrm{BG}}$, and background with zero lifetime. We constrain both kinds of background to have the same resolution function. The model for the resolution function is the same as for the signal (three gaussians). The first gaussian, whose width is $\sigma_{t,i}$ times some scale factor, $S_{\mathrm{BG}}$, models the "correctly reconstructed" background, and the other two whose width and norms we fit for describe the "misreconstructed" background. In some sense, most background is "misreconstructed" - it is, after all, background. We will assign a systematic uncertainty due to our background model later.

There are a lot of fit parameters here; $\tau_{\mathrm{Sig}}$ is obviously the most important. It should also be noted that in one should not read too much into the meaning of the

parameter $\tau_{\rm BG}$, as the component of the background it describes generally contains more than one lifetime. The full likelihood function is:

$$\mathcal{L}\left(\tau_{\rm Sig}, S_{\rm Sig}, \sigma_{\rm Sig_1}, f_{\rm Sig_1}, \sigma_{\rm Sig_2}, f_{\rm Sig_2}, \tau_{\rm BG}, f_{\tau_{BG}}, S_{\rm BG}, \sigma_{\rm BG_1}, f_{\rm BG_1}, \sigma_{\rm BG_2}, f_{\rm BG_2}\right) =$$
$$\prod_i \int_0^\infty \Bigg[ \underbrace{p_{\rm Sig,i} E(t'|\tau_{\rm Sig})}_{\text{signal}} \Bigg( \underbrace{(1 - f_{\rm Sig_1} - f_{\rm Sig_2}) G(t_i - t'|S_{\rm Sig}\sigma_{t,i})}_{\text{proper time resolution}} +$$
$$\underbrace{f_{\rm Sig_1} G(t_i - t'|\sigma_{\rm Sig_1}) + f_{\rm Sig_2} G(t_i - t'|\sigma_{\rm Sig_2})}_{\text{mis-measured}} \Bigg) +$$
$$\Bigg( \underbrace{(1 - p_{\rm Sig,i})}_{\text{background}} \Bigg( \underbrace{f_{\tau_{\rm BG}} E(t'|\tau_{\rm BG})}_{\text{with lifetime}} + \underbrace{(1 - f_{\tau_{BG}})\delta(t')}_{\text{0 lifetime}} \Bigg) \times$$
$$\Bigg( \underbrace{(1 - f_{\rm BG_1} - f_{\rm BG_2}) G(t_i - t'|S_{\rm BG}\sigma_{t,i})}_{\text{proper time resolution}} +$$
$$\underbrace{f_{\rm BG_1} G(t_i - t'|\sigma_{\rm BG_1}) + f_{\rm BG_2} G(t_i - t'|\sigma_{\rm BG_2})}_{\text{mis-measured}} \Bigg) \Bigg) \Bigg] dt'$$

where $G(t|\sigma) \equiv 1/(\sqrt{2\pi}\sigma)\exp(-t^2/2\sigma^2)$ and $E(t|\tau) \equiv 1/\tau \exp(-t/\tau)$. The meanings for the fit parameters and inputs from the data are described in Table 3.1.

The lifetime extraction procedure described here is implemented in a software package called LifeFit [24].

We note for the record that the parameterization of the likelihood function is different from and more general than used in the published CLEO II.V measurement of the $K\pi$ lifetime [25]. The difference is that in the $K\pi$ lifetime analysis, the signal and the background were constrained to have the same resolution function; this allows the background to pull directly on the fitted signal lifetime. Indeed, we are unable to extract unbiased lifetimes from simulated $K\pi$ samples in the presence of background without allowing the background to have its own resolution parameters.

Table 3.1: Description of inputs from the data and lifetime fit parameters.

| Input Data | Description |
|---|---|
| $t_i$ | Proper Time |
| $\sigma_{t,i}$ | Proper Time uncertainty |
| $p_{\mathrm{Sig,i}}$ | Signal Probability (determined from mass fit) |
| **Fit Parameter** | **Description** |
| $\tau_{\mathrm{Sig}}$ | Signal Lifetime |
| $S_{\mathrm{Sig}}$ | Scale factor for proper time uncertainties (signal) |
| $\sigma_{\mathrm{Sig_1}}$ | proper time uncertainty for mis-measured signal |
| $f_{\mathrm{Sig_1}}$ | fraction of mis-measured signal with proper time uncertainty $\sigma_{\mathrm{Sig_1}}$ |
| $\sigma_{\mathrm{Sig_2}}$ | proper time uncertainty for mis-measured signal |
| $f_{\mathrm{Sig_2}}$ | fraction of mis-measured signal with proper time uncertainty $\sigma_{\mathrm{Sig_2}}$ |
| $\tau_{\mathrm{BG}}$ | Background Lifetime |
| $f_{\tau_{BG}}$ | Fraction of background with lifetime |
| $S_{\mathrm{BG}}$ | Scale factor for proper time uncertainties (background) |
| $\sigma_{\mathrm{BG_1}}$ | proper time uncertainty for mis-measured background |
| $f_{\mathrm{BG_1}}$ | fraction of mis-measured background with proper time uncertainty $\sigma_{\mathrm{BG_1}}$ |
| $\sigma_{\mathrm{BG_2}}$ | proper time uncertainty for mis-measured background |
| $f_{\mathrm{BG_2}}$ | fraction of mis-measured background with proper time uncertainty $\sigma_{\mathrm{BG_2}}$ |

# CHAPTER 4
# RESULTS

In this chapter, we describe the present the results of $y_{KK}$ and $y_{\pi\pi}$ measurements in simulated and real data. We show that based upon our simulation experiments, we have great confidence in our ability to extract an unbiased result from the data.

## 4.1 Simulation

Three simulation tools are employed to test all aspects of the analysis. We document the results of these tests here, in order of increasing complexity.

### 4.1.1 LifeFit Internal Generator

In order to test LifeFit independently of the rest of the analysis chain, LifeFit contains its own methods to generate simulated data. The simulation is generated according to the parameters that are fit for. Other fitter inputs such as $\sigma_{t,i}$ and $m_i$ are thrown according to distribution which mock up what we see in the data. This allows us to answer the question "does LifeFit work?" If so, LifeFit should be able to recover the input parameters within statistical errors, and those errors should be correct. The way we test this is to run thousands of simulation samples and fits with statistics similar to those found in the data, and with inputs that look similar to the data.

What we find is that LifeFit is able to recover the input values of the toy simulation. Figure 4.1 shows the pull distribution for the all important $\tau_{\text{Sig}}$ fit parameter for one such run of simulation. If we understand the unbinned fit, we should see that Figure 4.1 has a width consistent with one and a mean consistent with zero. This is indeed what we see.

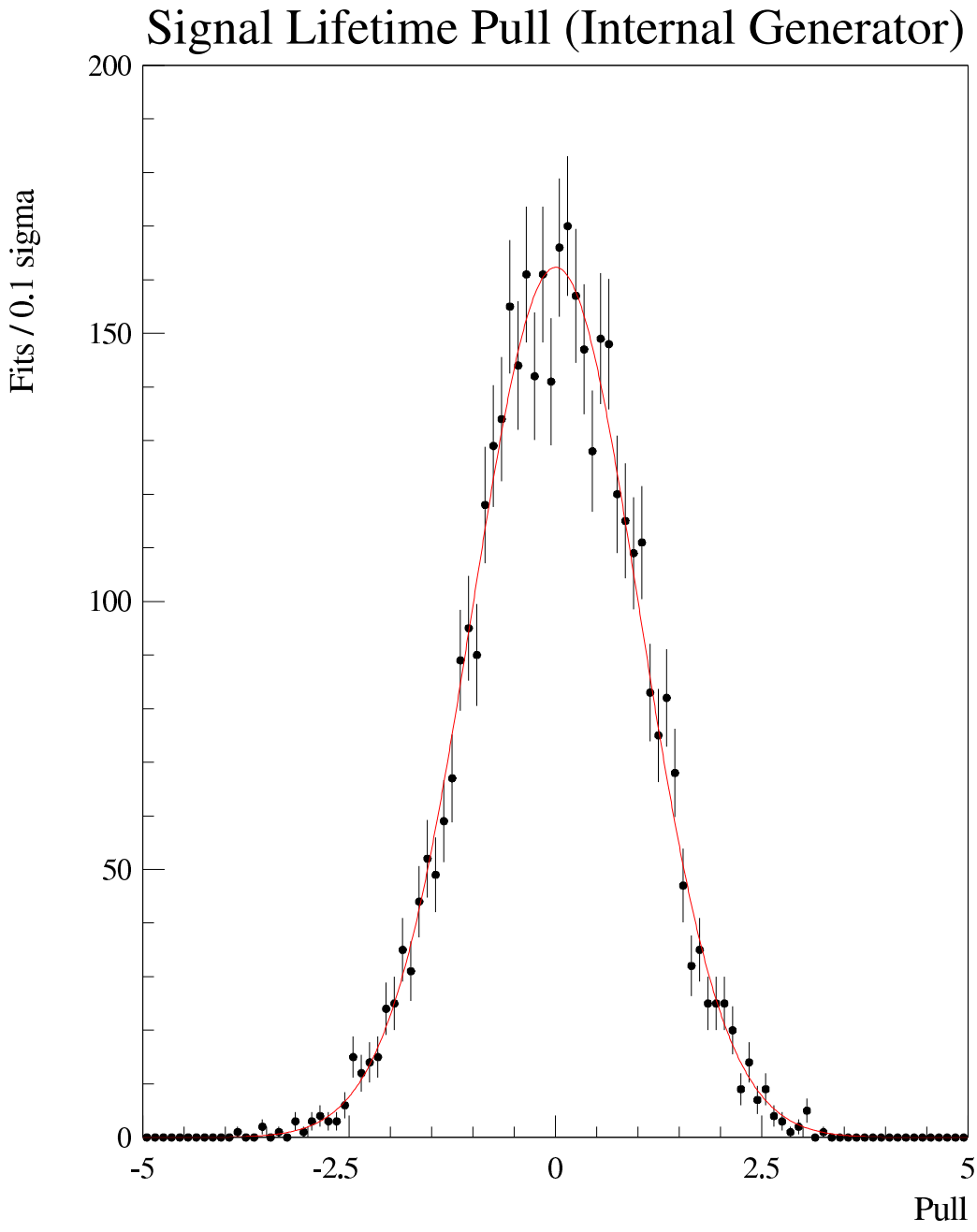


Figure 4.1: Fitted $\tau_{\text{Sig}}$ Pull distribution from many samples of mock data internally generated by LifeFit, and a single gaussian fit overlaid. The mean of the fit is $0.007 \pm 0.016$, and the $\sigma$ is $1.011 \pm 0.011$.

### 4.1.2 FASTMC

FASTMC is a derivative of MCFAST[26]. FASTMC is designed to be a tool to understand charged particle tracking performance. It allows the generation of single particles and their decay via QQ. It also traces the daughter trajectories through a detector described in an ASCII file, includes gaussian multiple scattering in the tracing process, creates and smears hits left in the detector, and provides a full Kalman fit to create reconstructed track candidates.

In this analysis, we use FASTMC as an independent infrastructure to test the entire analysis chain, including $D$ reconstruction code, in an idealized environment. This is done by embedding the actual analysis code, along with the necessary filling of CLEO analysis data structures, inside the FASTMC executable. Since the unbinned lifetime fitter was already independently tested in 4.1.1, we can use FASTMC as a direct test of the analysis code. It should be noted that the detector description used was certainly less than perfect, but that isn't important here; we are simply testing the math in our analysis code. If the analysis works, we should also find that a fit to the proper time distribution using our unbinned procedure and only including the signal lifetime and scale factor (as the simulation dictates) should result in a $\tau_{\rm Sig}$ consistent with the input value, and a $S_{\rm Sig}$ consistent with one.

Using a large sample of $\approx$ 1.2 million $K\pi$ signals generated with an input lifetime of 414.95 fs (same as in QQ's decay.dec) inside FASTMC, we recover a $\tau_{\rm Sig}$ of $414.96 \pm 0.60$ fs. We also find that the proper time uncertainties are computed correctly ($S_{\rm Sig}$ of $1.0039 \pm 0.0009$). This implies that the math in FASTMC and the analysis code is very close to perfectly correct, and that any imperfections negligible.

### 4.1.3 CLEOG

Armed with the understanding gained from the Lifefit and FASTMC simulations, we use large samples of generic GEANT [22]-based CLEOG [27] monte carlo to study the combined effects of a full detector simulation, backgrounds, and exposure

Table 4.1: Fit results to invariant mass distributions from CLEO II.V monte carlo for $KK$, $\pi\pi$, and $K\pi$. $K\pi$ was fit to two gaussians with the same mean and a polynomial of order 1, while $KK$ and $\pi\pi$ were fit to a single gaussian and polynomial of order 1.

| Parameter | $KK$ | $\pi\pi$ | $K\pi$ |
|---|---|---|---|
| Area | 20294±177 | 7668±98 | 121482±381 |
| $m_D(MeV)$ | 1864.33±0.05 | 1864.50±0.09 | 1864.45±0.02 |
| $\sigma_1(MeV)$ | 5.26±0.05 | 6.96±0.08 | 5.43±0.05 |
| $A_2/(A_1+A_2)$ | n/a | n/a | 0.26±0.02 |
| $\sigma_2/\sigma_1$ | n/a | n/a | 1.87±0.03 |
| $\chi^2$/DOF | 175/75 | 99/75 | 75/73 |

to CLEO software on the measured lifetimes of our neutral $D$ mesons. CLEOG is the CLEO simulation program which implements GEANT-based physics and full detector response simulations - it is our best simulation technology. By the term "generic" monte carlo, we mean that the monte carlo was generated without pre-selecting certain particle species from the truth table. It is the most general style of monte carlo, as it includes all known backgrounds.

The CLEOG simulated data used in this analysis is continuum ($e^+e^- \to udsc$) monte carlo, sampling the available CLEO II.V run range, and include backgrounds - this was achieved by embedding an selection function in CLEOG which mocked our analysis code and passed anything which could possibly end up in our analysis chain. The effective sizes of samples for $KK$ and $\pi\pi$ are over 8 times larger than the data, and for $K\pi$ is $\approx 6$ times larger than the data.

We would like to know if the inputs to the lifetime fitter and variables used in our selection criteria are well represented in the simulation. Plots of the lifetime fitter inputs, $m_D$, $t$, and $\sigma_t$ for the $KK$, $\pi\pi$, and $K\pi$ data and simulation are shown in Figures 4.2, 4.3, and 4.4. We observe that the distributions of proper time, $t$, and its uncertainty, $\sigma_t$, appear to be simulated quite well; however, $m_D$ is not. The results of fits to the $K\pi$, $KK$, and $\pi\pi$ invariant mass distributions are given in Table 4.1. The input mass is 1.8646 $GeV$. We note that none of the central values in Table 4.1

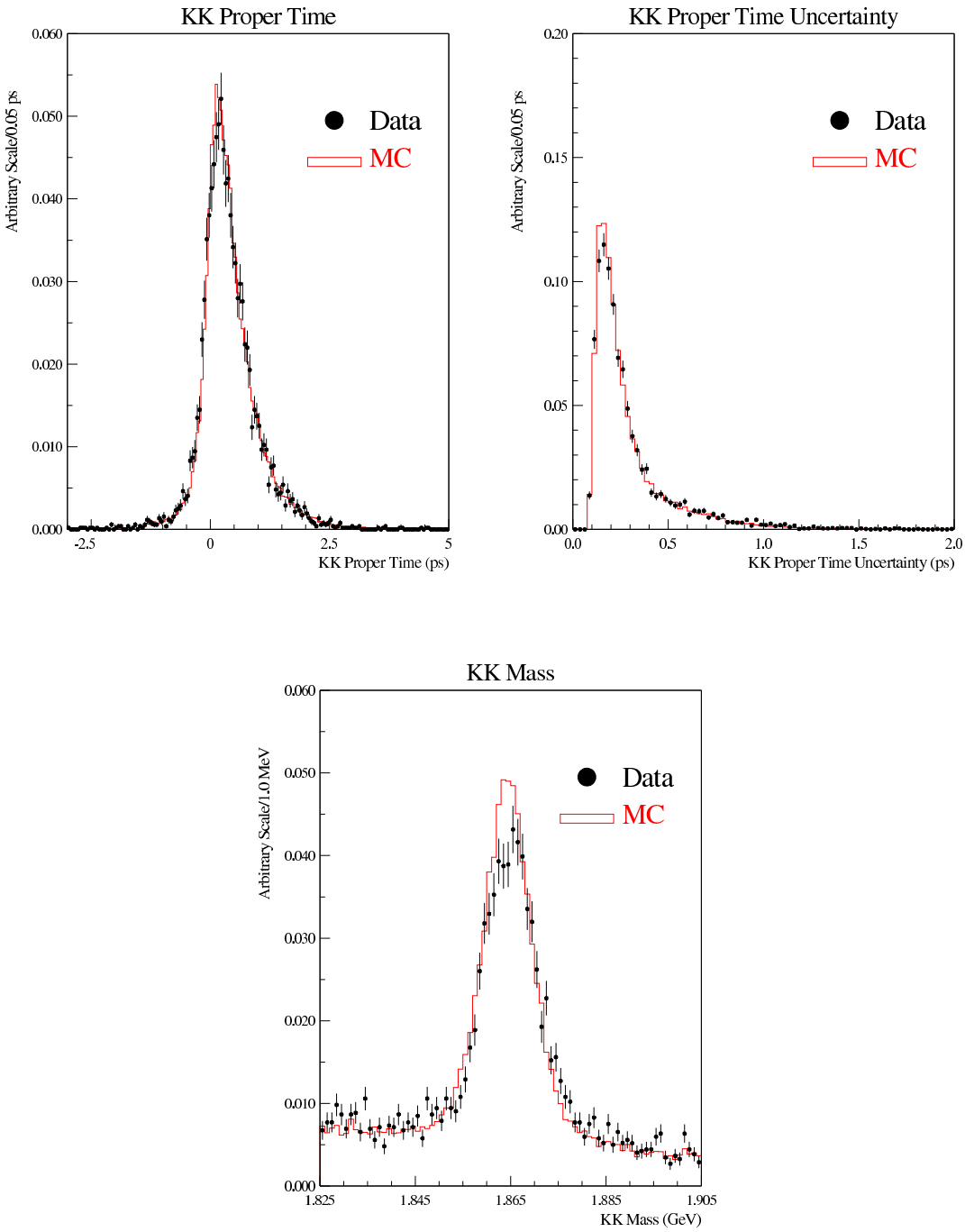


Figure 4.2: Comparison of $KK$ proper time, proper time uncertainty, and mass distributions in data and monte carlo. Data and monte carlo are both normalized to have the same area.

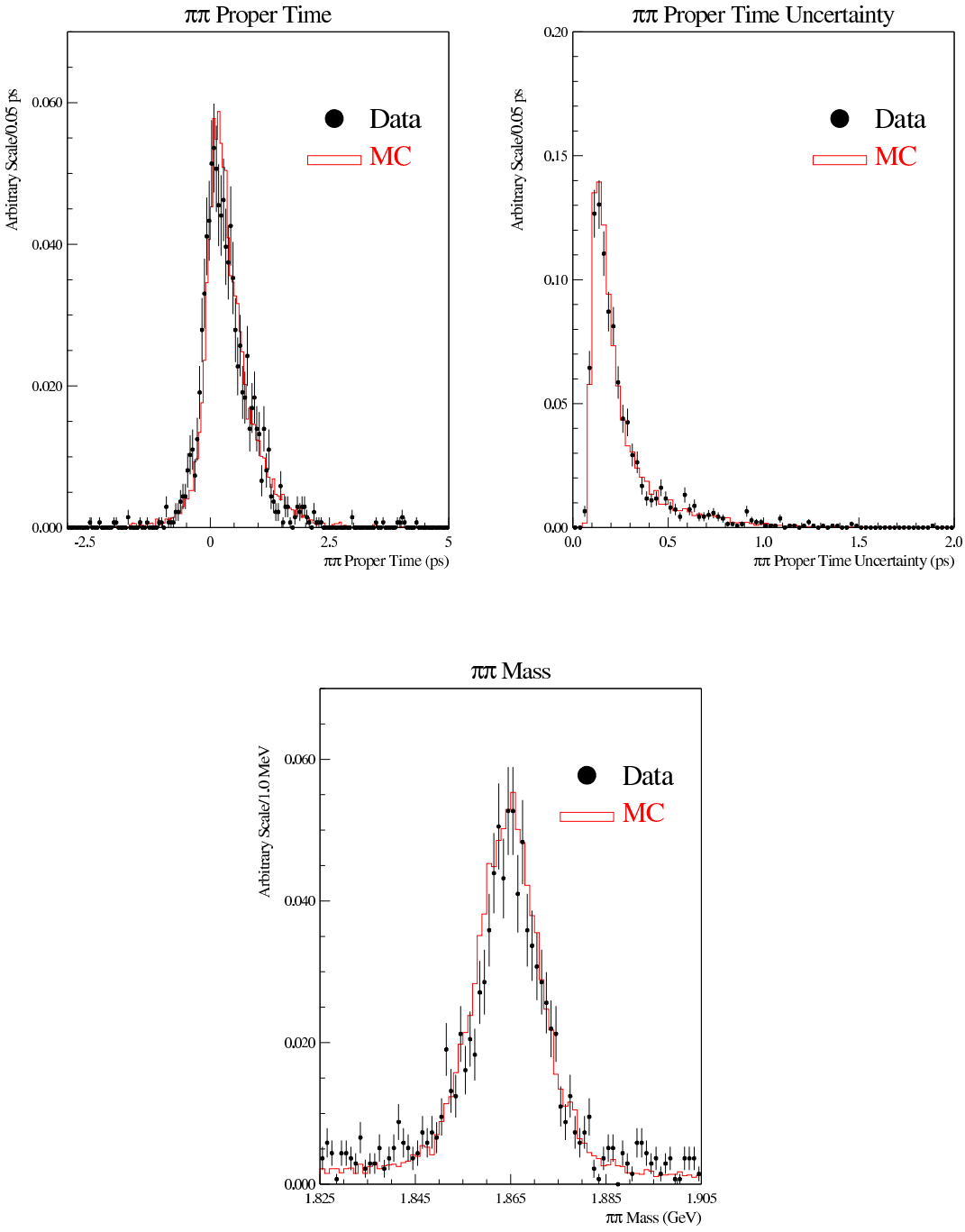


Figure 4.3: Comparison of $\pi\pi$ proper time, proper time uncertainty, and mass distributions in data and monte carlo. Data and monte carlo are both normalized to have the same area.

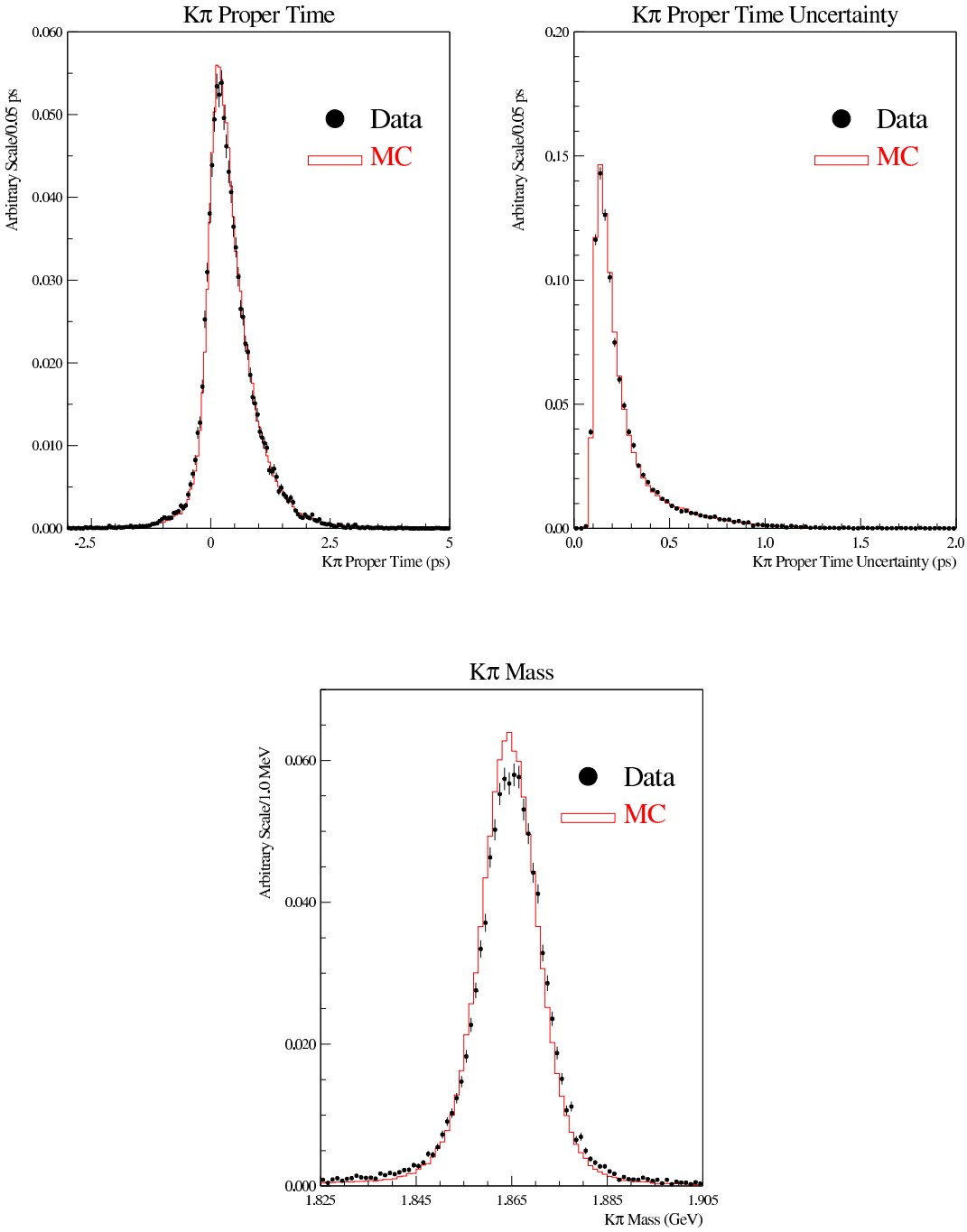


Figure 4.4: Comparison of $K\pi$ proper time, proper time uncertainty, and mass distributions in data and monte carlo. Data and monte carlo are both normalized to have the same area.

are consistent with the input at the $1\sigma$ level. We further note that the data (see Table 4.7) and monte carlo disagree about the central value of the mass for $K\pi$ and $KK$.

By using truth table information, we can identify a subsample of correctly reconstructed $D^0$ candidates. Using this sample, we note the linear reconstructed mass-proper time correlation. Figure 4.5 shows the proper time residual, reconstructed minus truth, versus the reconstructed mass for each decay channel. This figure tells us that we can bias our lifetime and $y$ measurements by reconstructing a mean $D$ mass that is not the truth. Of course, we can bias our lifetime similarly by getting the decay vertex wrong, or by misreconstructing the $D$ momentum. But the mass is special, in that we can do something about it; namely, we can constrain the reconstructed mass for each candidate to the same value. In the monte carlo, the value we should constrain to is obvious: the input $D$ mass (1.8646 GeV). Figure 4.5 shows how the mass constraint removes the potential lifetime bias due to the reconstructed mass-proper time correlation. Therefore, we use a proper time calculated with a mass constraint in all lifetime fits. Note that the mass constrained proper time will be used only in the signal portion of the likelihood function; it is incorrect to use such a proper time for a combination which is a background.

The input lifetime to the simulation is 415.0 fs. We look for biases in our reconstruction technique by looking at proper time residual and pull distributions for $K\pi$, $KK$, and $\pi\pi$ combinations which were identified from truth table information as being correct combinations. If no bias exists, we expect that the residuals and pulls should have means consistent with zero. Further, if our measured proper time errors are accurate, we should find the pull distributions should have a width consistent with one. We show the residual and pull distributions fitted to two gaussians with the same mean in Figures 4.6 and 4.7, respectively. The fit results are summarized in Table 4.2. We find no statistically significant biases.

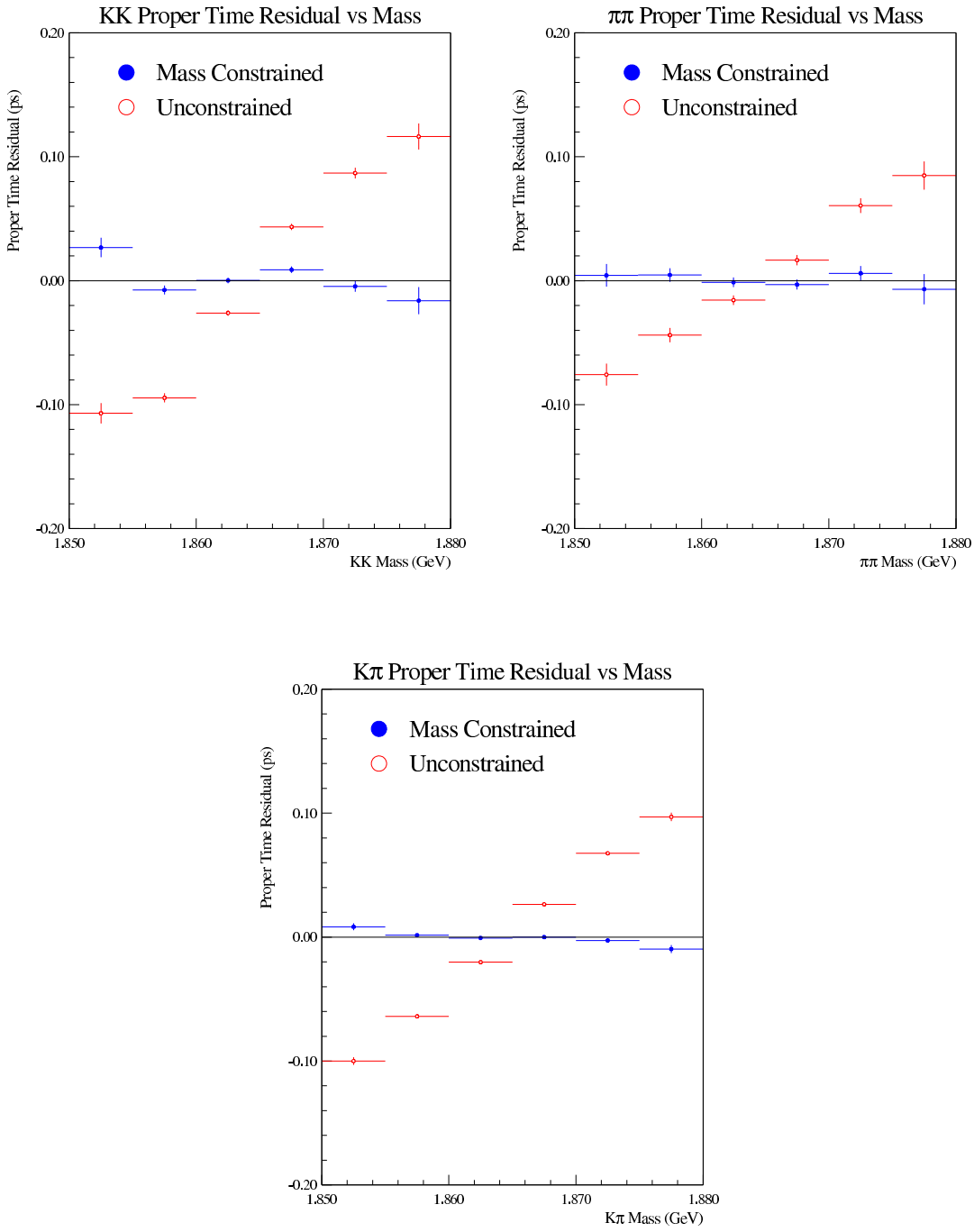


Figure 4.5: Comparison of mass constrained and unconstrained proper time residuals as a function of reconstructed mass for $KK$, $\pi\pi$, and $K\pi$ signal from CLEO II.V monte carlo.

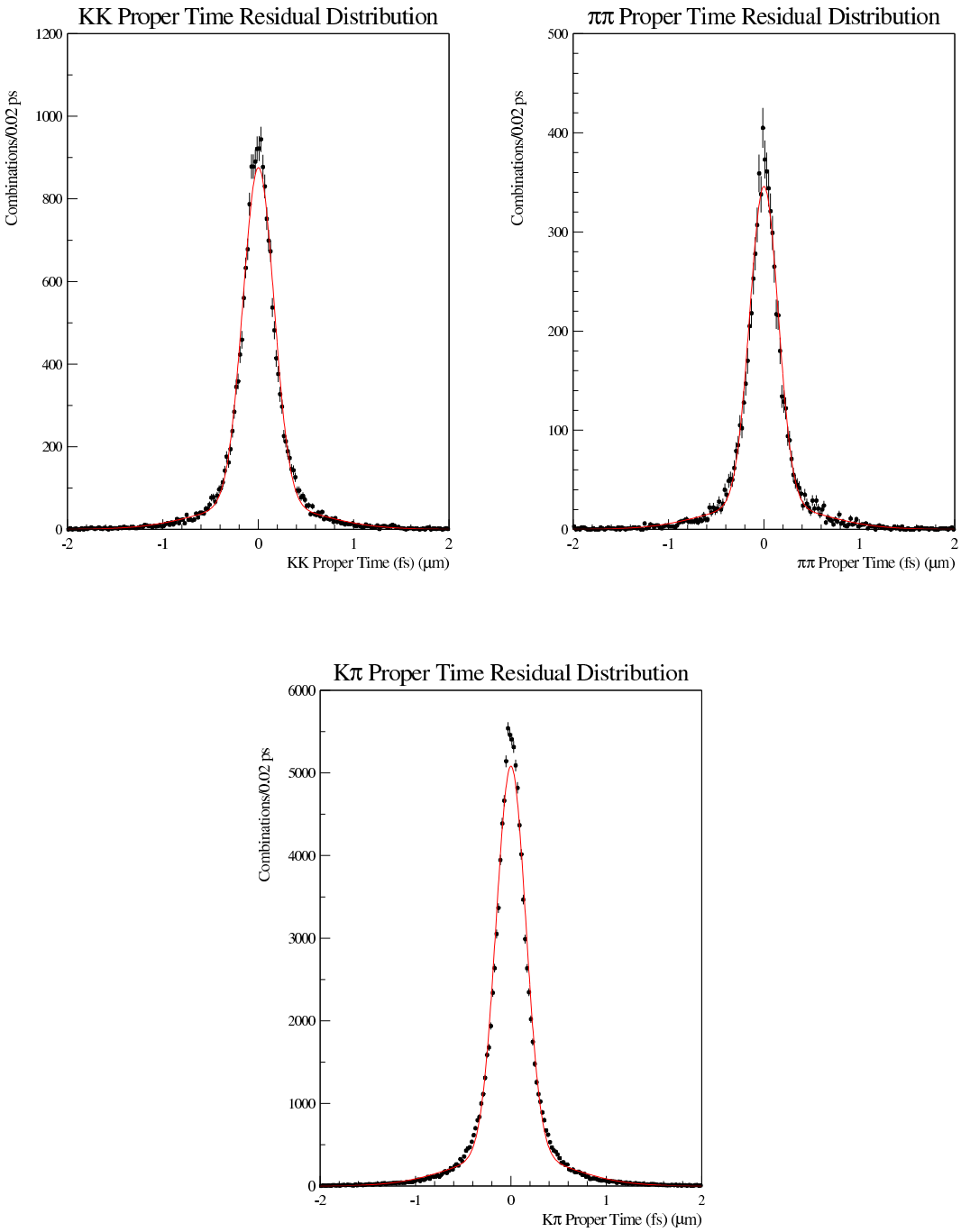


Figure 4.6: Proper time residuals from tagged $KK$, $\pi\pi$, and $K\pi$ CLEO II.V CLEOG monte carlo. A fit to two gaussians having the same mean is overlaid.

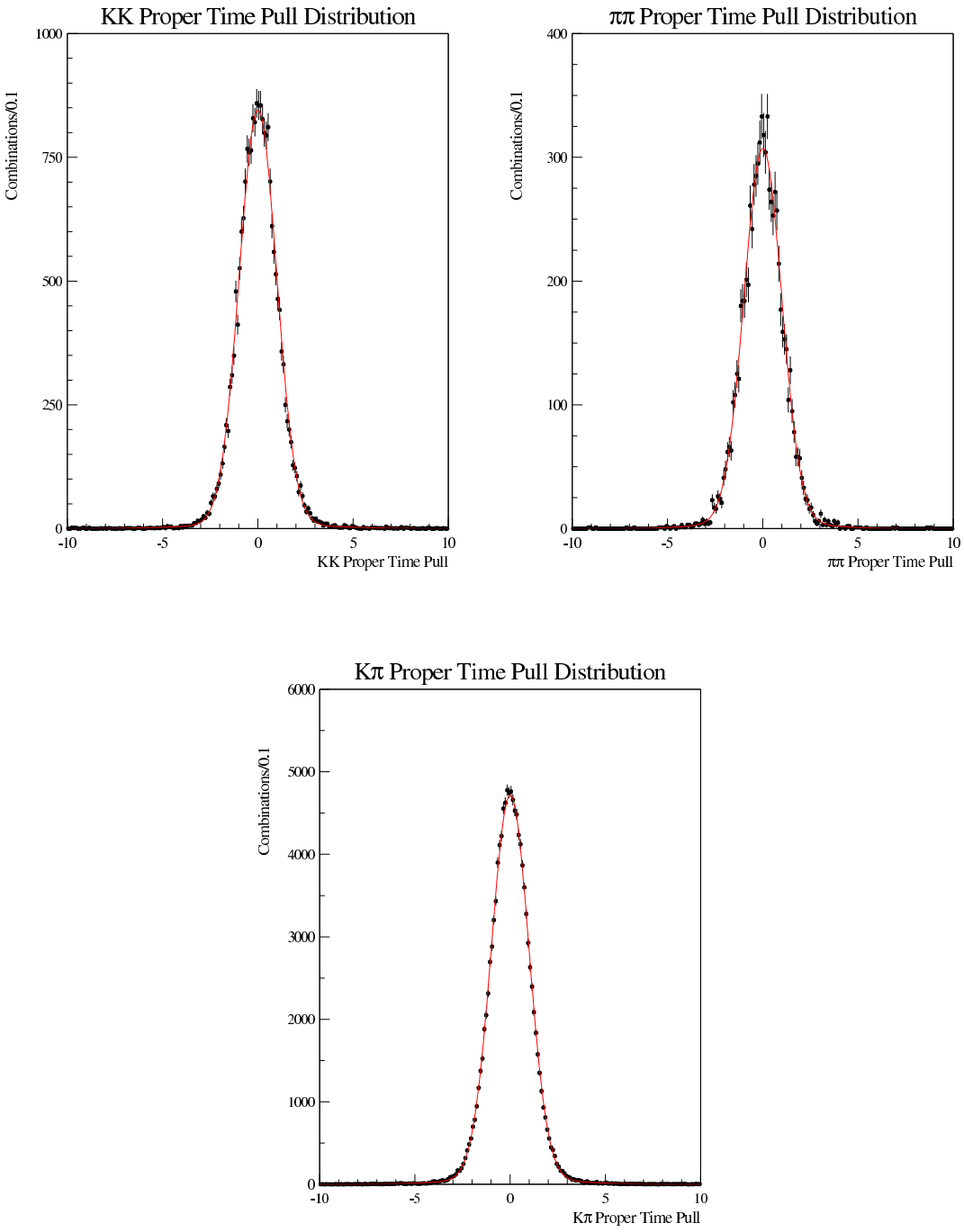


Figure 4.7: Proper time pulls from tagged $KK$, $\pi\pi$, and $K\pi$ CLEO II.V CLEOG monte carlo. A fit to two gaussians having the same mean is overlaid.

Table 4.2: Fit results to $KK$, $\pi\pi$, and $K\pi$ proper time residual and pull distributions for CLEO II.V tagged MC.

| Residuals | Mean(fs) | $\sigma_1$(fs) | $A_2/(A_1+A_2)$ | $\sigma_2/\sigma_1$ | $\sigma_{RMS}$(fs) | $\chi^2$/DOF |
|---|---|---|---|---|---|---|
| $KK$ | 2.3±1.3 | 162.3±1.7 | 0.218±0.007 | 3.74±0.05 | 317.5 | 423/195 |
| $\pi\pi$ | 0.6±2.2 | 148.4±2.5 | 0.236±0.010 | 3.95±0.09 | 313.0 | 300/195 |
| $K\pi$ | 0.3±0.5 | 154.6±0.7 | 0.233±0.003 | 3.81±0.02 | 314.4 | 1711/195 |
| Pulls | Mean | $\sigma_1$ | $A_2/(A_1+A_2)$ | $\sigma_2/\sigma_1$ | $\sigma_{RMS}$ | $\chi^2$/DOF |
| $KK$ | $(0.9\pm0.7)\cdot10^{-2}$ | 0.978±0.007 | $(3.5\pm0.4)\cdot10^{-2}$ | 3.48±0.16 | 1.15 | 268/195 |
| $\pi\pi$ | $(0.7\pm1.3)\cdot10^{-2}$ | 0.987±0.012 | $(4.7\pm0.9)\cdot10^{-2}$ | 2.71±0.17 | 1.12 | 184/195 |
| $K\pi$ | $(0.2\pm0.3)\cdot10^{-2}$ | 0.981±0.003 | $(3.9\pm0.2)\cdot10^{-2}$ | 3.14±0.06 | 1.14 | 410/195 |

Table 4.3: Fit results to $KK$, $\pi\pi$, and $K\pi$ proper time distributions in CLEO II.V monte carlo.

| Signal Param. | $KK$ | $\pi\pi$ | $K\pi$ |
|---|---|---|---|
| $\tau_{\rm Sig}$(ps) | 0.4144±0.0040 | 0.4149±0.0058 | 0.4160±0.0015 |
| $S_{\rm Sig}$ | 1.016 (fixed) | 1.016 (fixed) | 1.016±0.005 |
| $f_{\rm Sig_1}$ | 0.011 (fixed) | 0.011 (fixed) | 0.011±0.002 |
| $\sigma_{\rm Sig_1}$(ps) | 0.583 (fixed) | 0.583 (fixed) | 0.583±0.070 |
| $f_{\rm Sig_2}$ | 0.00057 (fixed) | 0.00057 (fixed) | 0.00057±0.00013 |
| $\sigma_{\rm Sig_2}$(ps) | 8.0 (fixed) | 8.0 (fixed) | 8.0 (fixed) |
| Background Param. | $KK$ | $\pi\pi$ | $K\pi$ |
| $\tau_{\rm BG}$(ps) | 0.462±0.008 | 0.466±0.067 | 0.379±0.017 |
| $f_{\tau_{BG}}$ | 0.871±0.011 | 0.373±0.047 | 0.894±0.028 |
| $S_{\rm BG}$ | 1.000±0.015 | 1.230±0.050 | 1.099±0.042 |
| $f_{\rm BG_1}$ | 0.029±0.003 | 0.041±0.013 | 0.155±0.018 |
| $\sigma_{\rm BG_1}$(ps) | 1.87±0.17 | 2.06±0.41 | 1.39±0.11 |
| $f_{\rm BG_2}$ | 0.005±0.001 | 0.008±0.004 | 0.014±0.003 |
| $\sigma_{\rm BG_2}$(ps) | 8.0 (fixed) | 8.0 (fixed) | 8.0 (fixed) |

Table 4.4: Correlation matrix from fit to $KK$ proper time distribution from CLEO II.V monte carlo.

| Par | Global | $\tau_{\rm Sig}$ | $\tau_{\rm BG}$ | $f_{\tau_{BG}}$ | $S_{\rm BG}$ | $f_{\rm BG_1}$ | $\sigma_{\rm BG_1}$ | $f_{\rm BG_2}$ |
|---|---|---|---|---|---|---|---|---|
| $\tau_{\rm Sig}$ | 0.31998 | 1.000 | -0.238 | -0.018 | -0.003 | -0.005 | 0.000 | 0.010 |
| $\tau_{\rm BG}$ | 0.67941 | -0.238 | 1.000 | -0.610 | -0.305 | -0.059 | 0.000 | -0.103 |
| $f_{\tau_{BG}}$ | 0.64233 | -0.018 | -0.610 | 1.000 | 0.296 | 0.060 | 0.000 | 0.046 |
| $S_{\rm BG}$ | 0.61424 | -0.003 | -0.305 | 0.296 | 1.000 | 0.524 | -0.006 | -0.103 |
| $f_{\rm BG_1}$ | 0.53683 | -0.005 | -0.059 | 0.060 | 0.524 | 1.000 | -0.006 | -0.055 |
| $\sigma_{\rm BG_1}$ | 0.00693 | 0.000 | 0.000 | 0.000 | -0.006 | -0.006 | 1.000 | 0.000 |
| $f_{\rm BG_2}$ | 0.17740 | 0.010 | -0.103 | 0.046 | -0.103 | -0.055 | 0.000 | 1.000 |

Table 4.5: Correlation matrix from fit to $\pi\pi$ proper time distribution from CLEO II.V monte carlo.

| Par | Global | $\tau_{\rm Sig}$ | $\tau_{\rm BG}$ | $f_{\tau_{BG}}$ | $S_{\rm BG}$ | $f_{\rm BG_1}$ | $\sigma_{\rm BG_1}$ | $f_{\rm BG_2}$ |
|---|---|---|---|---|---|---|---|---|
| $\tau_{\rm Sig}$ | 0.27185 | 1.000 | -0.174 | -0.019 | -0.007 | -0.004 | -0.029 | 0.011 |
| $\tau_{\rm BG}$ | 0.73545 | -0.174 | 1.000 | -0.651 | 0.050 | -0.357 | 0.031 | -0.007 |
| $f_{\tau_{BG}}$ | 0.68035 | -0.019 | -0.651 | 1.000 | -0.130 | 0.179 | 0.012 | -0.013 |
| $S_{\rm BG}$ | 0.37953 | -0.007 | 0.050 | -0.130 | 1.000 | -0.328 | 0.188 | -0.038 |
| $f_{\rm BG_1}$ | 0.62644 | -0.004 | -0.357 | 0.179 | -0.328 | 1.000 | -0.385 | -0.066 |
| $\sigma_{\rm BG_1}$ | 0.57715 | -0.029 | 0.031 | 0.012 | 0.188 | -0.385 | 1.000 | -0.380 |
| $f_{\rm BG_2}$ | 0.45624 | 0.011 | -0.007 | -0.013 | -0.038 | -0.066 | -0.380 | 1.000 |

Table 4.6: Correlation matrix from fit to $K\pi$ proper time distribution from CLEO II.V monte carlo.

| Par | Global | $\tau_{\rm Sig}$ | $S_{\rm Sig}$ | $f_{\rm Sig_1}$ | $\sigma_{\rm Sig_1}$ | $f_{\rm Sig_2}$ | $\tau_{\rm BG}$ | $f_{\tau_{BG}}$ | $S_{\rm BG}$ | $f_{\rm BG_1}$ | $\sigma_{\rm BG_1}$ | $f_{\rm BG_2}$ |
|---|---|---|---|---|---|---|---|---|---|---|---|---|
| $\tau_{\rm Sig}$ | 0.28981 | 1.000 | -0.125 | -0.013 | -0.090 | -0.032 | -0.156 | 0.014 | 0.005 | 0.085 | -0.106 | 0.058 |
| $S_{\rm Sig}$ | 0.44690 | -0.125 | 1.000 | -0.299 | 0.057 | -0.015 | -0.007 | 0.035 | -0.218 | 0.114 | -0.109 | 0.063 |
| $f_{\rm Sig_1}$ | 0.79035 | -0.013 | -0.299 | 1.000 | -0.674 | 0.021 | 0.021 | 0.015 | 0.051 | -0.133 | 0.203 | -0.115 |
| $\sigma_{\rm Sig_1}$ | 0.78431 | -0.090 | 0.057 | -0.674 | 1.000 | -0.071 | 0.131 | -0.074 | 0.094 | -0.270 | 0.113 | -0.014 |
| $f_{\rm Sig_2}$ | 0.44342 | -0.032 | -0.015 | 0.021 | -0.071 | 1.000 | 0.003 | 0.005 | 0.000 | 0.041 | -0.057 | -0.329 |
| $\tau_{\rm BG}$ | 0.76091 | -0.156 | -0.007 | 0.021 | 0.131 | 0.003 | 1.000 | -0.694 | -0.201 | -0.344 | 0.209 | -0.111 |
| $f_{\tau_{BG}}$ | 0.70980 | 0.014 | 0.035 | 0.015 | -0.074 | 0.005 | -0.694 | 1.000 | 0.235 | 0.175 | -0.084 | 0.043 |
| $S_{\rm BG}$ | 0.60041 | 0.005 | -0.218 | 0.051 | 0.094 | 0.000 | -0.201 | 0.235 | 1.000 | -0.423 | 0.337 | -0.172 |
| $f_{\rm BG_1}$ | 0.84651 | 0.085 | 0.114 | -0.133 | -0.270 | 0.041 | -0.344 | 0.175 | -0.423 | 1.000 | -0.750 | 0.303 |
| $\sigma_{\rm BG_1}$ | 0.83630 | -0.106 | -0.109 | 0.203 | 0.113 | -0.057 | 0.209 | -0.084 | 0.337 | -0.750 | 1.000 | -0.532 |
| $f_{\rm BG_2}$ | 0.66205 | 0.058 | 0.063 | -0.115 | -0.014 | -0.329 | -0.111 | 0.043 | -0.172 | 0.303 | -0.532 | 1.000 |

To make sure we can recover the input lifetime in the presence of background, we fit the reconstructed proper time distributions for each decay channel with the unbinned lifetime fitter. Noting that the three decay modes in question are very similar kinematically, we can use the signal resolution function determined from the high statistics $K\pi$ sample and apply it to the smaller $KK$ and $\pi\pi$ samples. As noted above, when evaluating the signal portion of the likelihood function, we use a proper time and uncertainty calculated with the neutral $D$ meson candidate mass constrained to 1.8646 $GeV$. The results of the fits are shown in Table 4.3, and the covariance matrices are given in Tables 4.4, 4.5, and 4.6. We find that the lifetime fitter performs very well, and no statistically significant biases are observed. From these results, we can extract measurement of $y_{CP}$ from the monte carlo - it should be consistent with zero, as the simulation has no knowledge of mixing in the $D$ system. We find

$$\begin{aligned} y_{KK_{MC}} &= 0.004 \pm 0.010 \\ y_{\pi\pi_{MC}} &= 0.003 \pm 0.014 \end{aligned} \tag{4.1}$$

We can also combine the monte carlo results to obtain

$$\overline{y}_{MC} = 0.003 \pm 0.009 \tag{4.2}$$

## 4.2 Data

The $K\pi$, $KK$, and $\pi\pi$ mass distributions for all candidates passing our selection requirements is shown in Figure 4.8. The results of fits to these mass distributions for the signal portion are given in Table 4.7. Note that the mean of the $KK$ and $\pi\pi$ fits are consistent with that of $K\pi$, implying that any problems with our mass scale due

Table 4.7: Fit results to invariant mass distributions from CLEO II.V data for $KK$, $\pi\pi$, and $K\pi$. $K\pi$ was fit to two gaussians with the same mean and a polynomial of order one, while $KK$ and $\pi\pi$ were fit to a single gaussian and polynomial of order one.

| Parameter | $KK$ | $\pi\pi$ | $K\pi$ |
|---|---|---|---|
| Area | 2548±66 | 965±37 | 21517±183 |
| $m_D(MeV)$ | 1865.09±0.15 | 1864.69±0.26 | 1864.98±0.05 |
| $\sigma_1(MeV)$ | 5.59±0.15 | 6.75±0.25 | 5.65±0.14 |
| $A_2/(A_1+A_2)$ | n/a | n/a | 0.27±0.04 |
| $\sigma_2/\sigma_1$ | n/a | n/a | 1.96±0.10 |
| $\chi^2$/DOF | 96/75 | 89/75 | 90/73 |

Table 4.8: Fit results to $\Delta M$ distributions from CLEO II.V data for $KK$, $\pi\pi$, and $K\pi$. $K\pi$ was fit to two gaussians with the same mean and a threshold function, while $KK$ and $\pi\pi$ were fit to a single gaussian and threshold function.

| Parameter | $KK$ | $\pi\pi$ | $K\pi$ |
|---|---|---|---|
| Area | 2525±70 | 918±36 | 21286±177 |
| $\Delta m(MeV)$ | 145.432±0.007 | 145.435±0.010 | 145.436±0.002 |
| $\sigma_1(keV)$ | 235.5±7.6 | 237.6±10.3 | 187.9±3.1 |
| $A_2/(A_1+A_2)$ | n/a | n/a | 0.31±0.01 |
| $\sigma_2/\sigma_1$ | n/a | n/a | 3.35±0.10 |
| $\chi^2$/DOF | 390/282 | 343/282 | 432/280 |

to tracking hypothesis ($K$ vs. $\pi$) are small at our level of statistics. For reference, the $\Delta m$ distributions are shown in Figure 4.9 and fit results given in Table 4.8.

The $K\pi$, $KK$, and $\pi\pi$ proper time distributions are shown in Figure 4.10. These distributions were fit in an unbinned likelihood fit with the likelihood function described in section 3.6. The fit was performed as in the CLEOG monte carlo (see Section 4.1.3); that is, a mass constrained proper time and uncertainty were used in the signal portion of the likelihood, and the $KK$ and $\pi\pi$ signal resolution parameters were fixed to those obtained from the $K\pi$ fit. The only difference between the treatment of the data and monte carlo is the mass to which the $D$ meson candidates were constrained.

In the simulation, the true mass is known absolutely ($m_D = 1.8646$ GeV). However, we are not so lucky in the data. According to reference [29], the mass of the

$D^0$ meson is $1864.5 \pm 0.5$ MeV; i.e., it is not very well known. So how do we decide what mass to constrain to in the data? We can preserve the spirit of the monte carlo analysis by replacing the true mass with our best estimate of the mass from our data. That is, we correct our data based upon the simulation, and take a weighted average of the $K\pi$, $KK$, and $\pi\pi$ corrected mean masses. The result we find for this weighted average is 1.86514 GeV. We note for now that constraining the $D$ meson candidate mass to this value is a source of possible systematic error due to the linear relationship between reconstructed mass and proper time (which have different slopes for $K\pi$, $KK$, and $\pi\pi$). The important issue, which the mass constraint addresses, is that $K\pi$, $KK$, and $\pi\pi$ proper times are all evaluated with the same mass.

The results of the proper time fits are shown in Table 4.9, and the correlation matrices resulting from these fits are shown in Tables 4.10, 4.11, and 4.12, for $KK$, $\pi\pi$, and $K\pi$, respectively. We find that the measured $K\pi$, $KK$, and $\pi\pi$ lifetimes are statistically consistent with one another, and that the resolution functions for the signal are very similar, as expected. We also find that the lifetime of the background close to the $D$ lifetime. From the correlation matrices, we can see that the scale factor for the signal proper time uncertainties and the lifetime of the background are among the most correlated with the signal lifetime, again not unexpected.

From Table 4.9, we can extract measurements of $y_{CP}$:

$$\begin{aligned} y_{KK} &= -0.015 \pm 0.029 \\ y_{\pi\pi} &= 0.008 \pm 0.043 \end{aligned} \tag{4.3}$$

Combining these results, using the same prescription used to combine the proper time measurements in section 3.5, we obtain

$$\overline{y} = -0.008 \pm 0.025 \tag{4.4}$$

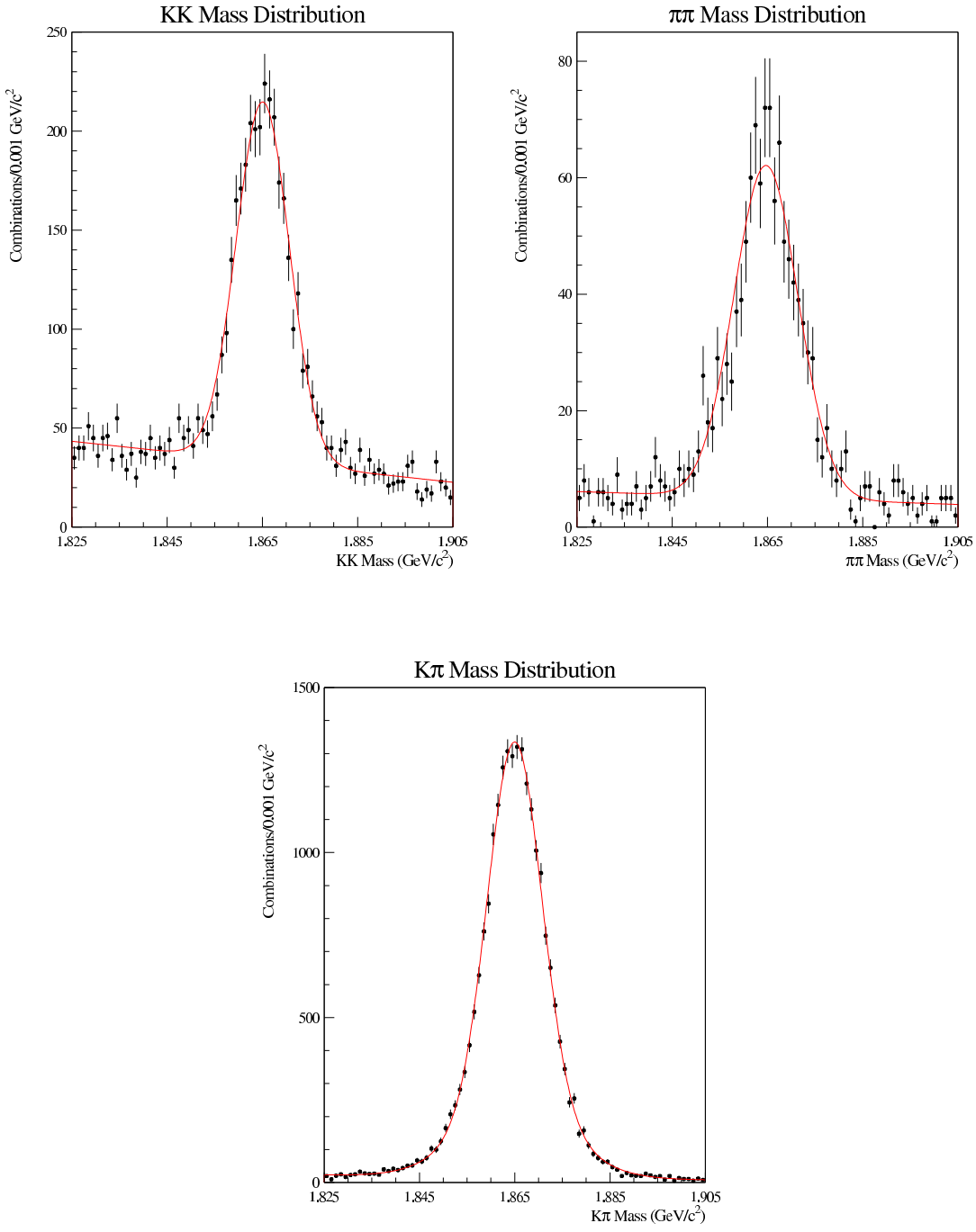


Figure 4.8: Invariant mass distributions from CLEO II.V data for $KK$, $\pi\pi$, and $K\pi$ with overlaid fit function (see Table 4.7 for fit results).

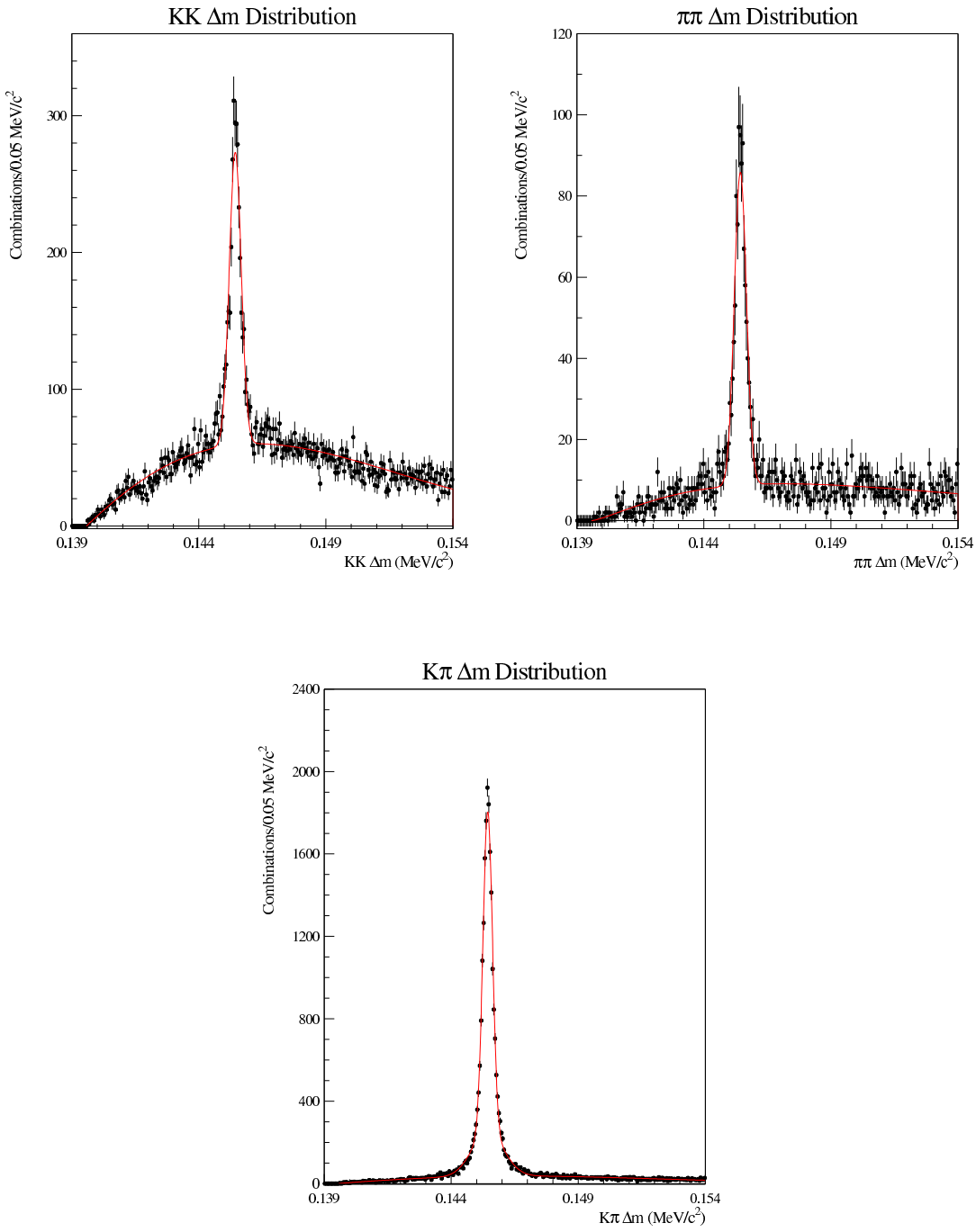


Figure 4.9: Mass difference distributions, $m_{D^*} - m_D$, from CLEO II.V data for $KK$, $\pi\pi$, and $K\pi$ with overlaid fit function (see Table 4.8 for fit results).

Table 4.9: Fit results to $KK$, $\pi\pi$, and $K\pi$ proper time distributions in CLEO II.V data.

| Signal Param. | $KK$ | $\pi\pi$ | $K\pi$ |
|---|---|---|---|
| $\tau_{\rm Sig}(ps)$ | 0.4106±0.0116 | 0.4013±0.0169 | 0.4046±0.0036 |
| $S_{\rm Sig}$ | 1.089 (fixed) | 1.089 (fixed) | 1.089±0.015 |
| $f_{\rm Sig_1}$ | 0.038 (fixed) | 0.038 (fixed) | 0.038±0.009 |
| $\sigma_{\rm Sig_1}(ps)$ | 0.590 (fixed) | 0.590 (fixed) | 0.590±0.079 |
| $f_{\rm Sig_2}$ | 0.00039 (fixed) | 0.00039 (fixed) | 0.00039±0.00028 |
| $\sigma_{\rm Sig_2}(ps)$ | 8.0 (fixed) | 8.0 (fixed) | 8.0 (fixed) |
| Background Param. | $KK$ | $\pi\pi$ | $K\pi$ |
| $\tau_{\rm BG}(ps)$ | 0.436±0.020 | 0.559±0.154 | 0.376±0.030 |
| $f_{\tau_{BG}}$ | 0.857±0.029 | 0.322±0.075 | 0.810±0.048 |
| $S_{\rm BG}$ | 1.037±0.041 | 1.361±0.231 | 1.171±0.075 |
| $f_{\rm BG_1}$ | 0.057±0.037 | 0.358±0.123 | 0.122±0.028 |
| $\sigma_{\rm BG_1}(ps)$ | 0.74±0.37 | 0.28±0.06 | 1.34±0.16 |
| $f_{\rm BG_2}$ | 0.012±0.003 | 0.042±0.013 | 0.012±0.004 |
| $\sigma_{\rm BG_2}(ps)$ | 8.0 (fixed) | 8.0 (fixed) | 8.0 (fixed) |

Table 4.10: Correlation matrix from fit to $KK$ proper time distribution from CLEO II.V data.

| Par | Global | $\tau_{\rm Sig}$ | $\tau_{\rm BG}$ | $f_{\tau_{BG}}$ | $S_{\rm BG}$ | $f_{\rm BG_1}$ | $\sigma_{\rm BG_1}$ | $f_{\rm BG_2}$ |
|---|---|---|---|---|---|---|---|---|
| $\tau_{\rm Sig}$ | 0.30655 | 1.000 | -0.214 | -0.023 | 0.010 | -0.018 | -0.017 | 0.006 |
| $\tau_{\rm BG}$ | 0.71802 | -0.214 | 1.000 | -0.625 | -0.250 | 0.100 | 0.222 | -0.010 |
| $f_{\tau_{BG}}$ | 0.65438 | -0.023 | -0.625 | 1.000 | 0.259 | -0.032 | -0.099 | 0.015 |
| $S_{\rm BG}$ | 0.48299 | 0.010 | -0.250 | 0.259 | 1.000 | -0.175 | -0.024 | -0.008 |
| $f_{\rm BG_1}$ | 0.90744 | -0.018 | 0.100 | -0.032 | -0.175 | 1.000 | 0.881 | 0.366 |
| $\sigma_{\rm BG_1}$ | 0.91725 | -0.017 | 0.222 | -0.099 | -0.024 | 0.881 | 1.000 | 0.446 |
| $f_{\rm BG_2}$ | 0.47173 | 0.006 | -0.010 | 0.015 | -0.008 | 0.366 | 0.446 | 1.000 |

Table 4.11: Correlation matrix from fit to $\pi\pi$ proper time distribution from CLEO II.V data.

| Par | Global | $\tau_{\rm Sig}$ | $\tau_{\rm BG}$ | $f_{\tau_{BG}}$ | $S_{\rm BG}$ | $f_{\rm BG_1}$ | $\sigma_{\rm BG_1}$ | $f_{\rm BG_2}$ |
|---|---|---|---|---|---|---|---|---|
| $\tau_{\rm Sig}$ | 0.28551 | 1.000 | -0.167 | -0.059 | 0.029 | -0.011 | -0.034 | -0.009 |
| $\tau_{\rm BG}$ | 0.73360 | -0.167 | 1.000 | -0.633 | -0.313 | 0.018 | 0.233 | 0.228 |
| $f_{\tau_{BG}}$ | 0.67859 | -0.059 | -0.633 | 1.000 | 0.118 | -0.077 | -0.193 | -0.112 |
| $S_{\rm BG}$ | 0.73435 | 0.029 | -0.313 | 0.118 | 1.000 | 0.375 | -0.661 | 0.088 |
| $f_{\rm BG_1}$ | 0.40804 | -0.011 | 0.018 | -0.077 | 0.375 | 1.000 | -0.286 | 0.061 |
| $\sigma_{\rm BG_1}$ | 0.67900 | -0.034 | 0.233 | -0.193 | -0.661 | -0.286 | 1.000 | -0.009 |
| $f_{\rm BG_2}$ | 0.30220 | -0.009 | 0.228 | -0.112 | 0.088 | 0.061 | -0.009 | 1.000 |

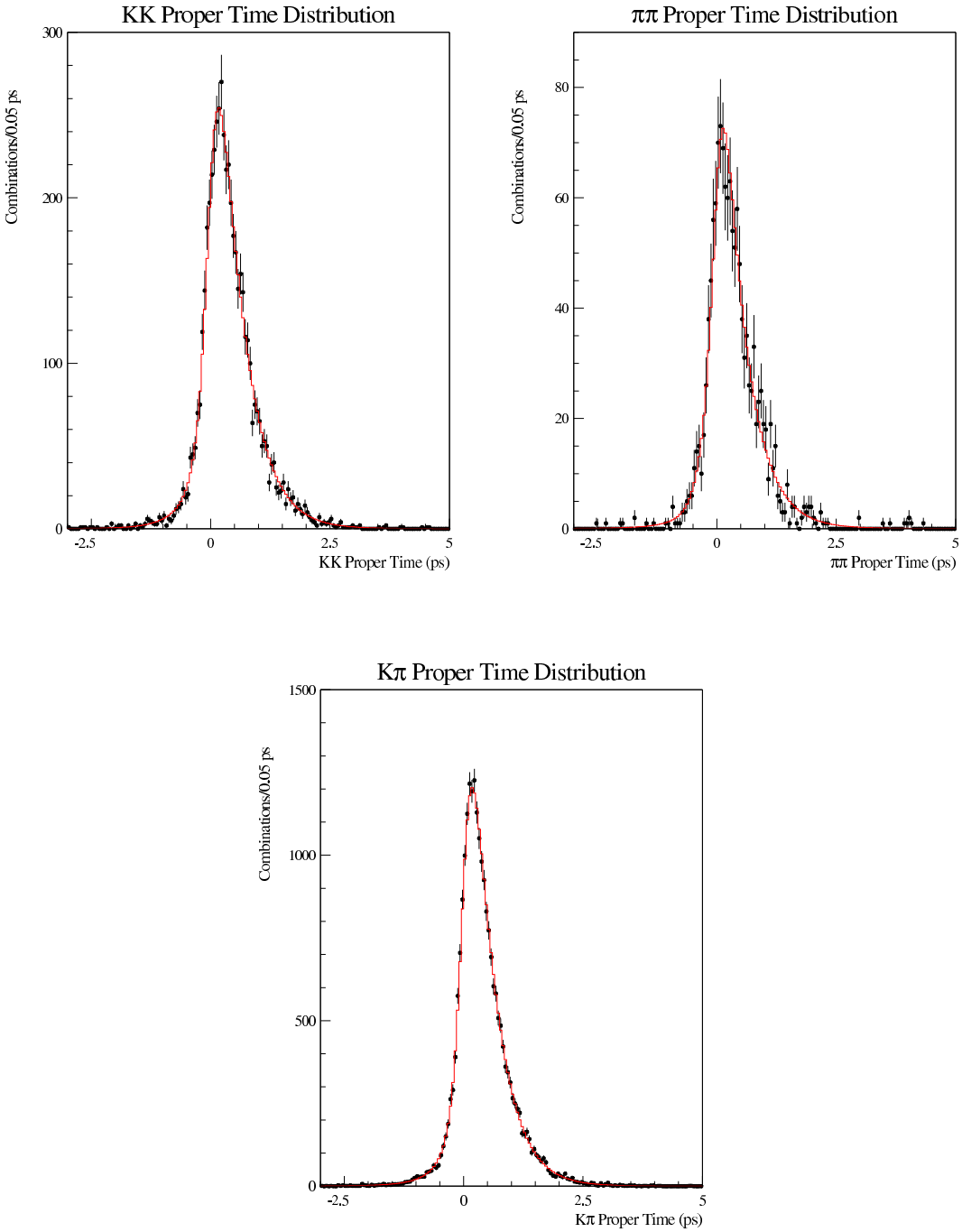


Figure 4.10: Proper time distributions from CLEO II.V data for $KK$, $\pi\pi$, and $K\pi$ with overlaid fit function.

Table 4.12: Correlation matrix from fit to $K\pi$ proper time distribution from CLEO II.V data.

| Par | Global | $\tau_{\rm Sig}$ | $S_{\rm Sig}$ | $f_{\rm Sig_1}$ | $\sigma_{\rm Sig_1}$ | $f_{\rm Sig_2}$ | $\tau_{\rm BG}$ | $f_{\tau_{BG}}$ | $S_{\rm BG}$ | $f_{\rm BG_1}$ | $\sigma_{\rm BG_1}$ | $f_{\rm BG_2}$ |
|---|---|---|---|---|---|---|---|---|---|---|---|---|
| $\tau_{\rm Sig}$ | 0.34426 | 1.000 | -0.125 | -0.002 | -0.139 | -0.018 | -0.173 | -0.010 | 0.035 | 0.084 | -0.076 | 0.017 |
| $S_{\rm Sig}$ | 0.52210 | -0.125 | 1.000 | -0.352 | 0.097 | -0.004 | -0.016 | 0.078 | -0.250 | 0.116 | -0.105 | 0.028 |
| $f_{\rm Sig_1}$ | 0.81246 | -0.002 | -0.352 | 1.000 | -0.719 | 0.026 | -0.057 | 0.067 | -0.061 | 0.050 | 0.088 | -0.039 |
| $\sigma_{\rm Sig_1}$ | 0.81606 | -0.139 | 0.097 | -0.719 | 1.000 | -0.065 | 0.183 | -0.110 | 0.147 | -0.363 | 0.111 | 0.021 |
| $f_{\rm Sig_2}$ | 0.44282 | -0.018 | -0.004 | 0.026 | -0.065 | 1.000 | 0.002 | 0.004 | -0.009 | 0.053 | -0.056 | -0.397 |
| $\tau_{\rm BG}$ | 0.73600 | -0.173 | -0.016 | -0.057 | 0.183 | 0.002 | 1.000 | -0.642 | -0.081 | -0.383 | 0.180 | -0.049 |
| $f_{\tau_{BG}}$ | 0.66198 | -0.010 | 0.078 | 0.067 | -0.110 | 0.004 | -0.642 | 1.000 | -0.011 | 0.229 | -0.091 | 0.026 |
| $S_{\rm BG}$ | 0.56281 | 0.035 | -0.250 | -0.061 | 0.147 | -0.009 | -0.081 | -0.011 | 1.000 | -0.421 | 0.275 | -0.059 |
| $f_{\rm BG_1}$ | 0.81901 | 0.084 | 0.116 | 0.050 | -0.363 | 0.053 | -0.383 | 0.229 | -0.421 | 1.000 | -0.661 | 0.073 |
| $\sigma_{\rm BG_1}$ | 0.73139 | -0.076 | -0.105 | 0.088 | 0.111 | -0.056 | 0.180 | -0.091 | 0.275 | -0.661 | 1.000 | -0.282 |
| $f_{\rm BG_2}$ | 0.52627 | 0.017 | 0.028 | -0.039 | 0.021 | -0.397 | -0.049 | 0.026 | -0.059 | 0.073 | -0.282 | 1.000 |

# CHAPTER 5
# CHECKS AND SYSTEMATIC UNCERTAINTIES

In this chapter, we describe the various consistency checks performed to make sure our result is robust, and provide estimates of systematic uncertainties involved with our analysis procedure.

## 5.1 Data Consistency Checks

In our normalized lifetime difference measurements between $KK$, $\pi\pi$, and $K\pi$, we expect that the measurements should be robust in the various ways we can divide our data samples. Put another way, the physics of this analysis does not change as a function of the kinematical variables of our $D$ candidates, or when the data was recorded, except due to statistical fluctuations. However, it is important to verify this by actually breaking the data samples up into pieces as a function of relavent variables and looking for statistically significant effects. If such behavior is observed, it may be indicative of detector miscalibrations or anomalous running conditions, among other things. Such effects, which even our detailed simulation might not know about, could conceivably bias our results. In the subsections which follow, we look for running in our $y$ measurements as a function of various kinematical variables of our $D$ candidates as well as run number. If no statistically significant running is observed in a given variable, we expect that the distribution of $y$ measurements will fit well to a flat line. Therefore, we monitor the confidence levels of fits of the $y$ measurements as a function of different variables. We observe no statistically significant running of our measurements as a function of any of the variables we checked.

### 5.1.1 Azimuthal Angle $\phi_D$

To see if we observe any dependence of $y$ on azimuthal angle in CLEO II.V data, we divide the sample into four bins of $\phi_D$, the reconstructed azimuthal angle of the $D$ candidate. The proper time distributions of these samples are fit independently with the unbinned likelihood fitter, and values of $y$ extracted. The results are shown in Figure 5.1. We do not observe a statistically significant $\phi$ dependence.

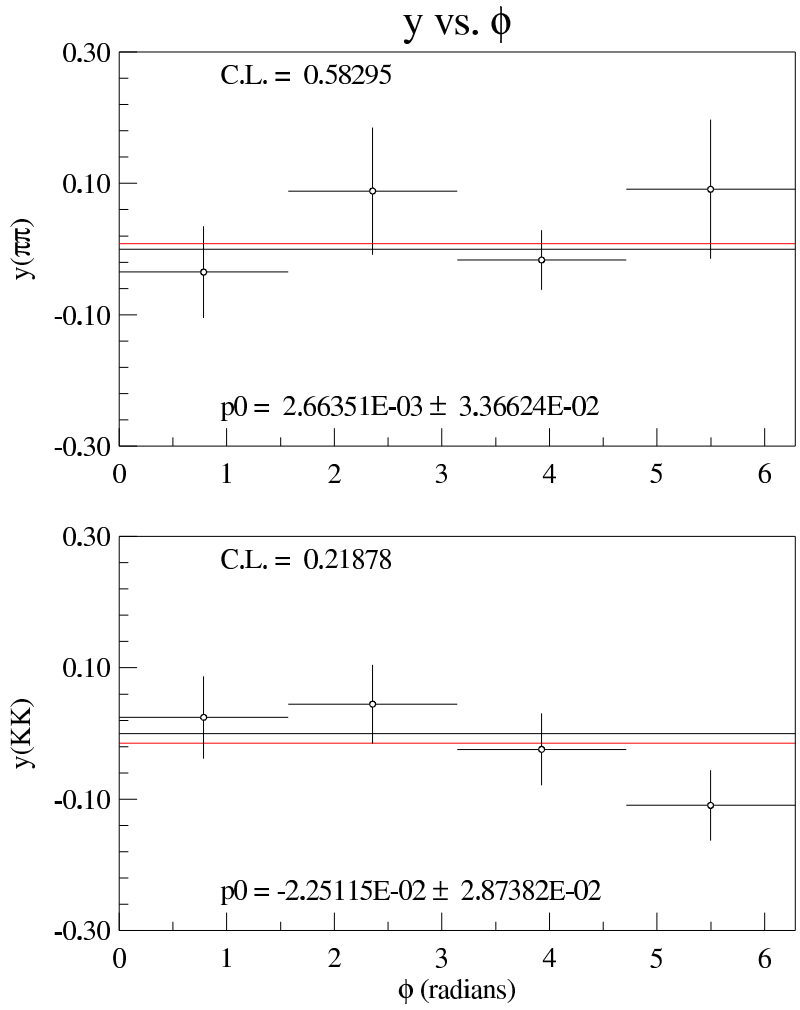


Figure 5.1: Mixing parameters $y_{\pi\pi}$ and $y_{KK}$ vs. $\phi_D$ in CLEO II.V data. The result of a fit to these points to a 0th order polynomial and its confidence level is shown. The line through the points in each plot is the uncorrected value for all data from Section 4.2.

### 5.1.2 Polar Angle $cos\theta_D$

To see if we observe any dependence of $y$ on polar angle in CLEO II.V data, we divide the sample into four bins of $cos\theta_D$, the cosine of the reconstructed polar angle of the $D$ candidate, and determine independent $y$ measurements from these samples. The results are shown in Figure 5.2. We do not observe a statistically significant $cos\theta$ dependence.

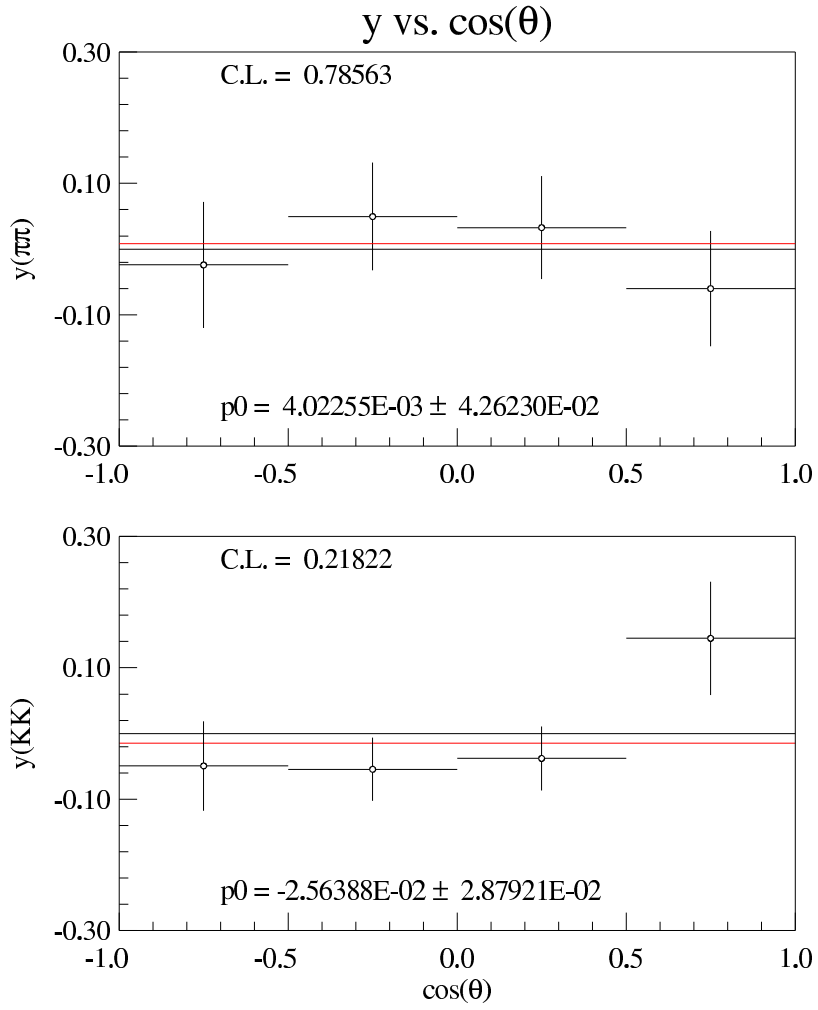


Figure 5.2: Mixing parameters $y_{\pi\pi}$ and $y_{KK}$ vs. $cos\theta_D$ in CLEO II.V data. The result of a fit to these points to a 0th order polynomial and its confidence level is shown. The line through the points in each plot is the uncorrected value for all data from Section 4.2.

### 5.1.3 Momentum

We check for momentum dependence by dividing the entire CLEOII.V data sample into 4 roughly equal pieces, and determine independent $y$ measurements from these samples. These measurements are shown in Figure 5.3. We do not observe a statistically significant dependence on momentum of the $D$ candidate.

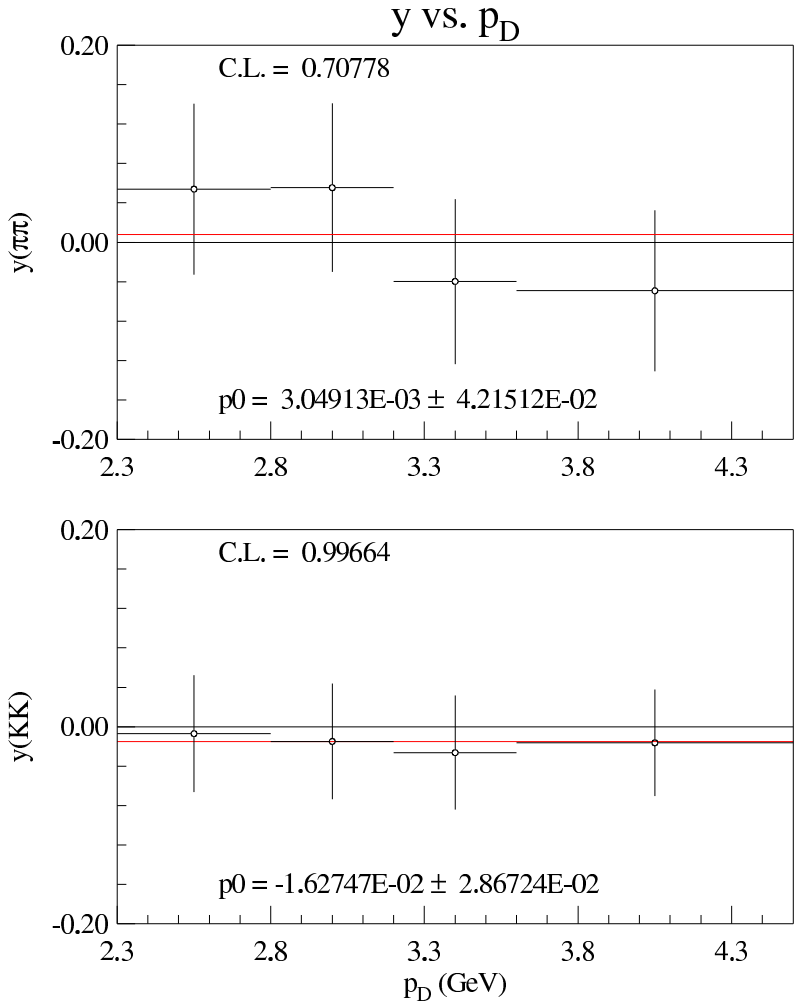


Figure 5.3: Mixing parameters $y_{\pi\pi}$ and $y_{KK}$ vs. $p_D$ in CLEO II.V data. The result of a fit to these points to a 0th order polynomial and its confidence level is shown. The line through the points in each plot is the uncorrected value for all data from Section 4.2.

### 5.1.4 Decay Angle $cos\theta^*$

We check for $cos\theta^*$ dependence by dividing the entire CLEOII.V data sample into 4 roughly equal pieces, and determine independent $y$ measurements from these samples. These measurements are shown in Figure 5.4. We do not observe a statistically significant dependence on $cos\theta^*$ of the $D$ candidate.

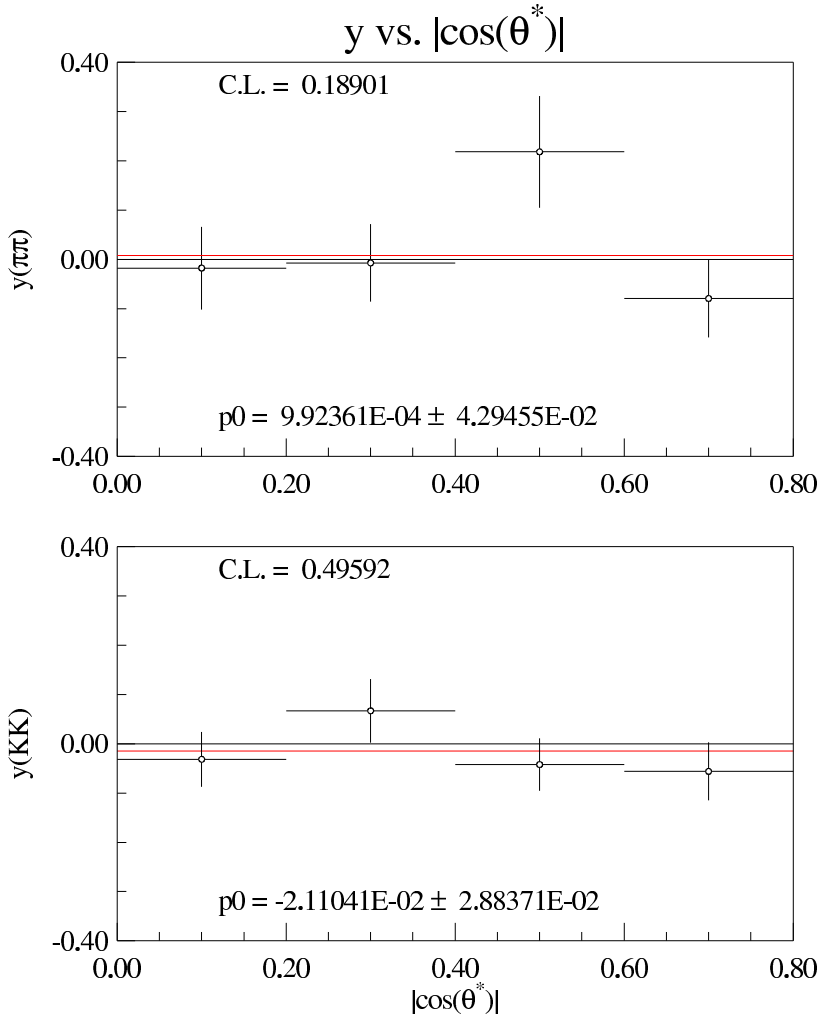


Figure 5.4: Mixing parameters $y_{\pi\pi}$ and $y_{KK}$ vs. $cos\theta^*$ in CLEO II.V data. The result of a fit to these points to a 0th order polynomial and its confidence level is shown. The line through the points in each plot is the uncorrected value for all data from Section 4.2.

### 5.1.5 Vertex Confidence Level prob($\chi^2_{vtx}$)

We check for prob($\chi^2_{vtx}$) dependence by dividing the entire CLEOII.V data sample into 4 pieces, and determine independent $y$ measurements from these samples. These measurements are shown in Figure 5.5. We do not observe a statistically significant dependence on prob($\chi^2_{vtx}$) of the $D$ candidate.

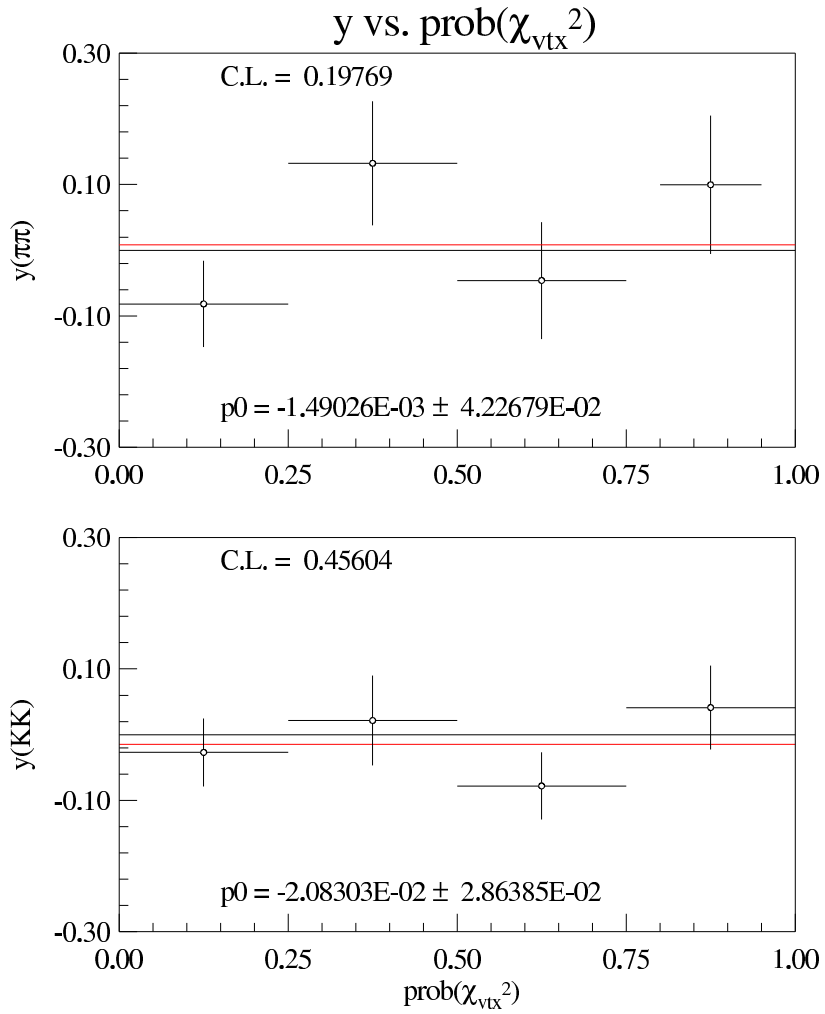


Figure 5.5: Mixing parameters $y_{\pi\pi}$ and $y_{KK}$ vs. prob($\chi^2_{vtx}$) in CLEO II.V data. The result of a fit to these points to a 0th order polynomial and its confidence level is shown. The line through the points in each plot is the uncorrected value for all data from Section 4.2.

### 5.1.6 Dataset

We check for dataset dependence by dividing the entire CLEOII.V data sample into 6 time-ordered, roughly equally sized pieces, and determine independent $y$ measurements from these samples. These measurements are shown in Figure 5.6. We do not observe a statistically significant dependence on dataset.

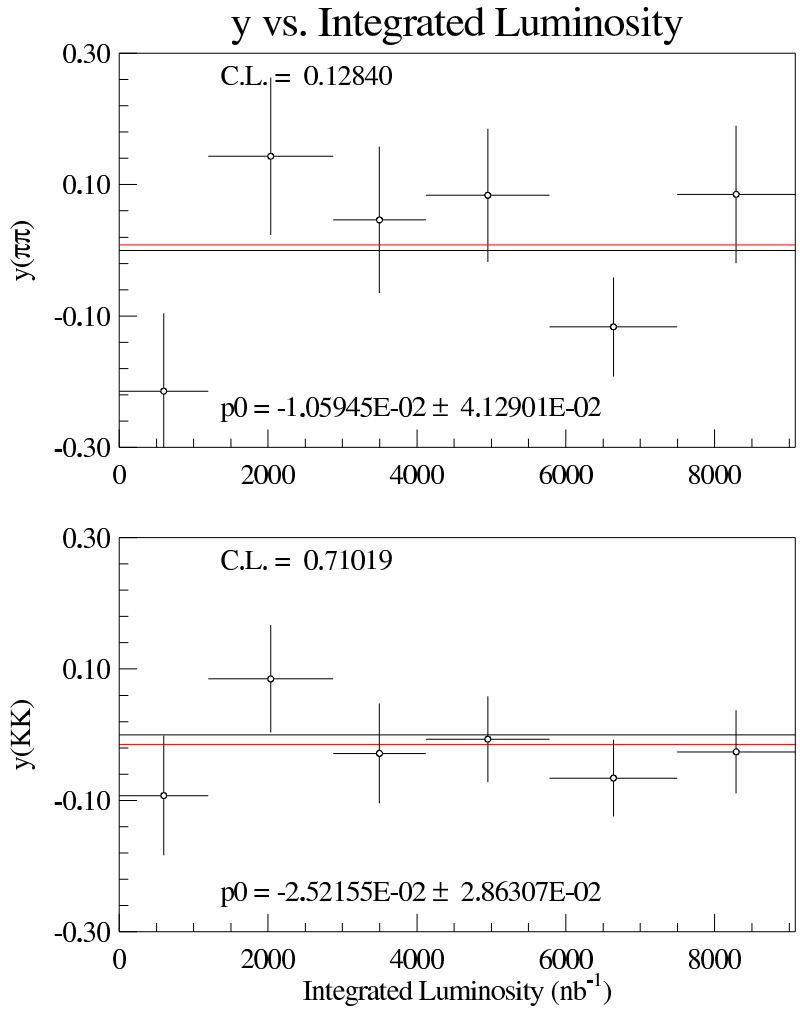


Figure 5.6: Mixing parameters $y_{\pi\pi}$ and $y_{KK}$ vs. integrated luminosity; boundaries between bins are on dataset boundaries. The result of a fit to these points to a 0th order polynomial and its confidence level is shown. The line through the points in each plot is the uncorrected value for all data from Section 4.2.

## 5.2 Systematic Uncertainties

Since we are measuring a normalized lifetime difference, the types of mistakes we can make are often consistent across decay channels and ultimately cancel. Of course, this is not true in general, and particularly using the assumptions we have made. Some of the assumptions we have made are that $KK$, $\pi\pi$, and $K\pi$ have identical proper time resolution functions, that our parameterization of the background is reasonable and robust, and that constraining the mass to 1.8646 GeV in the data is the right thing to do. We also examine some equally reasonable reasonable functional forms of our likelihood, which amount to different treatments of proper time outliers.

### 5.2.1 Signal Shape

It is reasonable to expect that the resolution functions for the signal in each of the decay modes are very similar due to the similar kinematics of the decays. For the background, this is not a reasonable assumption because there is no reason to expect the composition of the $K\pi$, $KK$, and $\pi\pi$ backgrounds to be the same (looking at truth table information in the simulation supports this conclusion). However, the kinematics of $K\pi$, $KK$, and $\pi\pi$ signals are not in fact identical, and constraining the shape of the $KK$ and $\pi\pi$ signal resolution functions to that of $K\pi$ is a source of systematic uncertainty. To evaluate this, we float the signal resolution parameters of $KK$ and $\pi\pi$ ($S_{\text{Sig}}$, $f_{\text{Sig}_1}$, $\sigma_{\text{Sig}_1}$, and $f_{\text{Sig}_2}$) in the unbinned lifetime fit. The results of this exercise form the data and monte carlo are shown in Table 5.1.

We take the difference from the high statistics monte carlo measurements as the systematic uncertainty due to our choice of signal resolution function:

$$\begin{aligned} \delta y_{KK} &= 0.007 \\ \delta y_{\pi\pi} &= 0.003 \\ \delta \overline{y} &= 0.005 \end{aligned} \tag{5.1}$$

Table 5.1: Unbinned fit results to proper time distributions, $y$ measurements and shifts in CLEO II.V monte carlo and data for $K\pi$, $KK$, and $\pi\pi$, where the resolution function for the signal in $KK$ and $\pi\pi$ were floated.

| Sample | $\tau_{KK}$(ps) | $\tau_{\pi\pi}$(ps) | $\tau_{K\pi}$(ps) |
|---|---|---|---|
| Monte Carlo | 0.4171±0.0041 | 0.4159±0.0060 | 0.4160±0.0015 |
| Data | 0.4113±0.0117 | 0.3975±0.0178 | 0.4046±0.0036 |
| | $y_{KK}$ | $y_{\pi\pi}$ | $\overline{y}$ |
| Monte Carlo | −0.003±0.010 | 0.000±0.015 | −0.002±0.009 |
| Data | −0.016±0.029 | 0.018±0.046 | −0.007±0.025 |
| | $\Delta y_{KK}$ | $\Delta y_{\pi\pi}$ | $\Delta\overline{y}$ |
| Monte Carlo | 0.007 | 0.003 | 0.005 |
| Data | 0.001 | −0.010 | −0.001 |

### 5.2.2 Background Shape

Expanding and our mass window selection criteria allows us to observe how changing the composition of the background impacts our result. Our treatment of the background, that it is represented by two components - one with lifetime and one without, is put to the test, as is our constraint that the two components have the same proper time resolution function. The results of varying the mass window size are summarized in Tables 5.2 and 5.4 for the data and monte carlo, respectively. Similarly, we can vary the overall level of the background by varying the $\Delta m$ requirement; Tables 5.3 and 5.5 show the effects of varying the background levels by ±50% in the data and monte carlo. We know our parameterization of the background leaves much to be desired, and expect a significant systematic error due to our modeling of the backgound shape.

We assign the systematic error from the monte carlo samples to avoid statistical fluctuations in the data; the differences between the monte carlo and data backgrounds are likely small compared to the systematic induced by our modelling. Varying the mass and $\Delta m$ windows are not the same systematic; they let in different kinds of backgrounds. So to assign the systematic error, we add the largest differences

Table 5.2: Unbinned fit results to proper time distributions, $y$ measurements, and shifts from CLEO II.V data for $KK$, $\pi\pi$, and $K\pi$ using different sized mass windows.

| Mass Window (MeV) | $\tau_{KK}$(ps) | $\tau_{\pi\pi}$(ps) | $\tau_{K\pi}$(ps) |
|---|---|---|---|
| $\pm 80$ | $0.4078 \pm 0.0112$ | $0.3984 \pm 0.0158$ | $0.4032 \pm 0.0034$ |
| $\pm 60$ | $0.4093 \pm 0.0113$ | $0.3991 \pm 0.0162$ | $0.4040 \pm 0.0035$ |
| $\pm 50$ | $0.4105 \pm 0.0114$ | $0.4027 \pm 0.0166$ | $0.4042 \pm 0.0035$ |
| $\pm 30$ | $0.4138 \pm 0.0119$ | $0.3982 \pm 0.0174$ | $0.4073 \pm 0.0042$ |
| | $y_{KK}$ | $y_{\pi\pi}$ | $\overline{y}$ |
| $\pm 80$ | $-0.011 \pm 0.028$ | $0.012 \pm 0.040$ | $-0.004 \pm 0.024$ |
| $\pm 60$ | $-0.013 \pm 0.029$ | $0.012 \pm 0.042$ | $-0.005 \pm 0.024$ |
| $\pm 50$ | $-0.015 \pm 0.029$ | $0.004 \pm 0.042$ | $-0.010 \pm 0.024$ |
| $\pm 30$ | $-0.016 \pm 0.030$ | $0.023 \pm 0.046$ | $-0.005 \pm 0.026$ |
| | $\Delta y_{KK}$ | $\Delta y_{\pi\pi}$ | $\Delta\overline{y}$ |
| $\pm 80$ | $-0.004$ | $-0.004$ | $-0.004$ |
| $\pm 60$ | $-0.002$ | $-0.004$ | $-0.003$ |
| $\pm 50$ | $0.000$ | $0.004$ | $0.002$ |
| $\pm 30$ | $0.001$ | $-0.015$ | $-0.003$ |

Table 5.3: Unbinned fit results to proper time distributions, $y$ measurements, and shifts from CLEO II.V data for $KK$, $\pi\pi$, and $K\pi$ using different sized $|\Delta m|$ windows.

| $\lvert\Delta m\rvert$ cut (MeV) | $\tau_{KK}$(ps) | $\tau_{\pi\pi}$(ps) | $\tau_{K\pi}$(ps) |
|---|---|---|---|
| $\pm 0.5$ | $0.4142 \pm 0.0116$ | $0.3899 \pm 0.0171$ | $0.4066 \pm 0.0037$ |
| $\pm 1.5$ | $0.4052 \pm 0.0120$ | $0.4059 \pm 0.0170$ | $0.4035 \pm 0.0035$ |
| | $y_{KK}$ | $y_{\pi\pi}$ | $\overline{y}$ |
| $\pm 0.5$ | $-0.018 \pm 0.029$ | $0.043 \pm 0.047$ | $-0.002 \pm 0.025$ |
| $\pm 1.5$ | $-0.004 \pm 0.031$ | $-0.006 \pm 0.043$ | $-0.005 \pm 0.026$ |
| | $\Delta y_{KK}$ | $\Delta y_{\pi\pi}$ | $\Delta\overline{y}$ |
| $\pm 0.5$ | $0.003$ | $-0.035$ | $-0.006$ |
| $\pm 1.5$ | $-0.011$ | $0.014$ | $-0.003$ |

from the monte carlo's nominal measurement in quadrature, from both the mass and $\Delta m$ variations:

$$\begin{aligned} \delta y_{KK} &= 0.008 \\ \delta y_{\pi\pi} &= 0.011 \\ \delta \overline{y} &= 0.008 \end{aligned} \tag{5.2}$$

Table 5.4: Unbinned fit results to proper time distributions, $y$ measurements, and shifts from CLEO II.V monte carlo for $KK$, $\pi\pi$, and $K\pi$ using different sized mass windows.

| Mass Window (MeV) | $\tau_{KK}$(ps) | $\tau_{\pi\pi}$(ps) | $\tau_{K\pi}$(ps) |
|---|---|---|---|
| $\pm 80$ | $0.4153 \pm 0.0039$ | $0.4120 \pm 0.0055$ | $0.4160 \pm 0.0014$ |
| $\pm 60$ | $0.4148 \pm 0.0039$ | $0.4142 \pm 0.0056$ | $0.4161 \pm 0.0014$ |
| $\pm 50$ | $0.4150 \pm 0.0040$ | $0.4149 \pm 0.0057$ | $0.4160 \pm 0.0014$ |
| $\pm 30$ | $0.4144 \pm 0.0042$ | $0.4160 \pm 0.0061$ | $0.4155 \pm 0.0015$ |
| | $y_{KK}$ | $y_{\pi\pi}$ | $\overline{y}$ |
| $\pm 80$ | $0.002 \pm 0.010$ | $0.010 \pm 0.014$ | $0.004 \pm 0.008$ |
| $\pm 60$ | $0.003 \pm 0.010$ | $0.005 \pm 0.014$ | $0.004 \pm 0.008$ |
| $\pm 50$ | $0.002 \pm 0.010$ | $0.003 \pm 0.014$ | $0.002 \pm 0.009$ |
| $\pm 30$ | $0.003 \pm 0.011$ | $-0.001 \pm 0.015$ | $0.001 \pm 0.009$ |
| | $\Delta y_{KK}$ | $\Delta y_{\pi\pi}$ | $\Delta\overline{y}$ |
| $\pm 80$ | 0.002 | $-0.007$ | $-0.001$ |
| $\pm 60$ | 0.001 | $-0.002$ | $-0.001$ |
| $\pm 50$ | 0.002 | 0.000 | 0.001 |
| $\pm 30$ | 0.001 | 0.004 | 0.002 |

Table 5.5: Unbinned fit results to proper time distributions, $y$ measurements, and shifts from CLEO II.V monte carlo for $KK$, $\pi\pi$, and $K\pi$ using different sized $|\Delta m|$ windows.

| $\Delta m$ cut (MeV) | $\tau_{KK}$(ps) | $\tau_{\pi\pi}$(ps) | $\tau_{K\pi}$(ps) |
|---|---|---|---|
| $\pm 0.5$ | $0.4125 \pm 0.0039$ | $0.4178 \pm 0.0059$ | $0.4155 \pm 0.0015$ |
| $\pm 1.5$ | $0.4111 \pm 0.0042$ | $0.4116 \pm 0.0057$ | $0.4159 \pm 0.0014$ |
| | $y_{KK}$ | $y_{\pi\pi}$ | $\overline{y}$ |
| $\pm 0.5$ | $0.007 \pm 0.010$ | $-0.006 \pm 0.014$ | $0.003 \pm 0.009$ |
| $\pm 1.5$ | $0.012 \pm 0.011$ | $0.010 \pm 0.014$ | $0.011 \pm 0.009$ |
| | $\Delta y_{KK}$ | $\Delta y_{\pi\pi}$ | $\Delta\overline{y}$ |
| $\pm 0.5$ | $-0.003$ | 0.009 | 0.000 |
| $\pm 1.5$ | $-0.008$ | $-0.007$ | $-0.008$ |

### 5.2.3 Treatment of Proper Time Outliers

While fixing the wider gaussians describing the poorest resolution signal and background to $8ps$ works well in the simulation, it is, after all, an arbitrary number. Here, we vary this assignment to see what effect our assumption has on the measurement of $y_{CP}$. We also dropped the "wide" gaussian altogether and replaced it with a cut on proper time. The results are displayed in Tables 5.6 and 5.7 for data and

Table 5.6: Fit results to proper time distributions from CLEO II.V data for $KK$, $\pi\pi$, and $K\pi$ using different treatments for proper time outliers.

| Outlier Treatment | $\tau_{KK}$(ps) | $\tau_{\pi\pi}$(ps) | $\tau_{K\pi}$(ps) |
|---|---|---|---|
| $\sigma_{\mathrm{Sig}_2} = \sigma_{\mathrm{BG}_2} = 4ps$ | 0.4109±0.0116 | 0.4012±0.0168 | 0.4044±0.0036 |
| $\sigma_{\mathrm{Sig}_2} = \sigma_{\mathrm{BG}_2} = 12ps$ | 0.4108±0.0116 | 0.4010±0.0168 | 0.4044±0.0036 |
| $\lvert t_i\rvert \leq 10ps$ | 0.4106±0.0115 | 0.4007±0.0168 | 0.4037±0.0036 |
| | $y_{KK}$ | $y_{\pi\pi}$ | $\overline{y}$ |
| $\sigma_{\mathrm{Sig}_2} = \sigma_{\mathrm{BG}_2} = 4ps$ | −0.016±0.029 | 0.008±0.043 | −0.009±0.025 |
| $\sigma_{\mathrm{Sig}_2} = \sigma_{\mathrm{BG}_2} = 12ps$ | −0.016±0.029 | 0.008±0.043 | −0.008±0.025 |
| $\lvert t_i\rvert \leq 10ps$ | −0.017±0.029 | 0.007±0.043 | −0.010±0.025 |
| | $\Delta y_{KK}$ | $\Delta y_{\pi\pi}$ | $\Delta\overline{y}$ |
| $\sigma_{\mathrm{Sig}_2} = \sigma_{\mathrm{BG}_2} = 4ps$ | 0.001 | 0.000 | 0.001 |
| $\sigma_{\mathrm{Sig}_2} = \sigma_{\mathrm{BG}_2} = 12ps$ | 0.001 | 0.000 | 0.000 |
| $\lvert t_i\rvert \leq 10ps$ | 0.002 | 0.001 | 0.002 |

Table 5.7: Fit results to proper time distributions from CLEO II.V monte carlo for $KK$, $\pi\pi$, and $K\pi$ using different treatments for proper time outliers.

| Outlier Treatment | $\tau_{KK}$(ps) | $\tau_{\pi\pi}$(ps) | $\tau_{K\pi}$(ps) |
|---|---|---|---|
| $\sigma_{\mathrm{Sig}_2} = \sigma_{\mathrm{BG}_2} = 4ps$ | 0.4142±0.0040 | 0.4146±0.0058 | 0.4158±0.0015 |
| $\sigma_{\mathrm{Sig}_2} = \sigma_{\mathrm{BG}_2} = 12ps$ | 0.4142±0.0040 | 0.4148±0.0058 | 0.4156±0.0015 |
| $\lvert t_i\rvert \leq 10ps$ | 0.4138±0.0040 | 0.4145±0.0058 | 0.4152±0.0015 |
| | $y_{KK}$ | $y_{\pi\pi}$ | $\overline{y}$ |
| $\sigma_{\mathrm{Sig}_2} = \sigma_{\mathrm{BG}_2} = 4ps$ | 0.004±0.010 | 0.003±0.014 | 0.004±0.009 |
| $\sigma_{\mathrm{Sig}_2} = \sigma_{\mathrm{BG}_2} = 12ps$ | 0.003±0.010 | 0.002±0.014 | 0.003±0.009 |
| $\lvert t_i\rvert \leq 10ps$ | 0.003±0.010 | 0.002±0.014 | 0.003±0.009 |
| | $\Delta y_{KK}$ | $\Delta y_{\pi\pi}$ | $\Delta\overline{y}$ |
| $\sigma_{\mathrm{Sig}_2} = \sigma_{\mathrm{BG}_2} = 4ps$ | 0.000 | 0.000 | −0.001 |
| $\sigma_{\mathrm{Sig}_2} = \sigma_{\mathrm{BG}_2} = 12ps$ | 0.001 | 0.001 | 0.000 |
| $\lvert t_i\rvert \leq 10ps$ | 0.001 | 0.001 | 0.000 |

monte carlo, respectively; we take the maximum deflection from nominal in the data as our estimate of systematic error:

$$\begin{aligned} \delta y_{KK} &= 0.002 \\ \delta y_{\pi\pi} &= 0.001 \\ \delta\overline{y} &= 0.002 \end{aligned} \tag{5.3}$$

Table 5.8: Fit results to proper time distributions from CLEO II.V data and monte carlo for $KK$, $\pi\pi$, and $K\pi$, where the proper time and proper time uncertainties were calculated without using a mass constraint.

| Sample | $\tau_{KK}$(ps) | $\tau_{\pi\pi}$(ps) | $\tau_{K\pi}$(ps) |
|---|---|---|---|
| Monte Carlo | 0.4116±0.0041 | 0.4153±0.0059 | 0.4156±0.0015 |
| Data | 0.4095±0.0117 | 0.4003±0.0169 | 0.4054±0.0036 |
| | $y_{KK}$ | $y_{\pi\pi}$ | $\overline{y}$ |
| Monte Carlo | 0.010±0.011 | 0.001±0.015 | 0.007±0.009 |
| Data | −0.010±0.030 | 0.013±0.044 | −0.003±0.025 |
| | $\Delta y_{KK}$ | $\Delta y_{\pi\pi}$ | $\Delta\overline{y}$ |
| Monte Carlo | −0.006 | 0.002 | −0.004 |
| Data | −0.005 | −0.005 | −0.005 |

### 5.2.4 Proper Time/Mass Correlation & Mass Scale

A mass constraint ($m_D = 1.8646$ GeV in MC, $m_D = 1.86514$ GeV in data) has been employed in all the fits performed in this document to account for the linear correlation between proper time and mass as well as any miscalibration of CLEO's mass scale (see Figure 4.5). In the monte carlo proper time fits, evaluating the signal likelihood using a proper time and uncertainty calculated with a mass constrained to the input mass is obviously a reasonable thing to do. However, in the data, we don't know what the actual mass of the $D^0$ meson is. The world's knowledge of the mass of the neutral $D$ meson is not very good; reference [29] has $m_D = 1.8645 \pm 0.0005$ GeV, which means we may have constrained to the wrong mass in the data. In an absolute lifetime determination, if one constrains to the "wrong" mass, each proper time measurement and the resulting lifetime will be biased. In a normalized lifetime difference determination like this one, bias can also result because the slope of the lifetime residual versus reconstructed mass is not the same in each decay channel (again, see Figure 4.5).

To estimate the systematic uncertainty due to problems with the CLEO mass scale as well as our choice of $m_D$ to constrain to in the data, we perform unbinned lifetime fits on the data without using the mass constraint. On average, this changes

Table 5.9: Fit results to $KK$, $\pi\pi$, and $K\pi$ proper time distributions in CLEO II.V data, where the proper time and proper time uncertainties were calculated without using a mass constraint.

| Signal Parameter | $KK$ | $\pi\pi$ | $K\pi$ |
|---|---|---|---|
| $\tau_{\rm Sig}$(ps) | 0.4095±0.0117 | 0.4003±0.0169 | 0.4054±0.0036 |
| $S_{\rm Sig}$ | 1.072 (fixed) | 1.072 (fixed) | 1.072±0.015 |
| $f_{\rm Sig_1}$ | 0.033 (fixed) | 0.033 (fixed) | 0.033±0.010 |
| $\sigma_{\rm Sig_1}$(ps) | 0.615 (fixed) | 0.615 (fixed) | 0.615±0.096 |
| $f_{\rm Sig_2}$ | 0.00041 (fixed) | 0.00041 (fixed) | 0.00041±0.00028 |
| $\sigma_{\rm Sig_2}$(ps) | 8.0 (fixed) | 8.0 (fixed) | 8.0 (fixed) |
| Background Parameter | $KK$ | $\pi\pi$ | $K\pi$ |
| $\tau_{\rm BG}$(ps) | 0.440±0.020 | 0.511±0.109 | 0.406±0.036 |
| $f_{\tau_{BG}}$ | 0.852±0.031 | 0.357±0.069 | 0.681±0.053 |
| $S_{\rm BG}$ | 1.070±0.049 | 1.326±0.102 | 1.428±0.093 |
| $f_{\rm BG_1}$ | 0.122±0.069 | 0.015±0.020 | 0.103±0.031 |
| $\sigma_{\rm BG_1}$(ps) | 0.47±0.15 | 3.10±1.58 | 1.36±0.19 |
| $f_{\rm BG_2}$ | 0.013±0.003 | 0.035±0.015 | 0.012±0.004 |
| $\sigma_{\rm BG_2}$(ps) | 8.0 (fixed) | 8.0 (fixed) | 8.0 (fixed) |

the mass contributing to the proper time measurement by amounts varying from $\approx$ 50 to 450 keV; which is on order of the potential mass scale problem implied by the detailed simulation (see Table 4.1). The results of these fits are given in Table 5.9 for the data and monte carlo, and the correlation coefficient matrices for the data fits are given in Tables 5.10, 5.11, and 5.12 for $KK$, $\pi\pi$, and $K\pi$, respectively. For the systematic due to mass scale problems, we assign the difference between the constrained and unconstrained measurements from the data:

$$\begin{aligned} \delta y_{KK} &= 0.005 \\ \delta y_{\pi\pi} &= 0.005 \\ \delta \overline{y} &= 0.005 \end{aligned} \tag{5.4}$$

### 5.2.5 Length Scale

Length scale problems, while paramount in an absolute lifetime determination, are less important a normalized lifetime difference; such mistakes tend to drop out.

Table 5.10: Correlation matrix from fit to $KK$ proper time distribution in CLEO II.V data, where the proper time and proper time uncertainties were calculated without using a mass constraint.

| Par | Global | $\tau_{\rm Sig}$ | $\tau_{\rm BG}$ | $f_{\tau_{BG}}$ | $S_{\rm BG}$ | $f_{\rm BG_1}$ | $\sigma_{\rm BG_1}$ | $f_{\rm BG_2}$ |
|---|---|---|---|---|---|---|---|---|
| $\tau_{\rm Sig}$ | 0.32120 | 1.000 | -0.219 | -0.031 | 0.000 | -0.008 | 0.000 | 0.016 |
| $\tau_{\rm BG}$ | 0.70823 | -0.219 | 1.000 | -0.636 | -0.248 | -0.048 | 0.036 | -0.121 |
| $f_{\tau_{BG}}$ | 0.66668 | -0.031 | -0.636 | 1.000 | 0.254 | 0.060 | 0.000 | 0.069 |
| $S_{\rm BG}$ | 0.58827 | 0.000 | -0.248 | 0.254 | 1.000 | 0.317 | 0.449 | 0.059 |
| $f_{\rm BG_1}$ | 0.90073 | -0.008 | -0.048 | 0.060 | 0.317 | 1.000 | 0.888 | 0.185 |
| $\sigma_{\rm BG_1}$ | 0.91732 | 0.000 | 0.036 | 0.000 | 0.449 | 0.888 | 1.000 | 0.216 |
| $f_{\rm BG_2}$ | 0.27296 | 0.016 | -0.121 | 0.069 | 0.059 | 0.185 | 0.216 | 1.000 |

Table 5.11: Correlation matrix from fit to $\pi\pi$ proper time distribution in CLEO II.V data, where the proper time and proper time uncertainties were calculated without using a mass constraint.

| Par | Global | $\tau_{\rm Sig}$ | $\tau_{\rm BG}$ | $f_{\tau_{BG}}$ | $S_{\rm BG}$ | $f_{\rm BG_1}$ | $\sigma_{\rm BG_1}$ | $f_{\rm BG_2}$ |
|---|---|---|---|---|---|---|---|---|
| $\tau_{\rm Sig}$ | 0.27358 | 1.000 | -0.152 | -0.094 | -0.009 | -0.011 | 0.003 | -0.001 |
| $\tau_{\rm BG}$ | 0.63193 | -0.152 | 1.000 | -0.532 | -0.090 | -0.217 | 0.001 | 0.020 |
| $f_{\tau_{BG}}$ | 0.57640 | -0.094 | -0.532 | 1.000 | -0.042 | 0.080 | 0.006 | -0.017 |
| $S_{\rm BG}$ | 0.34826 | -0.009 | -0.090 | -0.042 | 1.000 | -0.240 | 0.092 | 0.044 |
| $f_{\rm BG_1}$ | 0.67483 | -0.011 | -0.217 | 0.080 | -0.240 | 1.000 | 0.034 | -0.584 |
| $\sigma_{\rm BG_1}$ | 0.30548 | 0.003 | 0.001 | 0.006 | 0.092 | 0.034 | 1.000 | -0.259 |
| $f_{\rm BG_2}$ | 0.64893 | -0.001 | 0.020 | -0.017 | 0.044 | -0.584 | -0.259 | 1.000 |

Reference [25] found a systematic error due to length scale for the $K\pi$ lifetime measurement of 2.0 fs, or about 0.5% of a $D$ lifetime. From the data result, we then find the length scale systematic for $y_{KK}$ and $y_{\pi\pi}$ to be:

$$\begin{aligned} \Delta y_{KK} &= 0.0001 \\ \Delta y_{\pi\pi} &= 0.0003 \end{aligned} \tag{5.5}$$

which is completely negligible.

### 5.2.6 Total Systematic Uncertainty

The systematic uncertainties are tabulated in Table 5.13. The dominant systematic uncertainties are from our modelling of the background proper time resolution

Table 5.12: Correlation matrix from fit to $K\pi$ proper time distribution in CLEO II.V data, where the proper time and proper time uncertainties were calculated without using a mass constraint.

| Par | Global | $\tau_{\rm Sig}$ | $S_{\rm Sig}$ | $f_{\rm Sig_1}$ | $\sigma_{\rm Sig_1}$ | $f_{\rm Sig_2}$ | $\tau_{\rm BG}$ | $f_{\tau_{BG}}$ | $S_{\rm BG}$ | $f_{\rm BG_1}$ | $\sigma_{\rm BG_1}$ | $f_{\rm BG_2}$ |
|---|---|---|---|---|---|---|---|---|---|---|---|---|
| $\tau_{\rm Sig}$ | 0.36493 | 1.000 | -0.148 | -0.019 | -0.118 | -0.016 | -0.145 | -0.064 | 0.059 | 0.053 | -0.063 | 0.014 |
| $S_{\rm Sig}$ | 0.56327 | -0.148 | 1.000 | -0.303 | 0.090 | -0.009 | -0.069 | 0.153 | -0.305 | 0.197 | -0.140 | 0.045 |
| $f_{\rm Sig_1}$ | 0.84349 | -0.019 | -0.303 | 1.000 | -0.760 | 0.032 | -0.117 | 0.158 | -0.224 | 0.182 | 0.002 | -0.017 |
| $\sigma_{\rm Sig_1}$ | 0.84704 | -0.118 | 0.090 | -0.760 | 1.000 | -0.071 | 0.221 | -0.161 | 0.246 | -0.445 | 0.191 | -0.004 |
| $f_{\rm Sig_2}$ | 0.44109 | -0.016 | -0.009 | 0.032 | -0.071 | 1.000 | 0.006 | 0.002 | -0.011 | 0.057 | -0.076 | -0.386 |
| $\tau_{\rm BG}$ | 0.73928 | -0.145 | -0.069 | -0.117 | 0.221 | 0.006 | 1.000 | -0.650 | 0.060 | -0.379 | 0.153 | -0.058 |
| $f_{\tau_{BG}}$ | 0.69443 | -0.064 | 0.153 | 0.158 | -0.161 | 0.002 | -0.650 | 1.000 | -0.184 | 0.259 | -0.082 | 0.034 |
| $S_{\rm BG}$ | 0.68714 | 0.059 | -0.305 | -0.224 | 0.246 | -0.011 | 0.060 | -0.184 | 1.000 | -0.553 | 0.310 | -0.080 |
| $f_{\rm BG_1}$ | 0.85819 | 0.053 | 0.197 | 0.182 | -0.445 | 0.057 | -0.379 | 0.259 | -0.553 | 1.000 | -0.678 | 0.097 |
| $\sigma_{\rm BG_1}$ | 0.75201 | -0.063 | -0.140 | 0.002 | 0.191 | -0.076 | 0.153 | -0.082 | 0.310 | -0.678 | 1.000 | -0.283 |
| $f_{\rm BG_2}$ | 0.52247 | 0.014 | 0.045 | -0.017 | -0.004 | -0.386 | -0.058 | 0.034 | -0.080 | 0.097 | -0.283 | 1.000 |

Table 5.13: Tabulation of total systematic error for $y_{KK}$, $y_{\pi\pi}$, and the combined value, $\overline{y}_{CP}$.

| Systematic Error Source | $y_{KK}$ | $y_{\pi\pi}$ | $\overline{y}_{CP}$ |
|---|---|---|---|
| Signal Shape | 0.007 | 0.003 | 0.005 |
| Background Shape | 0.008 | 0.011 | 0.008 |
| Outlier Treatement | 0.002 | 0.001 | 0.002 |
| Mass Scale | 0.005 | 0.005 | 0.005 |
| Length Scale | 0.000 | 0.000 | 0.000 |
| Subtotal | 0.012 | 0.012 | 0.011 |
| Monte Carlo Statistics | 0.010 | 0.014 | 0.009 |
| Total | 0.016 | 0.018 | 0.014 |

and from monte carlo statistics. To calculate the total systematic uncertainty for this measurement, we sum in quadrature each of the systematic uncertainty components and find, including monte carlo statistics:

$$\begin{aligned} \delta y_{KK} &= 0.016 \\ \delta y_{\pi\pi} &= 0.018 \\ \delta \overline{y} &= 0.014 \end{aligned} \tag{5.6}$$

# CHAPTER 6
# CONCLUSION

Using 9.0 $fb^{-1}$ of CLEO II.V data, we have measured the $D$ mixing parameter $y$ in the $CP$ conserving limit by comparing the lifetimes of the decays $D^0 \to K\pi, KK, \pi\pi$. We find

$$y_{KK} = -0.019 \pm 0.029(stat.) \pm 0.016(syst.)$$
$$y_{\pi\pi} = 0.005 \pm 0.043(stat.) \pm 0.018(syst.)$$

and combined in a weighted average,

$$\overline{y}_{CP} = -0.011 \pm 0.025(stat.) \pm 0.014(syst.) \tag{6.1}$$

$y_{KK}$, $y_{\pi\pi}$, and the weighted average, $\overline{y}_{CP}$, are consistent with zero, and has similar sensitivity to [8]. We are unable to remove theoretical models that weren't already in conflict with [12].

Representing our result as a 95% confidence level interval:

$$-0.084 < y_{KK} < 0.046$$
$$-0.086 < y_{\pi\pi} < 0.096$$
$$-0.067 < \overline{y}_{CP} < 0.045$$

Figure 6.1 shows this result in the context of other charm mixing results from CLEO [12], FOCUS [11], and E791 [13]. The figure shows that the above measurement is not in

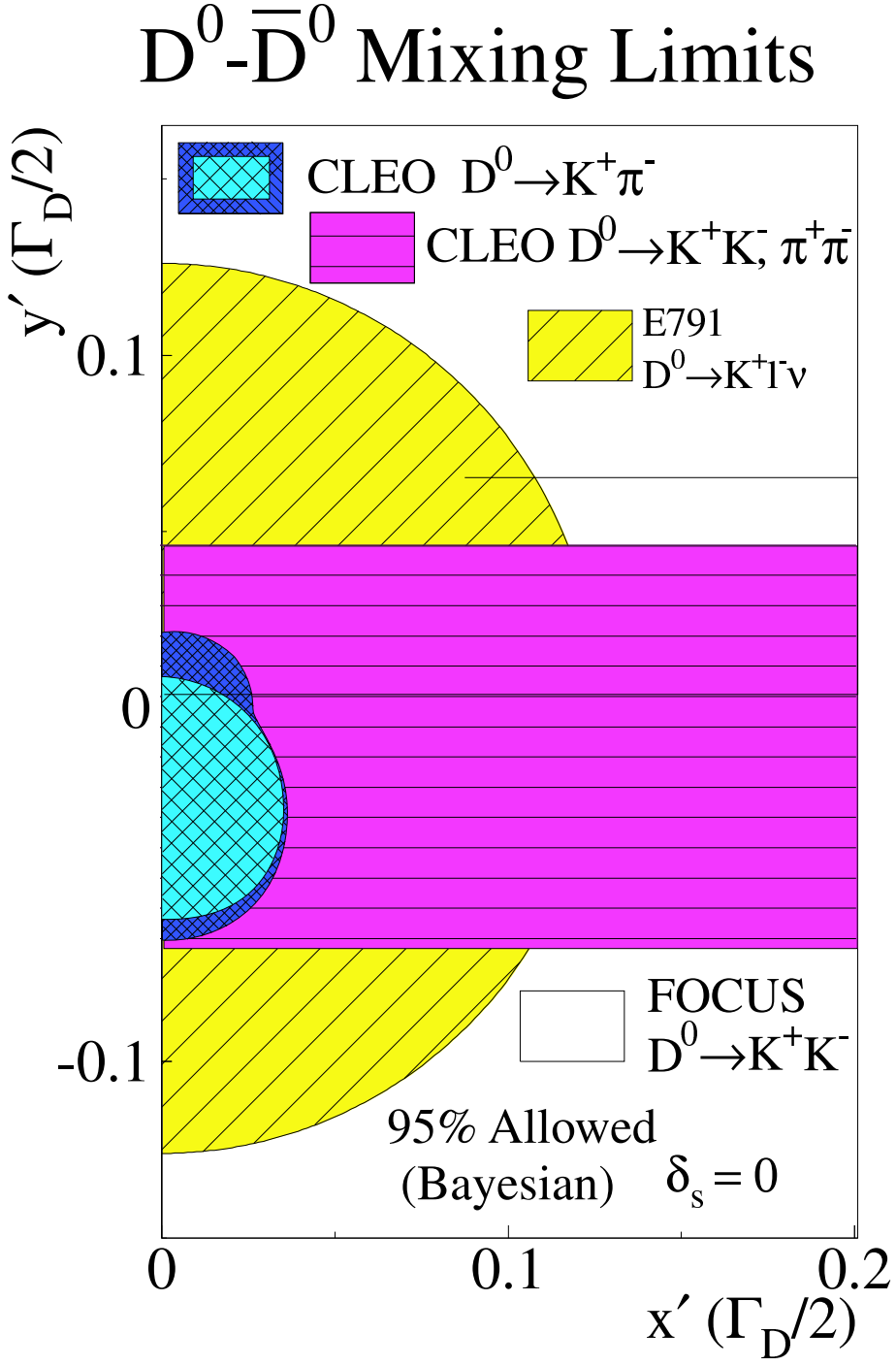


Figure 6.1: Summary of some recent mixing limits in the neutral $D$ system.

disagreement with the other results. Again, for purpose of illustration we have taken $\delta$ to be zero for Figure 6.1; this makes $x' = x$ and $y' = y$.

FOCUS has advantages over CLEO II.V in proper time resolution ($\sigma_t \equiv 0.08\tau_{D^0}$); it is so good they can use proper decay time significance ($t/\sigma_t$) as a selection criteria to assemble a large, fairly clean sample of candidates that did not have a $D^*$ tag (avoids branching fraction penalty). This makes the resolution of their $y_{CP}$ measurement better than that of CLEO II.V. Combining the FOCUS result with this one produces

$$0.010 < \overline{y}_{CP} < 0.038$$

at the 95% confidence level.

The FOCUS analysis, the E791 analysis, and this analysis can be combined into a single grand $CP$ eigenstate result:

$$0.008 < \overline{y}_{CP} < 0.034$$

at the 95% confidence level. Graphically, this result is shown with the FOCUS, E791, and Belle results in Figure 6.2.

If $D^0 - \overline{D^0}$ mixing is seen via some other means with a high rate, then our result indicates that mixing must come from $\Delta M$; i.e. mixing would take place through virtual intermediate states. Our result is consistent with the Standard model expectation that $y$ is very small. In addition, our result is consistent with many extensions to the Standard Model, which may significantly enhance $\Delta M$, but not $\Delta\Gamma$, such as supersymmetric models with quark-squark alignment, models with four generations, and models of light scalar leptoquarks [9].

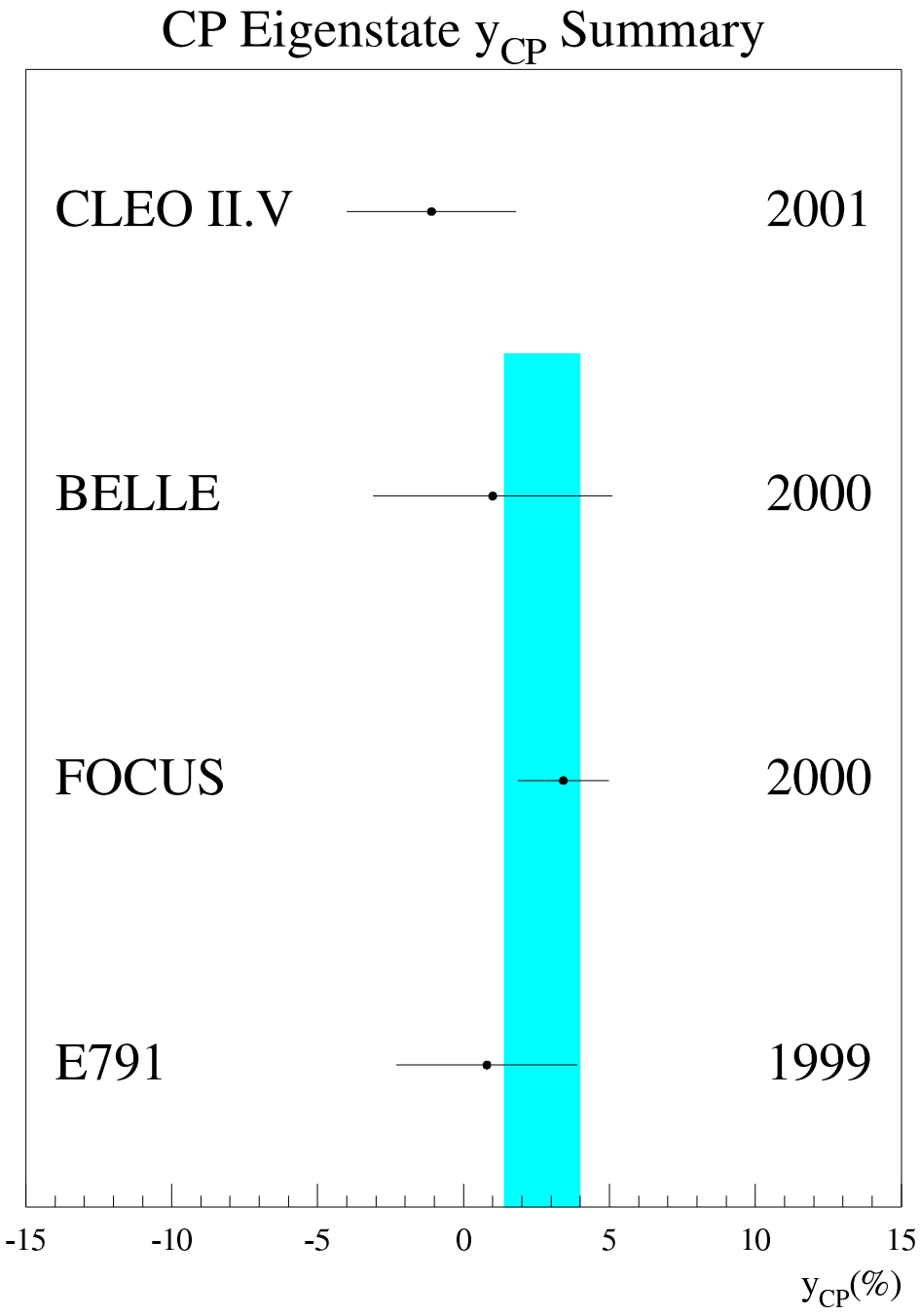


Figure 6.2: Summary of recent $y_{CP}$ limits in the neutral $D$ system, using CP eigenstate decays.

REFERENCES


[1] K. Lande *et al.*, Phys. Rev. **103**, 1901 (1956).

[2] P.F. Harrison and R. Quinn, The BaBar Physics Book, SLAC Report 504 (1998).

[3] W. Greiner and B. Müller, Gauge Theory of Weak Interactions, Springer-Verlag (1993).

[4] D. Griffiths, Introduction to Elementary Particles, John Wiley & Sons (1987).

[5] D.H. Perkins, Introduction to High Energy Physics, Addison-Wesley (1987).

[6] J.D. Richman, Heavy-Quark Physics and CP Violation, Lectures at the 1997 Nato Advanced Study Institute, Les Houches, France.

[7] H. Nelson, hep-ex/9908021 (1999).
http://xxx.lanl.gov/list/hep-ex/9908#hep-ex/9908021

[8] E.M. Aitala *et al.*, Phys. Rev. Lett. **83**, 32 (1999).

[9] G. Blaylock, A. Seiden, and Y. Nir, Phys. Lett. **355**, 555 (1995).

[10] H. Tajima, hep-ex/0102016 (2001).
http://xxx.lanl.gov/list/hep-ex/0102#hep-ex/0102016

[11] J.M. Link *et al.*, Phys. Lett. **B485**, 62 (2000).

[12] R. Godang *et al.*, Phys. Rev. Lett. **84**, 5038 (2000).

[13] E.M. Aitala *et al.*, Phys. Rev. Lett. **77**, 2384 (1996).

[14] Y. Kubota *et al.*, Nucl. Instrum. Methods A **320**, 66 (1992).

[15] D.G. Cassel *et al.*, Nucl. Instrum. Methods A **252**, 325 (1986).

[16] A. Bellerive, S.L. Jones, M. Garcia-Sciveres, CLEO CBX **94-39** (1994).

[17] P.M. Haas, A Measurement of Charmed Meson Lifetimes, Ph.D. Dissertation, The Ohio State University, 1988.

[18] CESR and CLEO Staff, CLNS **93/1265** (1993).
http://www.lns.cornell.edu/public/CLNS/CLEO.html.

[19] T.S. Hill, Nucl. Instrum. Methods A **418**, 32 (1998).

[20] K.K. Gan *et al.*, Nucl. Instrum. Methods A **374**, 27 (1996).

[21] W. Wagner, Multi-Hit Electronics for the CLEO Vertex Detector, Masters Thesis, The Ohio State University, 1996.

[22] GEANT – Detector Description and Simulation Tool, CERN Program Library Long Writeup W5013.

[23] P. Avery, CLEO CBX **95-55** (1995).
http://www.phys.ufl.edu/~avery/fitting.html, last modified June 20, 1996.

[24] C. Prescott, LifeFit Manual, http://www.phys.ufl.edu/~prescott/lifefit, last modified Oct. 10, 2000.

[25] Bonvicini *et al.*, Phys. Rev. Lett. **82**, 4586 (1999).

[26] http://www-pat.fnal.gov/mcfast/version_doc/v5_0/doc_index.html
contains documentation for the current version of MCFAST, last modified February 22, 1997.

[27] K. Sparks, CLEO CBX **89-282** (1989).
Current documentation available on the LNS WWW pages at
http://www.lns.cornell.edu/public/CLEO/soft/cleog/cleog.html.

[28] J. Alexander *et al.*, Phys. Rev. Lett. **77**, 5000 (1996).

[29] D.E. Groom *et al.*, The European Physical Journal **15** (2000) 1, available on the PDG WWW pages, http://pdg.lbl.gov/.

## BIOGRAPHICAL SKETCH

Craig Prescott was born in Fort Knox, Kentucky on September 17, 1969. He attended elementary and middle school in various locations in Wisconsin before moving to Florida at the age of thirteen. After attending Lake Brantley High School in Orlando for two years, he packed up his bags and moved to Clearwater, where he graduated from Countryside High School in 1987. He received his B.S. in physics from the University of Florida in 1991, and his B.A. in mathematics from the same institution in 1993. He liked Gainesville, Florida so much he decided to stay there for graduate school, where he pursued his interest in particle physics with Florida's CLEO collaborators.

I certify that I have read this study and that in my opinion it conforms to acceptable standards of scholarly presentation and is fully adequate, in scope and quality, as a dissertation for the degree of Doctor of Philosophy.

John M. Yelton, Chair
Professor of Physics

I certify that I have read this study and that in my opinion it conforms to acceptable standards of scholarly presentation and is fully adequate, in scope and quality, as a dissertation for the degree of Doctor of Philosophy.

Paul R. Avery
Professor of Physics

I certify that I have read this study and that in my opinion it conforms to acceptable standards of scholarly presentation and is fully adequate, in scope and quality, as a dissertation for the degree of Doctor of Philosophy.

Richard D. Field
Professor of Physics

I certify that I have read this study and that in my opinion it conforms to acceptable standards of scholarly presentation and is fully adequate, in scope and quality, as a dissertation for the degree of Doctor of Philosophy.

Pierre Ramond
Distinguished Professor of Physics

I certify that I have read this study and that in my opinion it conforms to acceptable standards of scholarly presentation and is fully adequate, in scope and quality, as a dissertation for the degree of Doctor of Philosophy.

Frederick Hamann III
Professor of Astronomy

This dissertation was submitted to the Graduate Faculty of the Department of Physics in the College of Liberal Arts and Sciences and to the Graduate School and was accepted as partial fulfillment of the requirements for the degree of Doctor of Philosophy.

May 2001

---

Dean, Graduate School